

Óbuda University



Ph.D. Dissertation

Development of Functionalized Calix[4]resorcinarene- Based Sensor Platforms for Heavy Metals Ions Detection in Aqueous Solutions.

By:

Larbi Eddaif

Under the supervision of **Dr. Abdul Shaban**

“This dissertation is presented as partial requirement
for the Doctor of Philosophy Degree award
at the Doctoral School of Materials Science and Technologies”

Experimental work was done at the Research Centre for Natural Sciences
Institute of Materials and Environmental Chemistry



© 2021
Larbi Eddaif
ALL RIGHTS RESERVED

Public Defense Committee

President: **Borsa Judit C. Sc. Prof. Emerita, ÓE**

Secretary: **Horváthné Drégelyi-Kiss Ágota Ph. D. egyetemi docens, ÓE**

Committee Members:

Gyulai Gergő Ph. D. tudományos munkatárs, ELTE

Halász Marianna C. Sc. egyetemi tanár, ÓE

Horváth Viola Ph. D. egyetemi docens, BME VBK

Opponents:

**Pekker Sándor D. Sc. tud. tanácsadó, ELKH Wigner FKK, kut.
professzor ÓE**

Takács Erzsébet D. Sc. emeritus kutatóprofesszor, ELKH EK

Public Defense date: 2022. 01. .

Heavy metal ions detection is a foremost concern in water sources. Conventional detection methods are at disadvantage being either time-consuming or expensive, therefore the necessity for rapid, economical, and precise detection devices is growing. Recently, the application of chemical sensors utilization as a detection and monitoring tool for heavy metal cations in water was developing.

For that purpose, potential sensing materials, Calix[4]resorcinarene macrocycles, were synthesized via acid-catalyzed cyclo-condensation. The prepared sensing elements are C-dec-9-enylcalix[4]resorcinarene labeled (I₁), C-undecylcalix[4]resorcinarene (I₂), C-dec-9-enylcalix[4]resorcinarene-O-(S)- α -methylbenzylamine (I₃), and C-dec-9-enylcalix[4]resorcinarene-O-(R)- α -methylbenzylamine (I₄), where I₃ and I₄ are novel enantiomers bearing chiral moieties.

Comprehensive structural characterization was performed using FTIR, NMR, and PXRD methods. The thermal properties and purity were examined by using TG-DSC-MS analyses. The encapsulation characteristics of the synthesized molecules (I₁-I₃), towards a set of cations (Cd²⁺, Cu²⁺, Hg²⁺, and Pb²⁺), were the subject of constructing Langmuir ultra-thin monolayers at the water/air interface level. Centered on the limiting areas obtained from the surface pressure area isotherms and the interfacial interactions supported by Gibbs-Shishkovsky's empirical equation calculations, high complexation abilities accompanied by ionic selectivity were revealed.

Innovative applications of oligomers (I₁-I₃) sensing platforms were investigated by the newly developed quartz crystal microbalance with impedance (QCM-I) measurements methodology. The response of QCM mass-sensitive sensors to a set of cations in the aqueous phase was studied showing decent statistical properties. Moreover, a high sensitivity towards Cu²⁺ ions in the case of I₃ was shown. Frequency-based selectivity studies were in good agreement with ionic selectivity gained from Langmuir analyses, and were expressed as follow: (I₁)-Cd²⁺, (I₁)-Hg²⁺, (I₂)-Cu²⁺, (I₂)-Pb²⁺, (I₃)-Cd²⁺, (I₃)-Hg²⁺.

Effective screen printed electrochemical detection platforms were constructed based on (I₁-I₃) oligomers. Characterization of the electrochemical platforms was performed by using cyclic voltammetry, square wave voltammetry, and electrochemical impedance spectroscopy. Under

optimized conditions of supporting electrolyte, pH, accumulation time, and potential, the voltammetric sensor platforms produced simultaneous and selective detection of Cd^{2+} , Hg^{2+} , Cu^{2+} , and Pb^{2+} despite the presence of major interferences present in water sources (Mg^{2+} , Ni^{2+} , Zn^{2+} , K^+ , and Al^{3+}). The method produced detection limits in the order of *ppb*, which is way below the thresholds of WHO and USEPA. The voltammetric sensors presented excellent reproducibility and repeatability with RSDs not passing 5 %.

In conformity with these outcomes, the synthesized oligomers showed their potential employment as sensing platforms for heavy metals cations detection in aqueous solutions.

D

claration

This Ph. D. dissertation is submitted to the Materials Science and Technologies,
Ph.D. School of Óbuda University as part of the requirements for the Doctor of
Philosophy degree award.

I, *Larbi Eddaif* declare that the research carried out herein is my work, that the
references chapter has a clear listing of the sources employed in writing this
document, and that this dissertation is original and has never been previously
submitted neither in part nor in full for any other degree.



Signature

November 24rd 2021
Date

Acknowledgments

At the outset, my sincere appreciations go to my advisor **Dr. Shaban Abdul** for his supervision in the course of my Ph.D. studies, his infinite assistance in all aspects comprising social life and science. My scientific achievements are owing to his helpfulness, competence, motivation, and dedication to hard work. Still, the words cannot describe my sincere acknowledgments towards him, but in simple words ‘Thank you for the paramount friendship, gags, and discussions that will last forever, thanks for being my life-mentor in Hungary.

My truthful thanks go to Prof. **Borsa Judit** for her support throughout the Ph. D. period, and **Prof. Telegdi Judit**, for the social and scientific assistance. My thanks to **Hersics Katalin**, and all the Óbuda University staff.

Special acknowledgments to **Prof. Pokol György** , **Prof. Buday László**, and **Dr. Tompos András**, and **Dr. Keresztes Zsófia** for welcoming me to the Research Centre for Natural Sciences.

My greetings to all my colleagues at the (*IMEC, RCNS*), particularly **Dr. Abohalkuma Talah**, **Dr. Felhósi Ilona**, **Pávai Mária**, **Dr. Románszki Loránd**, **Dr. Szábo Tamás**, **Kránicz Andrea**, and **Jámbor Andrea**.

I am thankful to **Trif László** for the thermal investigations, **Dr. Egyed Orsolya** for the NMR analysis, **Dr. Németh Csaba** for the XRD analysis, and **Dr. Mihaly Judit** for the FTIR measurements.

Special thanks to **Dr. Szendrő István** and **MicroVacuum Ltd.** for their generous opportunity to apply the QCM-I system in the thesis.

The Tempus Public Foundation is highly thanked for funding my Ph.D. studies under the framework of the Stipendium Hungaricum Scholarship Program.

I am grateful to all my family members, friends, professors, as well as to each person that helped in conducting this research work from far or near.

*Last but not least my thanks and appreciation to all my family members,
without their support, this would not have been possible.*

This work is dedicated to my
parents.

C

ontents

Declaration.....	i
Acknowledgments	ii
Dedication.....	iii
List of Figures.....	viii
List of Tables	xi
List of Acronyms	xii
Chapter 1: Introduction.....	1
Chapter 2: State of the art	4
2.1 Heavy metals	4
2.1.1 Overview	4
2.1.2 Description and toxicity.....	4
2.1.3 Detection of HMs	5
2.2 Sensors.....	6
2.2.1 Introduction	6
2.2.2 Description and characteristics	6
2.2.3 Sensors' classification	7
2.2.3.1 <i>Optical sensors</i>	9
2.2.3.2 <i>Electrochemical sensors</i>	9
2.2.3.3 <i>Piezoelectric sensors</i>	11
2.2.3.3.1 <i>Surface Acoustic Wave (SAW) sensors</i>	11
2.2.3.3.2 <i>Guided Wave (GW) sensors</i>	11
2.2.3.3.3 <i>Bulk Acoustic Wave (BAW) Sensors</i>	11
2.3 Applications of sensing materials.....	12
2.3.1 Nanostructures	13
2.3.2 Biological platforms	13
2.3.3 Polymers	14
2.3.4 Macrocyclic compounds.....	14
2.3.4.1 <i>Crown ethers</i>	14
2.3.4.2 <i>Cyclodextrins</i>	15
2.3.4.3 <i>Calixarenes/ Resorcinarenes</i>	16

2.3.4.3.1 <i>Introduction</i>	16
2.3.4.3.2 <i>Applications in complexation and extraction</i>	18
2.3.4.3.3 <i>Applications in heavy metals' detection and sensing</i>	20
2.4 The Hungarian scientific contribution to Ion Selective Electrodes (ISEs).....	24
Chapter 3: Methodology and experimental	25
3.1 Chemicals	25
3.2 Synthesis of ionophores.....	26
3.3 Ionophores analytical characterization techniques	28
3.3.1 Attenuated Total Reflectance-Fourier Transform InfraRed spectroscopy	28
3.3.2 Nuclear Magnetic Resonance spectroscopy	29
3.3.3 Thermogravimetry-Differential Scanning Calorimetry-Mass Spectrometry	29
3.3.4 X-Ray Powder Diffraction and Polarimetry	29
3.3.5 Polarimetry	30
3.4 Interfacial interactions based on the Langmuir films: Surface pressure-Area (Π -A) isotherms.....	30
3.5 Heavy metals detection processes: Quartz Crystal Microbalance with impedance measurements (QCM-I) and electrochemical tests.....	31
3.5.1. Electrode pretreatments	31
3.5.2. Ionophores immobilization on the gold sensing area	32
3.5.3 Quartz Crystal Microbalance with Impedance (QCM-I) experiments	32
3.5.4 Electrochemical detection experiments	34
3.5.4.1 <i>Screen-printed electrode (SPE) characterization</i>	35
3.5.4.2 <i>Experimental parameters optimization</i>	36
3.5.4.2.1 <i>Effect of supporting electrolyte</i>	36
3.5.4.2.2 <i>Effect of pH</i>	36
3.5.4.2.3 <i>Effect of accumulation time and accumulation potential</i>	37
3.5.4.3 <i>Calibration studies</i>	37
3.5.4.4 <i>Interference studies</i>	37
3.5.4.5 <i>Reproducibility and repeatability</i>	37
Chapter 4: Experimental results	38
4.1 Introduction	38
4.2 Ionophores' characterization results	38
4.2.1 Attenuated Total Reflectance-Fourier Transform InfraRed spectroscopy	38
4.2.2 Nuclear Magnetic Resonance spectroscopy	39

4.2.3 Thermogravimetry-Differential Scanning Calorimetry-Mass Spectrometry	39
4.2.4 X-Ray Powder Diffraction results	43
4.3 Heavy metals subphases/Ionophores interfacial interactions	44
4.3.1 Introduction	44
4.3.2 Surface pressure-area (Π -A) isotherms' results.....	44
4.3.2.1 <i>Phase transition descriptions</i>	44
4.3.2.1.1 <i>Langmuir isotherms' results for ionophore I₁</i>	44
4.3.2.1.2 <i>Langmuir isotherms' results for ionophore I₂</i>	45
4.3.2.1.3 <i>Langmuir isotherms' results for ionophore I₃</i>	47
4.4 Results of Quartz Crystal Microbalance with Impedance measurements (QCM-I)...	48
4.4.1 Introduction	48
4.4.2 Effect of heavy metals ions on the gold surface of quartz crystals	48
4.4.3 Heavy metals' concentration effect on resorcinarenes-piezogravimetric sensors ...	49
4.5 Electrochemical characterization.....	52
4.5.1 Cyclic voltammetry (CV) and Square wave voltammetry (SWV).....	52
4.5.2 Electrochemical impedance spectroscopy (EIS)	55
4.6 Optimization of the physicochemical parameters	56
4.6.1 Effect of supporting electrolyte	56
4.6.2 Effect of pH	57
4.6.3 Effect of accumulation time	58
4.6.4 Effect of accumulation potential effect	59
Chapter 5: Discussions	60
5.1 Introduction	60
5.2 Langmuir isotherms	60
5.2.1 Limiting area variations and their effect on ionic selectivity	61
5.2.2 Heavy metals adsorption within oligomeric ultra-thin films.....	63
5.3 Quartz Crystal Microbalance with Impedance measurement (QCM-I)	65
5.3.1 Sensing characteristics.....	67
5.3.2 Ionophores' attachment on the gold surface.....	69
5.3.3 Ionophores' affinity toward heavy metals	69
5.4 Electrochemical determination of heavy metals.....	74
5.4.1 Interferences study.....	76
5.4.2 Examination of reproducibility and repeatability	77
5.5 Heavy metals ions detection mechanisms	77
5.5.1 Piezogravimetric detection mechanism	77

5.5.2 Electrochemical detection mechanism	78
Chapter 6: Conclusions and future recommendations	79
New scientific results.....	81
List of contributions.....	83
References	85
Appendices	95

List of Figures

Fig. 2.1: Working principle and different components of a sensor.....	6
Fig. 2.2: Sensor signal calibration curve.....	7
Fig. 2.3: Classification of chemical sensors based on transduction mode.....	8
Fig. 2.4: Structure of a QCM resonator.....	12
Fig. 2.5: Common crown ethers structures.....	15
Fig. 2.6: Molecular structures of calix[4]resorcinarene and calix[4]arene.....	17
Fig. 2.7: Top and side views of p-tert-butylcalix[4]arene's cone conformation.....	18
Fig. 2.8: Cone-conformation of p-tert-butylcalix[4]arene emphasizing its different parts (Annulus, upper and lower rims)	18
Fig. 2.9: Different conformations of a typical calix[4]arene.....	19
Fig. 2.10: Structures of employed ionophores in the 1 st Calix-based ISE reported by the McKervey group.....	20
Fig. 2.11: The front page of the Hungarian patent of Pungor Ernő on heterogeneous ion-selective membranes.....	24
Fig. 3.1: Common synthetic route of calix[4]resorcinarene derivatives.....	26
Fig. 3.2: Synthetic approach for ionophores I ₁ and I ₂	27
Fig. 3.3: Synthetic procedure for compounds I ₃ and I ₄	28
Fig. 3.4: Langmuir-Blodgett trough (Model 611 NIMA Technology Ltd).....	31
Fig. 3.5: QCM-I 008 unit setup (<i>Courtesy of MicroVacuum Ltd</i>).....	33
Fig. 3.6: Fluidic QCM-I setup and data assessment process.....	34
Fig. 3.7: Gamry Interface 1010E potentiostat and the employed electrochemical cell	35
Fig. 3.8: Solartron 1250 frequency analyzer and Solartron 1286 electrochemical interface.....	35
Fig. 3.9: Electrochemical detection setup and data assessment process	36
Fig. 4.1: IR profiles of the ionophores.....	39

Fig. 4.2: Proton (^1H) and Carbon (^{13}C) NMR spectra of ionophore I_1	40
Fig. 4.3: TGA and DSC graphs for ionophores I_1 - I_4	41
Fig. 4.4: Characteristic MS of evolved volatiles from ionophores I_1 - I_4	42
Fig. 4.5: Diffractograms of the ionophores I_1 - I_4	43
Fig. 4.6: Langmuir (Π -A) isotherms for ionophore I_1	45
Fig. 4.7: Surface Pressure-Area isotherms for ionophore I_2	46
Fig. 4.8: Langmuir isotherms for ionophore I_3	47
Fig. 4.9: Normalized frequency, dissipation, and FWHM shifts of unmodified crystal resonators against various ions amounts.....	49
Fig. 4.10: Normalized frequency, dissipation, and FWHM shifts for ionophore I_1 based QCM sensor against various ions amounts	50
Fig. 4.11: Normalized frequency, dissipation, and FWHM shifts for ionophore I_2 based QCM sensor against various ions amounts	51
Fig. 4.12: Normalized frequency, dissipation, and FWHM shifts for ionophore I_3 based QCM sensor against various ions amounts	52
Fig. 4.13: Overlaid voltammograms of a) bare electrodes in 0.2 M HCl, b) bare electrodes in the presence of 1 ppm each of heavy metals in 0.2 M HCl, c) modified electrodes in 0.2 M HCl, d) modified electrodes in the presence of 1 ppm each of heavy metals in 0.2 M HCl.....	53
Fig. 4.14: SWV signatures of a) bare electrodes in 0.2 M HCl, b) bare electrodes in the presence of 1 ppm each of heavy metals in 0.2 M HCl, c) modified electrodes in 0.2 M HCl, d) modified electrodes in the presence of 1 ppm each of heavy metals in 0.2 M HCl.. ..	54
Fig. 4.15: EIS Nyquist plots of a) bare electrodes in 0.2 M HCl, b) bare electrodes in the presence of 1 ppm each of heavy metals in 0.2 M HCl, c) modified electrodes in 0.2 M HCl, d) modified electrodes in the presence of 1 ppm each of heavy metals in 0.2 M HCl.. ..	55
Fig. 4.16: Influence of various supporting electrolytes on the electrochemical signals of the modified electrodes in presence of 1 ppm each of heavy metals.....	56
Fig. 4.17: Influence of different pH values on the SWV signals of the modified electrodes in presence of 1 ppm each of heavy metals in HCl 0.2 M ($\text{pH}_i = 0.7$).....	57
Fig. 4.18: Influence of accumulation time on the SWV signals of the modified electrodes in presence of 1 ppm each of heavy metals in HCl 0.2 M ($\text{pH} = 0.7$).	58
Fig. 4.19: Influence of accumulation potential on the SWV signals of the modified electrodes in presence of 1 ppm each of heavy metals in HCl 0.2 M ($\text{pH} = 0.7$)	59

Fig. 5.1: Langmuir isotherm schematic highlighting various monolayers' phases.....	60
Fig. 5.2: Limiting area (A_{lim}) dependence on heavy metals concentration for I ₁ -I ₃	62
Fig. 5.3: Prospective arrangements of ionophores I ₁ -I ₃ on the water-air interface	63
Fig. 5.4: Potential interfacial complexation mechanism between ionophores I ₁ -I ₃ and the heavy metals ($M^{n+} = Cd^{2+}, Cu^{2+}, Hg^{2+}$ and Pb^{2+}).....	64
Fig. 5.5: Γ_{max}^{HM} definition plots for I ₁ -I ₃ in the function of heavy metals' amounts	65
Fig. 5.6: Frequency variation upon continuous loading of the sensor's surface over time.....	66
Fig. 5.7: Dissipation energy factor variations in time	66
Fig. 5.8: Dynamic ranges for ionophores I ₁ -I ₃ based on the normalized frequency and full width at half maximum variations	68
Fig. 5.9: Full width at half maximum variations of the Calix-QCM chemosensors (I ₁ , I ₂ , I ₃) for different concentrations (5, 25, 50, 500, and 1000 ppm) of Cd^{2+}	70
Fig. 5.10: Full width at half maximum variations of the Calix-QCM chemosensors (I ₁ , I ₂ , I ₃) for different concentrations (5, 25, 50, 500, and 1000 ppm) of Cu^{2+}	71
Fig. 5.11: Full width at half maximum variations of the Calix-QCM chemosensors (I ₁ , I ₂ , I ₃) for different concentrations (5, 25, 50, 500, and 1000 ppm) of Hg^{2+}	72
Fig. 5.12: Full width at half maximum variations of the Calix-QCM chemosensors (I ₁ , I ₂ , I ₃) for different concentrations (5, 25, 50, 500, and 1000 ppm) of Pb^{2+}	73
Fig. 5.13: Simultaneous electrochemical determination of the studied heavy metals in the concentration range from 1 to 100 ppb under optimal conditions based on I ₁ -I ₃ modified SPEs, the inserts are presented for the corresponding calibration curves.....	75
Fig. 5.14: Bar charts representing the heavy metals peak currents for the I ₁ -I ₃ @SPEs sensors in the absence (control) and existence of interfering ions under optimal conditions.....	76

L

ist of Tables

Table 2.1: Main characteristics of conventional HMs monitoring methods.....	5
Table 2.2: Metrological parameters of a sensor.....	8
Table 2.3: List of Calix based compounds as extracting, coordinating, and complexing agents.....	19
Table 2.4: Calix-based chemosensors for metal ions detection.....	21
Table 3.1: List of used chemicals in the thesis work.....	25
Table 5.1: $\Gamma_{\max}^{\text{HM}}$ values for ionophores I ₁ -I ₃	65
Table 5.2: Metrological parameters of resorcinarene-based QCM sensors.....	67
Table 5.3: Metrological parameters of the developed sensors.....	75
Table 5.4: Current peak deviations for 100 ppb of HMs in the presence of 40 folds' excess of interfering ions.	77
Table 5.5: RSDs related to reproducibility and repeatability of the developed sensors.....	77

L

ist of acronyms

- **¹H/¹³C NMR**: Proton /Carbon Nuclear Magnetic Resonance spectroscopy;
- **AFM**: Atomic Force Microscopy;
- **ASLSV**: Anodic Stripping Linear Sweep Voltammetry;
- **AuE**: Gold Electrode
- **AuNPs**: Gold Nanoparticles;
- **BAW**: Bulk Acoustic Wave;
- **CD**: Cyclodextrin;
- **CMEs**: Chemically Modified Electrodes;
- **CPE**: Carbon Paste Electrode;
- **DNA**: Deoxyribonucleic acid
- **DPASV**: Differential Pulse Anodic Stripping Voltammetry;
- **DPSV**: Differential Pulse Stripping Voltammetry;
- **DPV**: Differential Pulse Voltammetry;
- **EDTA**: Ethylene Diamine Tetra-acetic Acid;
- **EGA**: Evolved Gas Analysis;
- **EIS**: Electrochemical Impedance Spectroscopy;
- **ERGO**: Electrochemically Reduced Graphene Oxide;
- **FTIR**: Fourier-Transform Infrared spectroscopy;
- **GCE**: Glassy Carbon electrode;
- **GW**: Guided Wave;
- **HMs**: Heavy Metals;
- **IIPs**: Ion-Imprinted Polymers;
- **ISE**: Ion Selective Electrode;
- **ITO**: Indium Tin Oxide;
- **LOD**: Limit of Detection;
- **LOQ**: Limit of Quantification;
- **LOL**: Limit of Linearity;
- **LR**: Linear Range;
- **MWCNTs**: Multi-Walled Carbon Nanotubes;
- **PANI**: Polyaniline;
- **PXRD**: Powder X-Ray Diffraction;
- **QCM-I**: Quartz Crystal Microbalance with Impedance measurements;
- **RGO**: Reduced Graphene Oxide;
- **SAW**: Surface Acoustic Wave;
- **SEM**: Scanning Electron Microscopy;
- **SPE**: Screen Printed Electrode;
- **SSE**: Stainless Steel Electrode;
- **SWASV**: Square Wave Anodic Stripping Voltammetry;
- **SWNTs**: Single-Walled Nanotubes;
- **SWV**: Square Wave Voltammetry;
- **TG-DSC-MS**: Coupled Thermogravimetry-Differential Scanning Calorimetry-Mass Spectrometry.

C

hapter 1: Introduction

➤ *Statement of the problem*

The metals ions pollution poses a global risk, as trace levels of these toxicants if present in the ecosystem and are above the recommended thresholds, are causing lethal effects to human health. Mostly, they come into the body via direct consumption of contaminated water and food beverages. Therefore, early environmental detection is crucial. The recognition of metals ions in real samples is a difficult task, the main restrictions come from the complexity of their matrices and very low concentrations, often below the detection limits of available techniques. On large scale, myriads of analytical procedures and physicochemical tools have been used to gather information on heavy metals (HMs) determination and monitoring in water sources, these approaches provide very fine and complete information in terms of sensitivity and selectivity, besides significant constraints in connection to complication and duration of analysis (sampling, preparation, calibration, etc.).

At present, the sensors' reputation is well acknowledged, owing to their capability of conducting recognition investigations that were once dominated by analytical chemistry techniques, more advantages are offered by sensors viz. instrumentation low-cost, portability, data acquisition speed, technical reliability, real-time label-free onsite employment, and an overtime mapping-out of the target elements' existence in the studied environment, this later benefit is prohibitively costly when it comes to traditional detection procedures.

The design, construction, integration, and real application of HMs monitoring chemosensors, are comprehensively studied and reported in the literature, upon employing sensing platforms ranging from inorganic and nanomaterials to organic and macrocyclic elements, by way of illustration calixarenes and resorcinarenes, which had known ever-accelerating progress with regards to synthesis, structural alterations, and cone dimensions' modifications.

However, the mainstream of Calix-based chemosensing platforms targeting HMs recognition in water matrices is of either electrochemical concept or optical principle and no systematic study was carried out applying bulk acoustic wave (BAW) techniques as quartz crystal microbalance (QCM) to develop Calix-sensors for such applications.

➤ ***Aims and objectives of the research***

The aims of this research are:

- ✓ To perform the synthesis of resorcinarene molecules,
- ✓ To characterize the synthesized resorcinarene molecules, using several analytical methods (Fourier Transform Infra-Red spectroscopy (FTIR), X-Ray Diffraction (XRD), Nuclear Magnetic Resonance spectroscopy (NMR), and thermal analyses (TG-DSC-MS)),
- ✓ To investigate the complexing abilities of the resorcinarenes' ultra-thin layers utilizing the surface-pressure area isotherms based on the Langmuir technique,
- ✓ To investigate the potential applications of the synthesized molecules as recognition elements in detecting HMs, through applying the novel quartz crystal microbalance with impedance capability measurements device (QCM-I) and other electrochemical methods, namely cyclic voltammetry (CV), electrochemical impedance spectroscopy (EIS), and square wave voltammetry (SWV).

➤ ***Structure of the dissertation***

Accordingly, the outline of the dissertation body structure contains the following chapters:

Chapter 2 (State of the art): Offers a literature overview of metal ions, their toxicity, and their traditional detection via conventional physicochemical techniques and analytical procedures. It also gives insights on sensors' history, description, and classification, as well as further applications of sensing materials utilized in electroanalysis, focusing on reviewing the calixarenes and resorcinarenes' history, synthesis, structural alterations, complexing, and sensing applications.

Chapter 3 (Methodology and experimental): Highlights the applied apparatuses for the ionophores chemical characterization, the interfacial interaction via Langmuir isotherms, and the HMs detection application through QCM-I and electrochemical methods. It also lists the utilized chemicals, explains the resorcinarenes synthetic routes, and how the complexation and detection measurements were done emphasizing the different employed procedures.

Chapter 4 (Experimental results): States the gained outcomes from the synthesized resorcinarenes' structural characterization manifesting in the functional groups acquired from the FTIR analyses, the aliphatic and aromatic chemical shifts from the NMR investigations, the crystallinity degree from the XRD, the thermal stability, and the purity from the thermal analyses, besides investigating the ionophores' encapsulation properties employing the

Langmuir technique, and their metals ions detection results via utilizing QCM-I and electrochemistry.

Chapter 5 (Discussions): Deliberates the limiting area variations and ionic selectivity acquired from the interfacial interactions between the studied metals ions and the resorcinarenes at the water/air interface, discusses the sensing characteristics gained from the sensing outcomes of QCM-I and electrochemistry besides explaining the detection mechanisms.

Chapter 6 (Conclusions): Summarizes the main findings and the resulting conclusions, and highlights recommendations for future work to facilitate the environmental detection of HMs.

C

Chapter 2: State of the art

2.1 Heavy metals

2.1.1 Overview

Metallic species (Rare, earth, and heavy metals (HMs)) exist naturally in the earth's crust with varying concentrations. HMs are environmentally omnipresent, naturally found in ionic forms, compounds, or complexes that are harmless to human beings at trace levels often immobilized inside isolated compartments. HMs, are chemicals having a density greater than 4.5 g/cm^3 according to the Aarhus Protocol (Denmark, June 1998) of the Geneva Convention [1]. The most poisonous ones to humans are lead (Pb), mercury (Hg), arsenic (As), and cadmium (Cd). Others as copper (Cu), zinc (Zn), and chromium (Cr), yet necessary to human wellbeing in minor amounts, but are toxic at higher doses [2,3]. The welfare vital metals and metalloids context is comprehensive to cover Na, Mg, K, Ca, V, Mn, Fe, Co, and Ni [4]. The human disturbances of natural biogeochemical activities result in metallic pollution [5]. Indeed, HMs being extracted, purified, processed for industrial use, and consequently released towards the ecosystem), the overall process results in indirect exposure of plants, animals, and human beings to HMs.

2.1.2 Description and toxicity

The HMs' chemical nature can be modified by redox reactions, but their elemental nature remains the same and precludes any possibility of thermal decomposition or microbiological degradation. Consequently, they gather in soils and sediments, developing very complex chemistry due to abiotic (pH, redox potential) and biotic factors (microbial activity) [6,7]. Their toxicity is exerted by the substitution of essential metals in the human body, by blocking functional groups, or by interaction with enzymes and nucleic acids (via binding to DNAs' thiol groups, altering their functional properties) [5]. The HMs accumulation in living organisms generates toxic effects; e.g. renal necrosis and lung cancer for *cadmium*, as it accumulates through the respiratory route in the lungs and kidneys (10-35 years as biological half-life), however, it's still not considered genotoxic or carcinogen if entered the body via oral route [1]. *Lead* exposure gives rise to cardiovascular illness, neurodevelopmental effects, high systolic blood pressure, impaired renal function, mental retardation, and even mortality [1]. Irritability and blindness are diseases arising from *mercury*, esp. its inorganic compounds as

mercury(II) chloride, which targets the kidney through inhalation, resulting in colitis and hemorrhagic gastritis, and so it is considered weakly genotoxic [1]. Other diseases as gastrointestinal infections (nausea, vomiting, and diarrhea), are occurring from *copper* toxicity [1]. Aiming at limiting humans' exposure to HMs, it is necessary to develop less polluting industries, besides identifying the polluted sites, via the early detection and monitoring of HMs.

2.1.3 Detection of HMs

The HMs detection is based on common physicochemical methods and conventional analytical techniques; including Atomic Absorption Spectroscopy (AAS), X-Ray Fluorescence (XRF), Instrumental Neutron Activation Analysis (INAA), Inductively Coupled Plasma (ICP), High-Performance Liquid Chromatography (HPLC), and Gas chromatography (GC); **Table 2.1** presents a principle features' summary of those routine detection methods, lightening their high sensing characteristics, this latter fact is translated by their huge practical applications; as an example, *Caroli* and his research group determined the concentrations of As, Cd, Cr, Cu, Fe, Mn, Ni, Pb, Pt, Sn, V, and Zn, in honey by using ICP-AES and ICP-MS [8].

Table 2.1: Main characteristics of conventional HMs monitoring methods.

Techniques	Spectroscopy			X-ray	Neutron	Chromatography	
	Optical		Mass	Fluorescence (XRF)	Activation (INAA)	Liquid	Gas
	ICP-OES	AAS	ICP-MS			HPLC	GC
Sample nature	Liquid/ Gas	Liquid/ Gas	Liquid/ Gas	Solid/ Liquid	Solid/ Liquid	Liquid	Gas
Selectivity	Multi- elemental	Mono- elemental	Multi- elemental	Multi- elemental	Multi- elemental	Multi- elemental	
LOD	1-100 ppb	100 ppt – 10 ppb	1 ppt – 1 ppb	ppm	1 ppt – 1 ppb	—	—

Kenawy and coworkers used chemically modified chloro-methylated polystyrene ion-exchanger by applying AAS for the HMs determination in natural and biological samples [9]. *Silva et al.*, studied the simultaneous preconcentration and determination of some metals in water samples using 4-(2-pyridylazo)-resorcinol via ICP-OES [10], the obtained detection limits for Cu, Zn, Cd, and Ni were 18.9×10^{-9} , 16.83×10^{-9} , 15.3×10^{-9} , and 0.11×10^{-6} mol.L⁻¹, respectively. *Elouzi et al.* investigated the possibility of using bio-surfactants to remove or reduce the concentrations of HMs via ICP-OES [11]. Other research groups utilized AAS [12,13], ICP-MS [14], and Atomic Fluorescence Spectrometry (AFS) to monitor HMs [15].

The high degree of specificity, selectivity, and sensitivity, are major advantages of conventional HMs detection techniques. Nevertheless, they tend to be time-consuming, costly, require sample preparation procedures, and need professionally trained scientists. Subsequently, the development of a consistent, cost-effective, label-free, and reliable system for the real-time onsite detection and quantification of HMs, would be a valuable contribution to environmental analysis; the research is, therefore, focusing on the development of miniaturized devices ‘*Lab on a chip technology: Sensors*’ capable of being low-priced and having rapid responses, high sensitivities and selectivity towards HMs.

2.2 Sensors

2.2.1 Introduction

In the early 1950s, *Clark* began to develop the first sensor pointing at measuring the dissolved oxygen concentration in blood. His collaboration with *Lyon* in 1962, led to the invention of a biosensor combining an enzymatic membrane containing glucose oxidase, and an oxygen electrode for glucose determination in blood [16]. Half a decade later, *Updike* and *Hickson* developed an enzymatic electrode to measure glucose in biological solutions [17]. In 1969, *Guilbault* created a device capable of measuring urea amounts in blood and urine [18,19]. Since these first discoveries, sensors and biosensors have been attracting the researchers’ attention and were increasingly used in all fields including the pharmaceutical, petrochemical, and biomedical industries.

2.2.2 Description and characteristics

By definition, a sensor is an electronic device capable of transforming a physical, chemical, or biological quantity into an electrical one (signal), e.g. a frequency, a voltage, or a current (**Fig. 2.1**) [20].

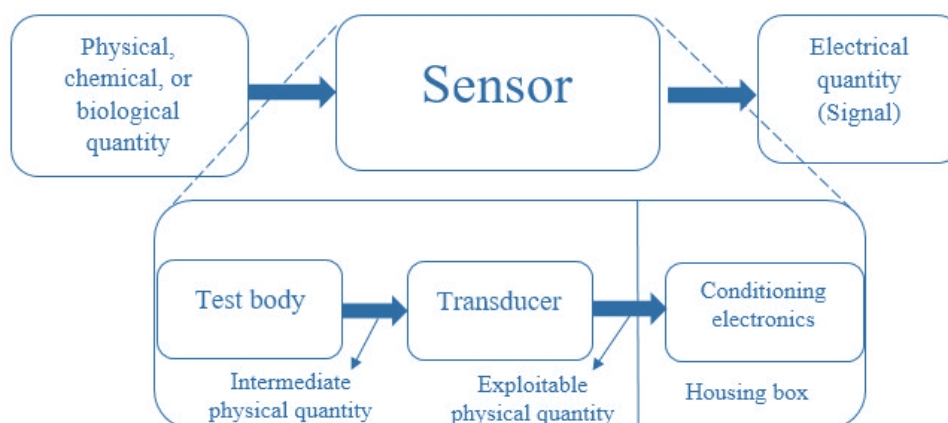


Fig. 2.1: Working principle and different components of a sensor.

Sensors are composed of many parts, namely: *The test body*; a sensitive element that transforms the measured magnitude to a measurable physical quantity. *The transducer* translates the physical quantity into an electrical one (output signal). *The housing box* is a mechanical element for protecting, holding, and fixing the sensor. And *the packaging/conditioning electronics* are a device that converts the sensor's output signal into a standard measurement signal, *the packaging/conditioning electronics* are the link between the sensor and the control system since they amplify and process the electrical signal. Commonly, sensors are characterized by metrological parameters which are experimentally evaluated based on various factors as shown in **Table 2.2**.

By adjusting the calibration curve (**Fig. 2.2**) of a sensor, it is possible to determine and understand the relationship between the input and the output quantities, in terms of metrological parameters and detection features (Sensitivity, detection limit, dynamic and linear ranges...etc.).

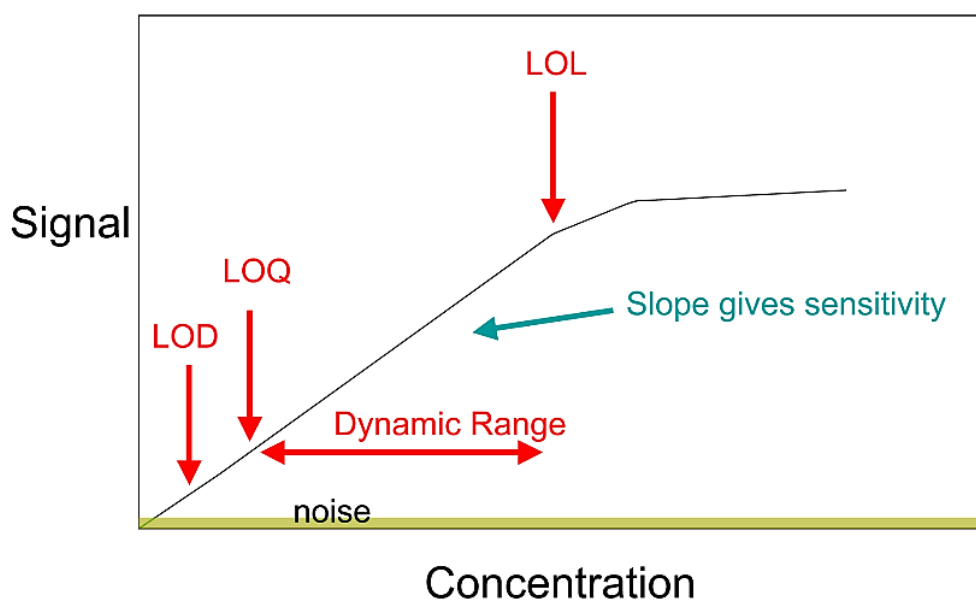


Fig. 2.2: Sensor signal calibration curve.

2.2.3 Sensors' classification

Sensors can be classified according to the used sensing platform/modifier layer; biological platforms e.g. DNA, proteins, and lipids for *Biosensors*, chemical substances as macrocycles and polymers for *Chemical Sensors*...etc. Otherwise according to the involved transduction principle in the recognition application: optical transduction for *optical sensors*, electrochemical transduction for *electrochemical sensors*, or else piezoelectric transduction for *piezoelectric/gravimetric sensors*; **Fig. 2.3** is demonstrating a simple classification of chemosensors based on the utilized transduction mode.

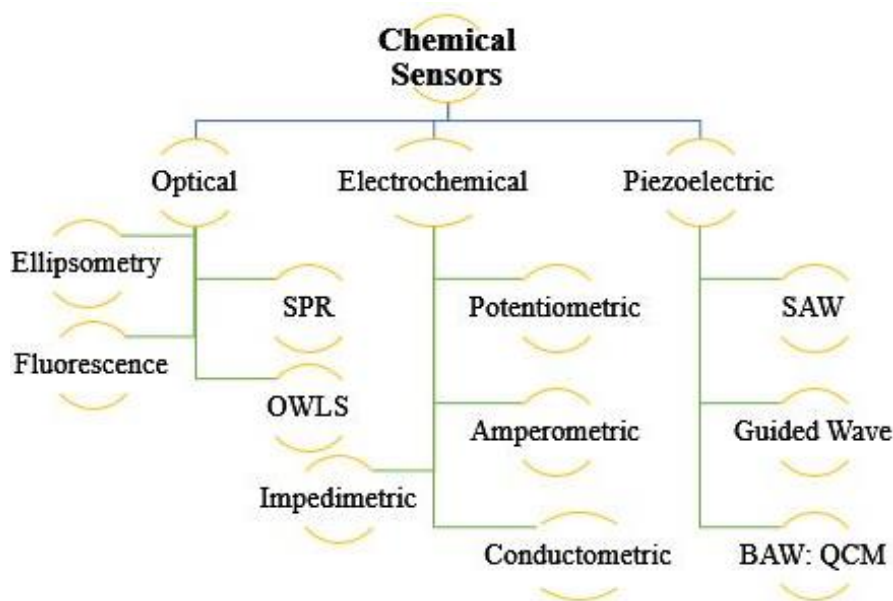


Fig. 2.3: Classification of chemical sensors based on transduction mode.

Table 2.2: Metrological parameters of a sensor

Characteristic	Description
Sensitivity	The quotient of the output quantity ΔY and the corresponding input quantity ΔX : $S = \Delta Y / \Delta X$ (Output signal variations/ Input signal variations)
Selectivity	The ability of a sensor to detect a target element in the presence of many others contained in the same medium, the selectivity translates the sensor's capability to be insensitive towards elements that are not the object of the measurement, but which influence its output.
Saturation	The step is when the output signal cannot exceed a maximum value, regardless of the input value.
LOD (Limit Of Detection)	The lowest concentration of an analyte can be detected with an acceptable uncertainty. It is calculated based on the equation: $LOD = 3\sigma/S$ Where σ and S are respectively the standard deviation and the slope of the calibration curve's linear range.
LOQ (Limit Of Quantification)	The lowest concentration of an analyte can be quantified with an acceptable uncertainty. It is calculated based on the equation: $LOQ = 10\sigma/S$ Where σ and S are respectively the standard deviation and the slope of the calibration curve's linear range.
LOL (Limit Of Linearity)	The linearity limit corresponds to the highest concentration that can be quantified with sufficient certainty.
Reproducibility	The agreement closeness among the results of the same magnitude measurements, where individual experiments are carried out according to different methods, using various instruments, by several persons, in different laboratories, and after fairly long time intervals compared to a single measurement duration.

Repeatability	The agreement nearness between successful measurement results of the same quantity with the same method, by the same person, with the same measuring instruments, in the same laboratory, and at fairly short time intervals.
Speed	The quality expresses the manner of monitoring input variations over time.
Influencing quantities	The quantities which, when applied, are liable to modify the sensor's metrological characteristics. They can be of different origins, e.g. mechanical, chemical, thermal, electrical...etc.
Range	It specifies the limits of the input in which it can vary.
Linearity	It's specified in terms of percentage of nonlinearity showing deviation from ideal situation.

2.2.3.1 Optical sensors

A wide variety of optical methods (*Surface Plasmon Resonance (SPR)*, *Optical Waveguide Light mode Spectroscopy (OWLS)*, and *Fluorescence Spectroscopy (FS)*) have been used for optical sensors' development. Optical-based sensors are centered on physical phenomena i.e. fluorescence and refractive index variations. They have become progressively popular in recent years with many commercially available devices. One of their main advantages is the ability to non-destructive probing of surfaces and films, besides having good sensitivity, robustness, and low response time. Likewise, they allow in-situ and real-time measurements, as well as simultaneous detection of several targets [21].

One subtype of optical sensors is the so-called 'colorimetric sensors' which are not based on surface-related optical properties, these sensors are relying on the color change of a solution containing the analyte to be detected and some functionalized nanoparticles, their optical absorption is highly affected by the coupling of interparticle surface plasmon and the nearby media's refractive index. The nanoparticles' accumulation or redispersion triggered by target analytes causes an important color variation. However, for attaining decent sensing characteristics, the nanoparticles are frequently functionalized with recognizing molecules that specifically bind with the analytes to be detected [21].

2.2.3.2 Electrochemical sensors

The electrochemical measurements are centered on electrons' exchange between electroactive species in solution (molecules or ions) and an electrode under well-defined analytical conditions. Electrochemical sensors are categorized according to the involved electrochemical method in the detection application, namely: *potentiometry*, *amperometry*, *conductometry*, and *impedance spectroscopy*.

The potentiometric sensing is the working principle of pH and Ion Selective Electrodes (ISEs), usually, the working electrode (WE) develops a variable potential, proportional to the concentration/activity of a specific element in solution, a local equilibrium is established at the

sensor's surface, and leads to the generation of a proportional potential to the logarithm of the element's the concentration/activity, according to Nernst equation (Eq. (2.1)) [22,23].

$$E_p = E^0 + \frac{RT}{nF} \ln\left(\frac{a_{ox}}{a_{red}}\right) \quad (2.1)$$

Where E_p represents the redox potential, E^0 is the standard normal redox potential, R is the universal gas constant (8.314 J/K.mol), (a_{ox}/a_{red}) is the activity ratio of the oxidant and reductant, n is the number of exchanged electrons during the reaction, T is the absolute temperature in Kelvin, and F is the Faraday's constant (96,500 C/mol).

The principle of *amperometric sensors* relies on determining an intensity-potential curve obtained by applying a sufficiently large voltage between the working and the reference electrodes, this curve has a diffusion plateau for which the intensity is proportional to the reduced or oxidized species' concentration [24].

Conductometric sensors are based on electrical conductivity measurement; for low concentrated solutions, the conductivity γ is roughly proportional to the electrolyte concentration (Eq. (2.2)). Since these sensors detect all ionic species present in the solution, their use requires a good knowledge of the solution's ionic composition since they have no intrinsic selectivity [24].

$$G = \frac{\gamma A}{l} \quad (2.2)$$

Where G is the conductance in Siemens (S); γ is the specific conductance or conductivity, expressed in S/cm, A is the area (cm²), and l is the length (cm).

The *impedimetric sensors* are based on the impedance measurement of an electrochemical cell employing electrochemical impedance spectroscopy, which allows controlling the charge transfer process at the electrode/electrolyte interface. In practice, the measurement is carried out in a three electrodes cell configuration, composed of a working electrode on which the detection platform is deposited, reference, and auxiliary electrodes. Indeed, an imposed potential with a sinusoidal low amplitude, between the reference and the working electrode, allows the measurement of the generated current between the working and the auxiliary electrode, and the ratio of the applied voltage to the measured current intensity defines the impedance of the electrochemical system. The latter can be represented by an equivalent electrical circuit depending on the system's type (faradic or non-faradic). This circuit makes it possible to express the electrical parameters defining the charge transfer phenomenon occurring at the electrode/electrolyte interface. In sensor systems, the electrical parameters vary

as there will be interfacial changes arising from interactions occurring at the working electrode's surface.

2.2.3.3 Piezoelectric sensors

Piezoelectric or acoustic wave sensors are based on the inverse piezoelectric effect, allowing an acoustic wave generation and detection, whose type depends on the used material's nature and geometry. The operating principle is established on measuring the disturbances occurring by the acoustic wave when it propagates in/on the material's surface. Typically, the output signal is in the form of frequency, phase, or amplitude variation as a function of time. Depending on the piezoelectric material's nature and crystallographic cut, piezoelectric sensors can be generated in three subtypes: Surface Acoustic Wave (SAW), Guided Wave (GW), and Bulk Acoustic Wave (BAW) sensors.

2.2.3.3.1 Surface Acoustic Wave (SAW) sensors

Their operating principle relies on the measurement of disturbances that occurred by the propagating acoustic wave along the piezoelectric substrate's surface. Indeed, interactions between the sensing platform and the target element, produce a mass effect; accordingly, a modification of the acoustic wave's propagation characteristics [25].

2.2.3.3.2 Guided Wave (GW) sensors

GW or Love waves are regularly guided in a thin film 'guiding layer' deposited on a piezoelectric substrate e.g. quartz which is considered to be semi-infinite concerning the wave, this later is then coupled into the guiding layer, which is rigidly linked to the substrate [25].

2.2.3.3.3 Bulk Acoustic Wave (BAW) Sensors

Quartz crystal microbalance (QCM)

The *QCM* is a technique based on a resonant quartz crystal (**Fig. 2.4**), whose surface is equipped with two electrodes (made of gold), one of which is functionalized employing a reception layer dedicated to specific recognition of target analytes [26].

The *QCM sensor's* principle relies on vibrating a piezoelectric quartz crystal at one of its resonant modes, by applying an alternative potential between its two electrodes. Any adsorbed mass on the recognition layer (sensing material) deposited on one or both electrodes causes a change in the resonant frequency [27].



Fig. 2.4: Structure of a QCM resonator.

The established equation by *Sauerbrey* in 1959 (Eq. (2.3)) [28] links the mass variation effect Δm on the electrode's surface and the frequency variation, noted Δf , as follow:

$$\frac{\Delta f}{f_0} = \frac{-2\Delta m_s}{\rho_q \lambda_0} \quad (2.3)$$

where λ_0 is the wavelength: $\lambda_0 = v_p / f_0$, v_p is the phase velocity/ transverse volume wave's speed: $v_p = (\mu_q / \rho_q)^{1/2}$; f_0 is the crystal's fundamental frequency (MHz), Δf is the resonance frequency variation (Hz), Δm_s is the surface mass variation (kg/m^2), μ_q is the quartz transverse elastic stiffness modulus, and ρ_q is the quartz density (kg/m^3).

The occurring piezoelectric phenomenon is attributable to the appearance of an electric potential on the crystal's surface if it undergoes the least mechanical deformation. Likewise, if the crystal is placed into an oscillating electrical field, it acquires an identical vibration frequency, in other terms, any changes in mass Δm occurring on the crystal's surface cause a proportional decrease in its vibration frequency Δf .

Electromagnetic piezoelectric sensor (EMPAS)

The EMPAS standing for the electromagnetic piezoelectric sensor is an ultra-high frequency device reaching frequencies up to 1.06 GHz. Unlike the QCM, the EMPAS needs no electrode connection for the quartz disk (electrode-less), its acoustic shear wave is induced by an AC-magnetic coil, generally situated 30 μm below the substrate. The ultra-high frequency EMPAS can easily reach higher analytical sensitivity if applied for sensor applications by simply attaining upper-frequency overtones up to the 53rd harmonics. Currently, our group employed EMPAS for detecting biological macromolecules comprising β -casein [29], and extracellular vesicles [30].

2.3 Applications of sensing materials

The modification of electrodes offers a significantly enhanced detection performance compared to usual unmodified ones [31]. Many coating materials are used for the recognition

and detection of target elements including nanostructures, biological platforms, or else chemical layers (polymers, small organic molecules, macrocyclic crown-ethers, cyclodextrins, calixarenes, and resorcinarenes) [32,33]. Frequently, the electrodes' functionalization is carried out either by adsorption interactions, covalent bonding, or dispersion within a conductive matrix. Targeting heavy metals detection, researchers vastly explored some receptor layers to improve the electrodes' sensitivity and selectivity, hence, illustrations of recent studies are deliberated.

2.3.1 Nanostructures

Metallic and carbon nanomaterials showed great electroanalytical interests thanks to their high specific surface area [34,35]. The nanoparticles' structuring on the electrode's surface is the key parameter for achieving remarkable sensing performances. Gold nanoparticles (AuNPs) are widely used in trace elemental analysis [36], e.g. *Li et al.* employed AuNPs to detect As^{3+} in real water samples reaching a detection limit of $1.3 \times 10^{-9} \text{ mol.L}^{-1}$ [37]. A nafion-l-leucine-graphene oxide layer was deposited on an Au electrode for determining As^{3+} in river water, the system provided a detection limit of $6.7 \times 10^{-6} \text{ mol.L}^{-1}$ [38]. A bi-ionic liquid-electrochemically reduced graphene oxide layer for detecting Cd^{2+} was fabricated, and a detection limit of $26.7 \times 10^{-9} \text{ mol.L}^{-1}$ was achieved [39]. A nitrogen-doped graphene layer for the heavy metals detection in tap water was constructed, and the sensor gave detection limits of 30×10^{-9} , 2×10^{-9} , 1×10^{-9} , and $10 \times 10^{-9} \text{ mol.L}^{-1}$, for Cd^{2+} , Pb^{2+} , Cu^{2+} , and Hg^{2+} , respectively [40]. Other studies investigated Hg^{2+} [41,42], Pb^{2+} [43,44], and Cr^{6+} sensing [45], while other heavy metals were sensed via graphene-based electrodes [46,47].

2.3.2 Biological platforms

The biosensing platform's choice depends on its specificity, stability, and the nature of targets to be analyzed [48,49]. Innovative biosensors have known wide applications comprising heavy metals detection (esp. Ag^+ ions), e.g. *Lee* and coworkers fabricated a silver-specific cytosine DNA piezogravimetric sensor reaching a detection limit of $0.1 \times 10^{-9} \text{ mol.L}^{-1}$ [50]. For the same ion, a hybridized DNA sensor was used [51], and another DNA biosensor showed a $2 \times 10^{-12} \text{ mol.L}^{-1}$ as detection limit [52]. An oligonucleotide-Gold nanoparticles (AuNPs) piezogravimetric sensor was fabricated for sensing Hg^{2+} , the system offered detection limits of $4 \times 10^{-9} \text{ mol.L}^{-1}$ (frequency) and $7 \times 10^{-9} \text{ mol.L}^{-1}$ (dissipation) [53]. An apta-sensor modified AuNPs for determining Cu^{2+} in lake and tap waters was invented, it reached a detection limit of $0.1 \times 10^{-12} \text{ mol.L}^{-1}$ [54]. A single-stranded DNAzyme sensor was developed to detect Pb^{2+} , and a detection limit of $0.25 \times 10^{-9} \text{ mol.L}^{-1}$ was gotten [55]. Hg^{2+} , Pb^{2+} , and Cd^{2+} were sensed

via a whole-cell-based biosensor [56], and the same metals ions were detected using a screen-printed electrode-bacterial biosensor [57].

2.3.3 Polymers

The (electro)deposition of polymers onto electroactive electrodes' surfaces denotes a vast research field [58,59]. Polymers' sensors are usually dedicated to Cu^{2+} detection, such as the polyaniline sensor developed by *Deshmukh et al.* [60]. A year later, they combined polyaniline and single-walled nanotubes reaching a detection limit of $1.4 \times 10^{-6} \text{ mol.L}^{-1}$ for Cu^{2+} ions [61]. Nowadays, the trending in polymers-based heavy metals sensors, is the so-called Ion Imprinted Polymers (I.I.Ps), such as the one developed by *Wei et al.*, their Cu^{2+} sensor exhibited a detection limit of $0.15 \times 10^{-6} \text{ mol.L}^{-1}$ [62]. Another Cu^{2+} I.P. sensor showed a detection limit of $7.4 \times 10^{-11} \text{ mol.L}^{-1}$ [63], and a p-phenylenediamine I.I.P. was constructed and reached a detection limit of $2.7 \times 10^{-9} \text{ mol.L}^{-1}$ [64]. A piezogravimetric polymer-based copper sensor was fabricated presenting a detection limit of $0.8 \times 10^{-9} \text{ mol.L}^{-1}$ [65]. Lead ions were sensed via a cysteine-graphene oxide /polypyrrole sensor, which showed a detection limit of $3.4 \times 10^{-9} \text{ mol.L}^{-1}$ [66]. Devoted to detecting Pb^{2+} , Cr^{3+} , Cu^{2+} , and Cd^{2+} , a piezogravimetric polymer grafted sensor was developed [67].

2.3.4 Macrocyclic compounds

Macrocycles as crown ethers, cyclodextrins, calixarenes, and resorcinarenes, have received immense consideration in heavy metals sensing applications due to their special three-dimensional shape that allows the formation of interest cavities for entrapping the ions of interest. In the next paragraphs, examples of heavy metals detection studies based on these ionophores are deliberated.

2.3.4.1 Crown ethers

Discovered accidentally in the 60s by *Pedersen* [68] (Nobel Prize in 1987, shared with *Cram* and *Lahn*), crown ethers are monocyclic compounds comprising oxygen atoms incorporated into the carbon skeleton (**Fig. 2.5**). This definition was enlarged to cover macrocyclic ethers containing azote and sulfur heteroatoms [69], acknowledging their complexing affinity towards alkaline and alkali metals ions, the crown ethers-based sensors are widely focusing on detecting K^+ [70,71], Na^+ [72], and Ag^+ [73]. Heavy metals ions sensing applications were also reported, e.g. an aza-crown ether sensor was fabricated to detect Cu^{2+} , the sensor exhibited a linear range from 7.9×10^{-9} to $1.2 \times 10^{-6} \text{ mol.L}^{-1}$ and a detection limit of $1.6 \times 10^{-9} \text{ mol.L}^{-1}$ in aqueous solutions [74], the same ion was sensed using a ferrocenyl-immine sensor, which showed a linear range of 0.16×10^{-6} - $1.1 \times 10^{-6} \text{ mol.L}^{-1}$, and a detection limit of $1.7 \times 10^{-9} \text{ mol.L}^{-1}$ [75], another ferrocenyl naphthoquinone sensor was fabricated for the detection of Ca^{2+} and Ba^{2+} [76], and a mono aza-

crown ether sensor to detect Cd^{2+} showed a linear range from 1.5×10^{-5} to $6.5 \times 10^{-5} \text{ mol.L}^{-1}$, and a detection limit of $4.5 \times 10^{-6} \text{ mol.L}^{-1}$ [77].

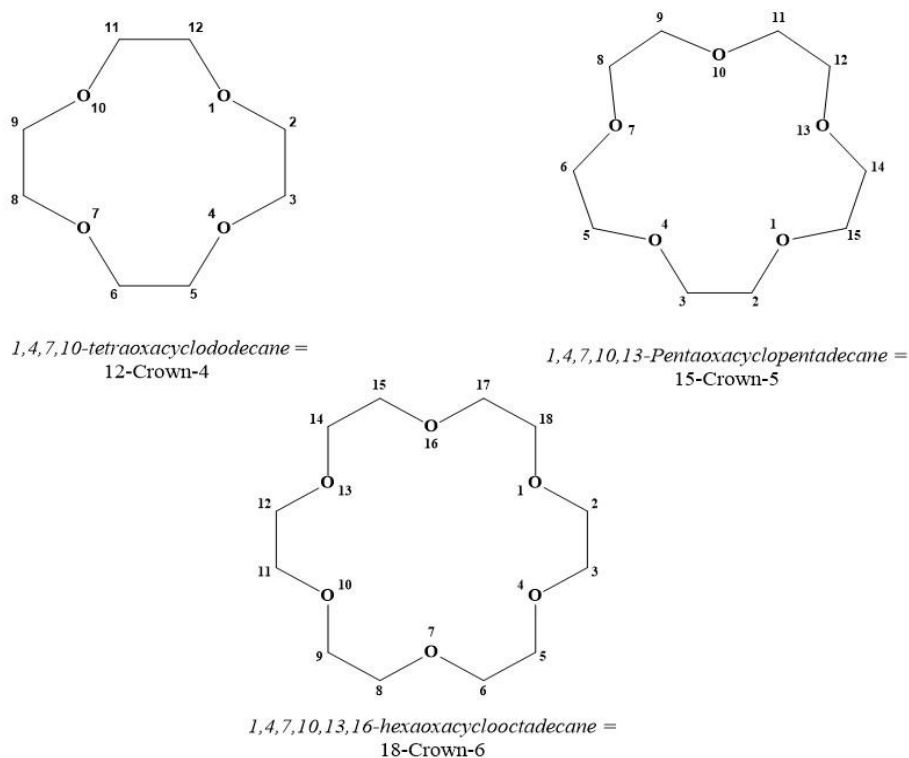


Fig. 2.5: Common crown ethers structures.

2.3.4.2 Cyclodextrins

Villiers (1891) isolated a crystalline substance while studying the starch breakdown and determined its composition: $(\text{C}_6\text{H}_{10}\text{O}_5)_3 \cdot 3\text{H}_2\text{O}$, the substance was named 'Cellulosin' which is in fact 'Cyclodextrin' [78]. Cyclodextrins (CDs) are cyclic ring-shaped oligosaccharides, formed of six to twelve glucose units [79-81]. The well-known CDs are composed of six, seven, and eight D-glucopyranosyl units respectively for the α -, β - and γ -CD forms.

CDs and their derivatives were extensively used to heighten the selectivity and sensitivity of heavy metals sensors [79,80]. For instance, a β -CD/Rotaxane sensor was invented to detect Hg^{2+} , Cu^{2+} , and Pb^{2+} , the best sensing performance was revealed for Hg^{2+} with a detection limit of $0.1 \times 10^{-6} \text{ mol.L}^{-1}$ [82]. A polymeric CD fluorescent sensor for monitoring Cd^{2+} ions in water and food samples was prepared, it exhibited a linear range from 4.4×10^{-9} to $44.5 \times 10^{-9} \text{ mol.L}^{-1}$ and a detection limit of $0.6 \times 10^{-9} \text{ mol.L}^{-1}$ [83]. A β -CD/Multi-walled carbon nanotubes sensor was fabricated to detect Pb^{2+} in drinking water, the sensors reached detection limits of $4.34 \times 10^{-9} \text{ mol.L}^{-1}$ and $11.1 \times 10^{-9} \text{ mol.L}^{-1}$ for the physically and chemically modified electrodes respectively [84]. A reduced graphene oxide/ β -CD sensor was prepared for detecting Cu^{2+} in synthetic water, and a detection limit of $2.8 \times 10^{-9} \text{ mol.L}^{-1}$ was obtained within a linear range

from 3×10^{-8} to 1×10^{-4} mol.L⁻¹ [85]. A bismuth film/Hydroxypropyl β -CD-Reduced graphene oxide/Nafion sensor was constructed to simultaneously detect Pb²⁺ and Cd²⁺, a linear range of $0.1-9 \times 10^{-9}$ mol.L⁻¹ and a detection limit of 0.09×10^{-9} mol.L⁻¹ were achieved for Pb²⁺, while a linear range of $0.5 \times 10^{-9}-9 \times 10^{-9}$ mol.L⁻¹ and a detection limit of 0.07×10^{-9} mol.L⁻¹ were attained for Cd²⁺ [86]. The CDs-based sensors are not restricted to heavy metals recognition only, but detection studies on acetaminophen [87] and estrogen [88] were also reported.

2.3.4.3 Calixarenes/ Resorcinarenes

2.3.4.3.1 Introduction

As an extension of *A. Bayer's* work on resin formation via phenols and aldehydes condensation (1872), the two Austrian Chemists *E. Ziegler* and *A. Zinke* arrived at synthesizing the first 'Calixarene' by the year 1944 [89]. They observed a crystalline solid, having a much higher melting point compared to that of resins. Later on, in 1958, they determined its molar mass which corresponds to the exact p-tert-butylcalix[4]arene's molar mass. In the same year, two English Chemists, namely: *U. Hunter* and *B. Hayes*, reached carrying out a sequential total synthesis of Calix[4]arene in 10 steps [90]. Numerous scientists were suggesting that Calix[4]arene has isomeric conformations including *N. Megson* [91], *A. Zinke*, and *R. Ott* [92], these suggestions were later confirmed by *J. Cornforth* [93].

Aiming at reproducing specific chemical reactions, generally created at some enzymes' active sites, in 1972, *C. Gutsche* resumed the work on calixarenes and developed the chemistry behind [94]. He showed that these macrocycles can be synthesized with good yields, different cyclic sizes, and can be easily purified, via functionalization with branched alkanes and tert-butyl groups, he also highlighted that the phenols' para position can be easily functionalized. By the year 1978, *C. Gutsche* was the first scientist calling these macrocyclic elements 'Calixarenes', inspired by the word 'Calix' meaning vase in the ancient Greek language, and 'arene' signifying the presence of aromatic nuclei in the molecule [95]. His work on calixarenes opened a novel macrocyclic chemistry era and was re-joined by many research teams such as the Italian *Ungaro* group [96] and the *Kämmerrer's* group in Germany [97].

Calix[n]arenes/[n]resorcinarenes are polycyclic macromolecules formed of 'n' phenolic/resorcinolic units, linked typically by methylenic bridges at the hydroxyl groups' ortho position (**Fig. 2.6**). Their synthesis is based on cyclo-condensation reactions via two main processes: *Mixing aldehydes and phenols* in an alkali medium is conducive to calixarenes' production [89] while *condensing aldehydes and resorcinol's* in an acidic catalyzed medium allow access to calixresorcinarenes (Resorcinarenes) [98].

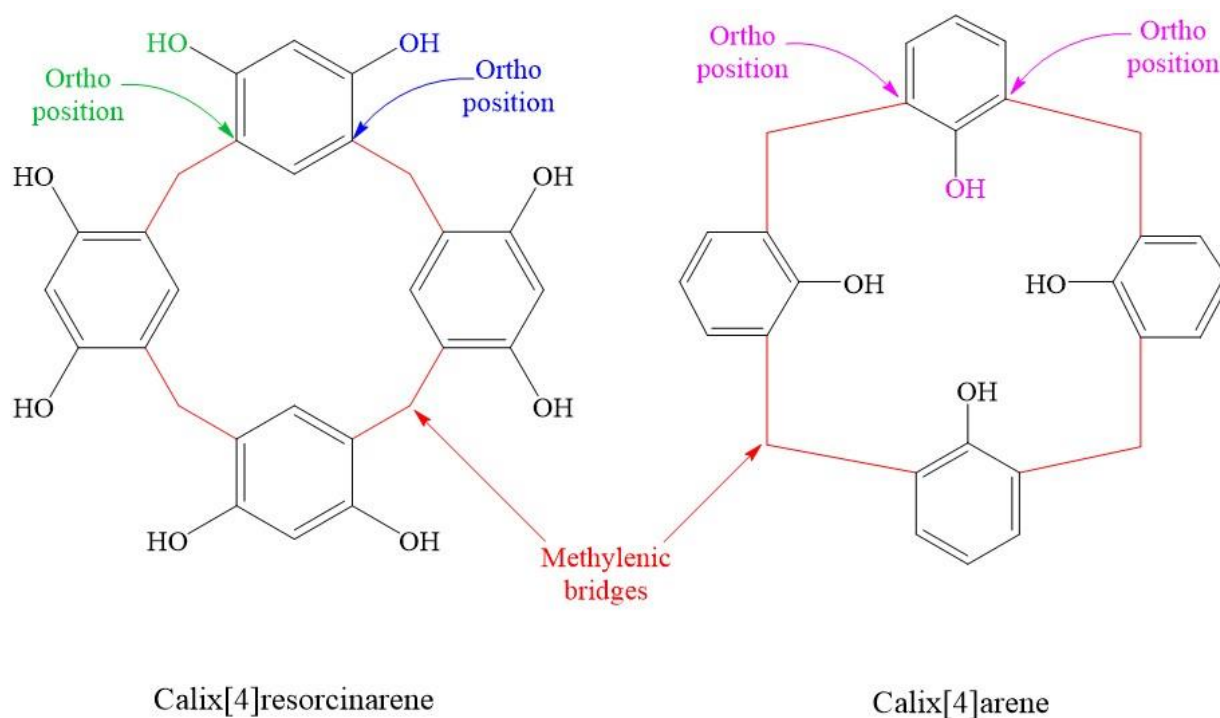
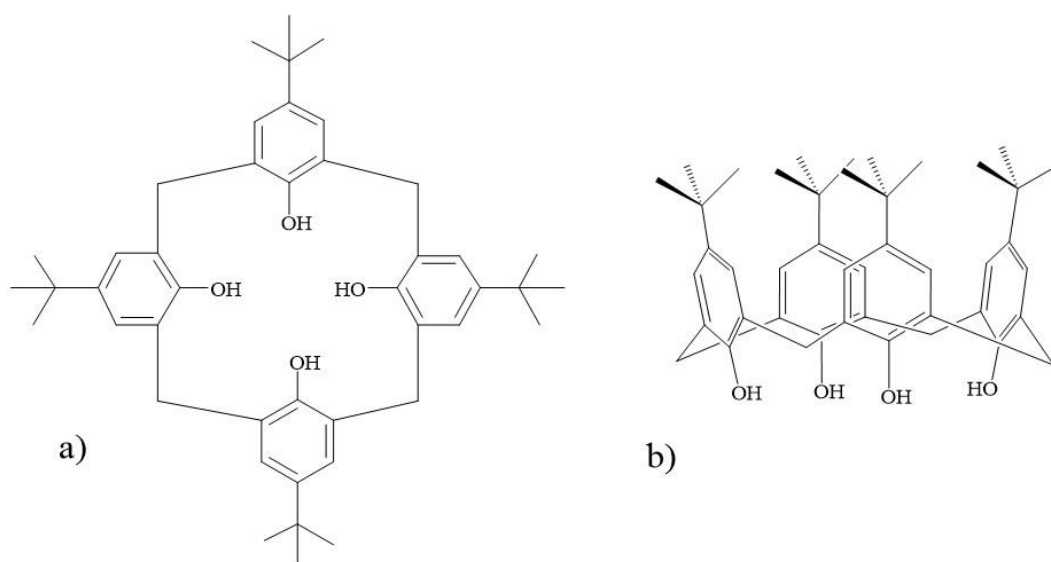


Fig. 2.6: Molecular structures of calix[4]resorcinarene and calix[4]arene

The nomenclature of Calix-based macrocycles can be labeled as follow: the number ‘n’ of phenolic/resorcinolic units is indicated in square brackets between ‘Calix’ and ‘arene/resorcinarene’ to distinguish the different macrocyclic sizes. As well, to specify from which substituent the compound is driven, the prefix ‘substituent’ is normally added before the Calix[n]arene/Calix[n]resorcinarene. For example, a four phenolic unit compound derived from the ‘*p*-tert-butylphenol’ is usually called ‘*p*-tert-butylcalix[4]arene’. However, the specific positions of substituents in a calixarene/resorcinarene molecule are displayed by numbers, illustrating this, the ‘*p*-tert-butylcalix[4]arene’ (**Fig. 2.7**) is represented by ‘5,11,17,23-Tetra-*t*-butyl-25,26,27,28-tetrahydroxycalix[4]arene’ [99].

The structure of calixarenes issued from phenolic derivatives, is by convention represented with hydroxyl groups, constituting the hydrophilic ‘Lower Rim’, pointing downwards ‘Endo side’, the substituents are then placed at the ‘Exo side’ pointing upwards, usually called hydrophobic ‘Upper Rim’ (**Fig. 2.8**) making them amphiphilic molecules having hydrophobic cavities.

H. Kämmerer studied the calixarenes/resorcinarenes’ flexibility by NMR spectra at different temperatures, he discovered that these compounds are much stretchy to adopt different conformations (cone, partial cone, 1,2-alternate and 1,3-alternate (**Fig. 2.9**)), though, the cone conformation is the predominant [97]. Further studies showed that the flexibility of functionalized calixarenes rises with increasing the central annulus size [100,101].



5,11,17,23-Tetra-*t*-butyl-25,26,27,28-tetrahydroxycalix[4]arene =
p-*tert*-Butylcalix[4]arene

Fig. 2.7: a) Top and b) side views of p-*tert*-butylcalix[4]arene's cone conformation.

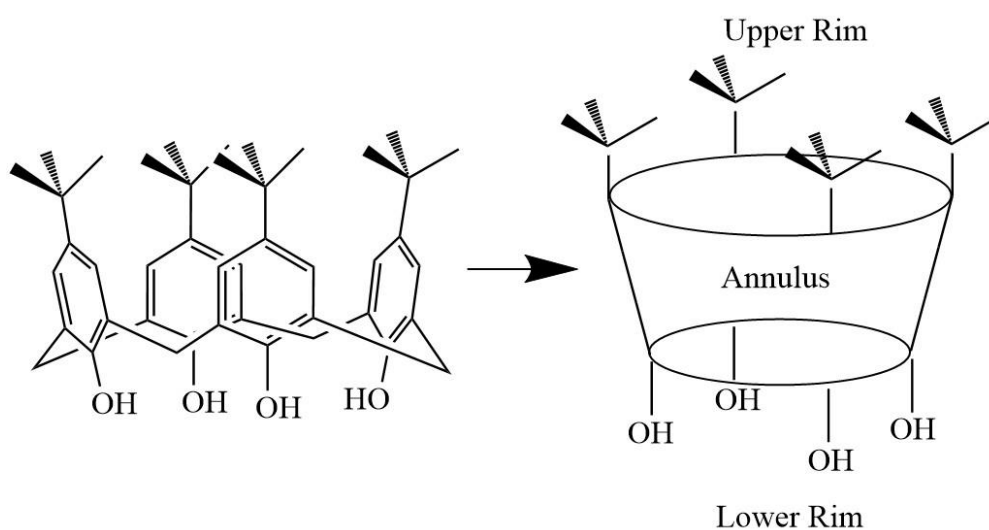


Fig. 2.8: Cone-conformation of p-*tert*-butylcalix[4]arene emphasizing its different parts (Annulus, upper and lower rims).

2.3.4.3.2 Applications in complexation and extraction

The production of calixarenes and resorcinarenes with a designed three-dimensional cavity, able to host molecules and ions, has attracted scientists' attention during the last two decades, this rising concern is owing to their capability of forming reversible inclusion complexes, especially with cations (Fast complexation-decomplexation kinetics).

For illustration, **Table 2.3** highlights some recent applications of Calix-based compounds as extracting and complexing agents.

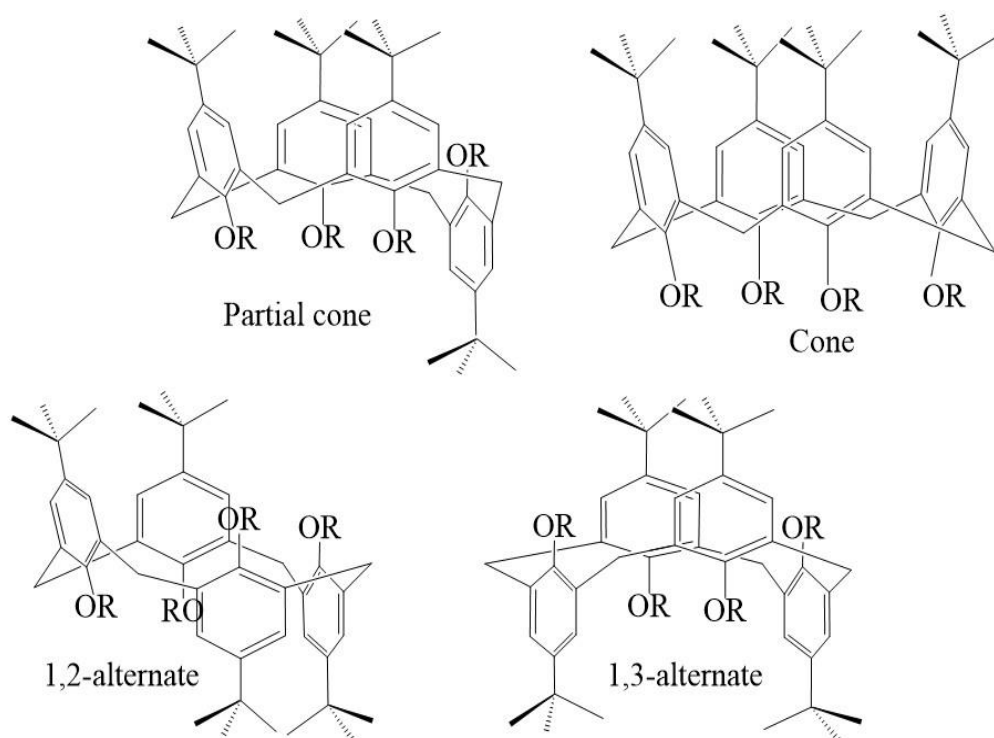


Fig. 2.9: Different conformations of a typical calix[4]arene.

Table 2.3: List of Calix-based compounds as extracting, coordinating, and complexing agents.

Ionophore	Target elements	Method	Results	Refs
Primidyl-thioamide functionalized calix[4]arene	Cu^{2+} , Co^{2+} , Ni^{2+} , Hg^{2+} , Pb^{2+} , Cd^{2+}	Extraction	Selective affinity and better efficiency towards Pb^{2+} and Hg^{2+}	[102]
Carboxylic acid-modified calix[4,6]arenes	Eu^{3+} and Nd^{3+}	Extraction	Calix[6]arene showed higher extraction ability	[103]
25,26,27,28-tetrapropoxycalix[4]arene-5,11,17,23-tetracarboxylic acid	Cu^{2+}	Complexation	Fabrication of the first metal-organic coordination network	[104]
3-pyridylmethyl-calix[4]arenes	Cu^{2+} and Zn^{2+}	Complexation	Formation of monomeric, dimeric, and oligomeric/polymeric elements	[105]
O-substituted p-tert-butylcalix[8]arene and O-substituted p-isononylcalix[8]arene	^{137}Cs and ^{241}Am	Extraction	The selective extraction was influenced by the alkyl substituents	[106]
Single bridged biscalic[6]arene	Na^+ , K^+ and Cs^+	Extraction and membrane transport	Selectivity towards K^+ ions	[107]
N, N-dihexylacetamide calix[4]arene, and N-hexyl-N-methyl acetamide calix[4]arene	Li^+ , Na^+ , K^+ and Rb^+	Complexation	Formation of 1:1 complexes	[108]
Two-story calix[6]arene	Zn^{2+} and Cu^{2+}	Complexation	6-coordinate-Zn(II) and 5-coordinate-Cu(II) complexes were formed	[109]
	Pb^{2+} , Cd^{2+} , Co^{2+} , Ni^{2+} ,	Extraction	Selectivity towards Cd^{2+} ions	[110]

Bis(1-(2-furoyl) piperazine
calix[4]arene Cu^{2+} and
 Zn^{2+}

2.3.4.3.3 Applications in heavy metals' detection and sensing

For years, calixarenes served as attractive materials for detecting metal ions in several matrixes encompassing water due to the easiness of functionalization, cavity size alterations, and selective binding affinities towards neutral molecules and charged ions.

The first 'Calixarene-Ion Selective Electrode (1986) was based on (methyl and ethyl ester)-p-tert-butylcalix[4]arenes ionophores (**Fig. 2.10**), the proposed sensors showed high selectivity towards Na^+ over alkali ions as K^+ , Li^+ , and Cs^+ (100 fold discrimination over K^+), allowing this ion-selective electrode (ISE) to potentially estimating Na^+ amounts in blood and serum [111]. Since then, calixarene neutral carriers were extensively exploited aiming at monitoring Na^+ ions by the leading *McKervey* group. In 1988, they succeeded to prepare another sodium ISE based on methyl-p-tert-butylcalix[4]aryl acetate, the detection platform showed high selectivity towards sodium ions, a fast response time of 3s, and a near Nernstian response in the concentration range from 10^{-1} to 10^{-4} mol.L $^{-1}$ [112]. One year later, they employed ester and ketone p-tert-butylcalix[4]arene derivatives targeting the same ion, the selectivity was improved and the sensor reached a detection limit of 10^{-5} mol.L $^{-1}$ [113].

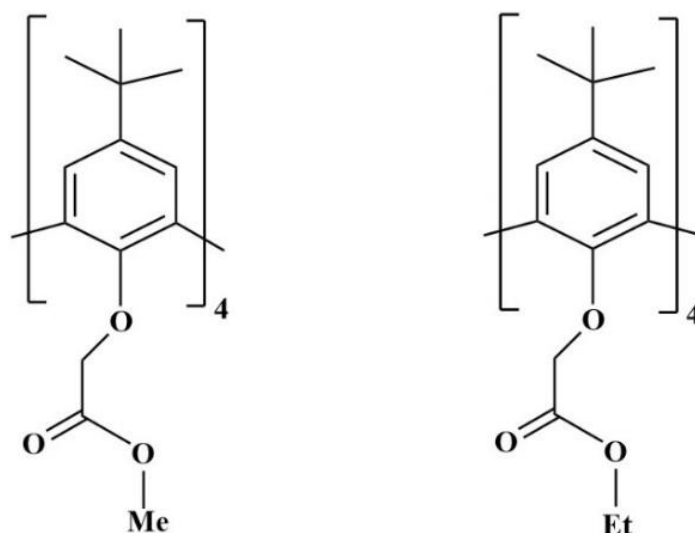


Fig. 2.10: Structures of employed ionophores in the 1st Calix-based ISE [110].

The synthesis of four calixarene derivatives for fabricating silver ions selective electrodes was effectively carried out by the same research team, where the selectivity studies showed high selectivity towards Ag^+ over K^+ , Na^+ , and other transition metal ions, the achieved detection limits were between 10^{-4} and $10^{-3.8}$ mol.L $^{-1}$ [114]. Later on, they prepared sodium-selective electrodes (Na^+ -ISEs) based on nineteen ionophores comprising bridged and (un)symmetrical

Calix[4]arene derivatives, either functionalized by thioether, amide, amine, ketone, or ester groups. Out of nineteen tested electrodes, four exhibited high selectivity and sensitivity towards sodium ions over alkali, alkaline, and ammonium ions within a vast lifetime superior to 200 days [115]. The *McKervey* group did not restrict its inventions of Calix-based ion-selective electrodes to monitor alkali and alkaline ions only, but they explored heavy metals as well, such as the lead ions selective electrode based on Calix-phosphine derivatives, the sensor reached near Nernstian slope, response time less than 10s, and a detection limit of $1 \times 10^{-6} \text{ mol.L}^{-1}$ [116]. For detecting the same ion, seven double-armed p-tert-butylcalix[4]arenes were synthesized and fully characterized by *Liu et al.*, these neutral carriers were employed in preparing ion-selective electrodes to sense several metal ions, however, they were all Pb^{2+} selective with a fast response time ranging from 10 to 15 s, the detection limits were between $10^{-7.2}$ and $10^{-5.7} \text{ mol.L}^{-1}$ within linear ranges from 10^{-7} to $10^{-1} \text{ mol.L}^{-1}$ [117]. Applications of calixarenes/resorcinarenes intended to metal ions sensing have fascinated the researchers' attention, **Table 2.4** is summarizing illustrations of Calix-based ion-selective electrodes, chemically modified electrodes, optical and piezogravimetric chemosensors for monitoring these ions during the past decade.

Table 2.4: Calix-based chemosensors for metal ions detection

Ionophore	Technique	Target ions	Detection limit (mol.L^{-1})	Linear Range (mol.L^{-1})	Comments	Refs
Cone-shaped calix[4]arene	Potentiometric Titration (ISE)	Hg^{2+}	4.10^{-7}	1.10^{-6} to 1.10^{-1}	-Detection in amalgam alloy and water samples. -Response time = 10 s. -pH working range: 1.5 to 4	[118]
Resorcinarene phosphoryl derivative	Electrochemical screening (Flow injection analysis)	Zn^{2+}	5.10^{-8}	1.10^{-7} to $1.2.10^{-6}$	-Application to real water samples. -Response time = 5s	[119]
Meso-octamethyl calix[4] pyrrole	Potentiometric Sensing (ISE)	Ti^{3+}	8.10^{-7}	1.10^{-6} to 1.10^{-2}	-Determination in industrial wastewaters. -Highly selective. -pH working range: 1 to 3	[120]
p-tert-butylcalix[6]arene	Potentiometric detection (ISE)	Cd^{2+}	---	97.10^{-6} to 1.10^{-1}	Applied to industrial wastewaters. -Highly selective. -Response time = 35 s. -pH working range: 2.8 to 6.2	[121]
Series of calix[4]arenes	Potentiometric sensing (ISE)	Tl^{+}	8.10^{-9}	1.10^{-6} to 1.10^{-2}	Highly selective. -Serious interference from Ag^{+} .	[122]

Chapter 2: State of the art

p-tert-butylcalix[8]arene tetracetone derivative	<i>Impedimetric detection (EIS)</i>	Cd ²⁺	1.10 ⁻⁷	---	-High sensitivity to Cd ²⁺ . -Au modified electrode.	[123]
Calix[4]arene derivative/ RGO	<i>Voltammetric sensor (SWV)</i>	Pb ²⁺ , Cd ²⁺ and Fe ³⁺	2.10 ⁻¹¹	1.10 ⁻¹⁰ to 1.10 ⁻⁸	-Sensing in pharmaceutical formulation. -Modified GCE.	[124]
p-tert-butylcalix[4]arene	<i>Voltammetric tests (DPASV)</i>	Pb ²⁺	1.8x.10 ⁻⁷	4.8.10 ⁻⁷ to 1.2.10 ⁻⁵	-Detection in industrial effluents and sewage water.	[125]
		Cu ²⁺	6.3.10 ⁻⁷	1.6.10 ⁻⁶ to 3.8.10 ⁻⁵	-SPCarbone modified electrode.	
		Hg ²⁺	2.4.10 ⁻⁷	4.9.10 ⁻⁷ to 1.2.10 ⁻⁵		
Cyrhretrenyl-calix[4]arene	<i>Voltammetric platform (SWASV)</i>	Cu ²⁺	4.7.10 ⁻¹⁰	1.6.10 ⁻⁷ to 2.8.10 ⁻⁶	-Determination in bivalve mollusks. -Modified GCE.	[126]
Dicarboxyl-calix[4]arene	<i>Voltammetric detection (DPV)</i>	Pb ²⁺	3.10 ⁻⁸	1.4.10 ⁻⁶ to 1.2.10 ⁻⁵	-Application to real water samples. -Modified Gold SPE.	[127]
BNPTHC Calix[4]arene	<i>Voltammetric sensing (DPV)</i>	Cu ²⁺	3.8.10 ⁻¹⁷	1.10 ⁻¹⁶ to 1.10 ⁻¹⁰	-Detection in spiked river water samples. - Modified gold electrode	[128]
		Cu ²⁺	4.7.10 ⁻⁸	1.6.10 ⁻⁵ to 3.1.10 ⁻⁵		
Thia-calix[4]arene	<i>Voltammetric analysis (DPASV)</i>	Cd ²⁺	3.6.10 ⁻⁸	8.9.10 ⁻⁷ to 8.9.10 ⁻⁶	- Applied to river water. -Modified GCE.	[129]
		Pb ²⁺	1.2.10 ⁻⁸	4.8.10 ⁻⁶ to 9.7.10 ⁻⁶		
1,3-alternate calix[4]arene bearing amino-thiadiazole tails	<i>Optical detection (Fluorescence)</i>	Ag ⁺	6.29.10 ⁻⁶	---	-Determination in physiological and aqueous samples. -High selectivity. -Formation of a (1:1) complex	[130]
Quinaldine-p-tert-butyl calix[4]arene	<i>Optical analysis (Colorimetry)</i>	Hg ²⁺	2.95.10 ⁻⁶	---	-Reversible sensing process.	[131]
Calix[4]arene bearing dansyl groups	<i>Optical sensing (Fluorescence)</i>	Hg ²⁺	1.10 ⁻⁷	---	-Multifunctional miniaturized sensor.	[132]
1,3-alternate calix[4]arenes containing pyrene moieties	<i>Optical tests (Colorimetry)</i>	Wide range of anions and cations	---	---	-For cations: Selectivity to Hg ²⁺ , Pb ²⁺ , Cu ²⁺ and Ni ²⁺ in (Acetonitrile-chloroform) media, and to Cu ²⁺ in (THF-H ₂ O) media - For anions: towards F ⁻ .	[133]
1,3-alternate thiacalix[4]arene bearing naphthyl groups	<i>Optical studies (Fluorescence)</i>	F ⁻	2.6.10 ⁻⁷	---	- A (1:1) complex was formed between the fluoroionophore and fluoride ions.	[134]
1,3-alternate calix[4]arene	<i>Optical sensing</i>	Cu ²⁺	1.05.10 ⁻⁶	---	-Highly selective to copper and sulfide ions.	[135]

Chapter 2: State of the art

comprising benzothiazole	(Fluorescence)	HSO ₄ ⁻	9.8.10 ⁻⁷	---	
Novel amino-pillar[5]arene	Optical analysis (Fluorescence)	Au ³⁺	7.10 ⁻⁸	---	- pH working range: 1-13.5 - Binding ratio of 2:1 (ionophores: Au ³⁺). [136]
C-dec-9-enylcalix[4]resorcinarene-O-(S-)-α-methylbenzylamine	Piezogravimetric detection (QCM-I)	Pb ²⁺	2.2.10 ⁻⁶	1.2.10 ⁻⁴ to 4.8.10 ⁻³	-The C-dec-9-enylcalix[4]resorcinarene-O-(R+)-α-methylbenzylamine based QCM sensor was much selective and sensitive towards Pb ²⁺ [137]
C-dec-9-enylcalix[4]resorcinarene-O-(R+)-α-methylbenzylamine		Pb ²⁺	1.4.10 ⁻⁶	2.4.10 ⁻⁵ to 2.4.10 ⁻³	
C-dec-9-enylcalix[4]resorcinarene-O-(S-)-α-methylbenzylamine	Piezogravimetric detection (QCM-I)	Cd ²⁺	9.8.10 ⁻⁶	3.6.10 ⁻⁵ to 2.2.10 ⁻³	Selectivity towards copper ions was seen for both Calix-based QCM sensors [138]
		Hg ²⁺	3.2.10 ⁻⁶	9.9.10 ⁻⁶ to 1.2.10 ⁻³	
		Cu ²⁺	2.5.10 ⁻⁶	7.9.10 ⁻⁶ to 4.10 ⁻³	
C-dec-9-enylcalix[4]resorcinarene-O-(R+)-α-methylbenzylamine		Cd ²⁺	7.9.10 ⁻⁶	2.7.10 ⁻⁵ to 8.9.10 ⁻³	
		Hg ²⁺	9.9.10 ⁻⁷	4.9.10 ⁻⁶ to 4.9.10 ⁻³	
		Cu ²⁺	1.7.10 ⁻⁶	7.9.10 ⁻⁶ to 1.6.10 ⁻²	
		Cd ²⁺	2.8.10 ⁻⁶	2.2.10 ⁻³ to 8.9.10 ⁻³	
C-dec-9-en-1-ylcalix[4]resorcinarene	Piezogravimetric detection (QCM-I)	Hg ²⁺	1.8.10 ⁻⁶	4.9.10 ⁻⁶ to 2.5.10 ⁻³	- The C-dec-9-en-1-yl-Calix[4]resorcinarene was selective to Cd ²⁺ , whereas the C-undecyl Calix[4]resorcinarene presented binding preferences toward Cu ²⁺ and Pb ²⁺ [139]
		Cu ²⁺	9.10 ⁻⁶	3.1.10 ⁻⁵ to 1.2.10 ⁻²	
		Pb ²⁺	4.3.10 ⁻⁶	1.4.10 ⁻⁵ to 2.4.10 ⁻³	
		Cd ²⁺	1.5.10 ⁻⁵	4.4.10 ⁻⁵ to 8.9.10 ⁻³	
		Hg ²⁺	3.8.10 ⁻⁶	1.5.10 ⁻⁵ to 2.5.10 ⁻³	
C-undecyl calix[4]resorcinarene		Cu ²⁺	2.8.10 ⁻⁶	1.6.10 ⁻⁵ to 3.9. 10 ⁻³	
		Pb ²⁺	9.7.10 ⁻⁷	4.8.10 ⁻⁶ to 4.8.10 ⁻³	

2.4 The Hungarian scientific contribution to Ion Selective Electrodes (ISEs)

Since the early 60s, Prof. *Pungor Ernő* was one of the leading analytical chemists in the field of ISEs, owing to his invention of the first silver-iodide-based iodide selective electrode in 1961 [140]. Two years later, he replaced the fragile paraffin membranes in his electrodes with silicone rubber as a robust material and patented his invention [141]. The front page of the Hungarian patent of *Pungor Ernő* on heterogeneous ion-selective membranes is shown in **Fig. 2.11**. In 1965, and based on his patent, the first commercially accessible ISEs were produced in Hungary. And in 1973, he developed an ionophore-based ISE containing a polymeric membrane, where vancomycin was employed as an ionophore, and the membrane was silicon rubber, the developed ISE successfully worked for detecting potassium ions [142]. Since then, leading works on ISEs were achieved at the *Department of Inorganic and Analytical Chemistry, Budapest University of Technology and Economics* [143-148].



Fig. 2.11: The front page of the Hungarian patent of Pungor Ernő on heterogeneous ion-selective membranes [141].

C

Chapter 3: Methodology and experimental

Aiming to support the results and discussion part, the used chemicals, the ionophores' synthetic routes, and the measurements' procedures are detailed in this chapter. Besides describing the applied apparatuses for the ionophores chemical characterization, the interfacial complexation via Langmuir isotherms, and the heavy metals detection application.

3.1 Chemicals

The used chemicals in the experimental part of the thesis work are listed below:

Table 3.1: List of used chemicals in the thesis work.

<i>Name</i>	<i>Formula</i>	<i>Characteristics</i>	<i>Purchased from</i>
Acetone	C ₃ H ₆ O	Analytical grade	Reanal
Chloroform	CHCl ₃	Analytical grade /Stabilized with 1% of Ethanol	Molar Chemicals KFT
Hydrogen peroxide (30%)	H ₂ O ₂	Extra pure	Molar Chemicals KFT
Tetrahydrofuran (THF)	C ₄ H ₈ O	Extra pure	Molar Chemicals KFT
Acetonitrile (ACN)	CH ₃ CN	Extra pure	Merck
n-Hexane	C ₆ H ₁₄	Analytical grade	Carlo Erba
2-propanol	C ₃ H ₈ O	Analytical grade	Molar Chemicals KFT
Ethanol (96%)	C ₂ H ₆ O	Extra pure	Molar Chemicals KFT
Methanol	CH ₄ O	Analytical grade	Molar Chemicals KFT
Sulfuric acid (96%)	H ₂ SO ₄	Analytical grade	Molar Chemicals KFT
Hydrochloric acid (37%)	HCl	Analytical grade	Molar Chemicals KFT
Glacial acetic acid (+ 99 %)	CH ₃ CO ₂ H	Analytical grade	Sigma-Aldrich
Sodium hydroxide (+ 98 %)	NaOH	Analytical grade	Sigma-Aldrich
Ammonium acetate	CH ₃ CO ₂ NH ₄	Analytical grade	Merck
Ammonia (25%)	NH ₃	Analytical grade	Molar Chemicals KFT
Nitric acid (65%)	HNO ₃	Analytical grade	Molar Chemicals KFT
Hellmanex III	—	Alkaline cleaning concentrate	Hellma GmbH & Co. KG (Germany)
Pb(II) nitrate	Pb(NO ₃) ₂	99.99%	Sigma-Aldrich
Cd(II) nitrate tetrahydrate	Cd(NO ₃) ₂ ·4H ₂ O	98%	Sigma-Aldrich
Hg(II) chloride	HgCl ₂	99.5%	Sigma-Aldrich
Cu (II) nitrate trihydrate	Cu(NO ₃) ₂ ·3H ₂ O	Extra pure	Sigma-Aldrich

Mg(II) chloride hexahydrate	MgCl ₂ .6H ₂ O	Analytical grade	Molar Chemicals KFT
Al(III) nitrate nonahydrate	Al(NO ₃) ₃ .9H ₂ O	Analytical grade	Sigma-Aldrich
Ni(II) nitrate hexahydrate	Ni(NO ₃) ₂ . 6H ₂ O	Analytical grade	Reanal
Dried Zn(II) sulfate	ZnSO ₄ .H ₂ O	Analytical grade	BDH Chemicals Ltd.
K(II) sulfate	K ₂ SO ₄	99.5 %	Molar Chemicals KFT
K(I) chloride	KCl	+ 99 %	Sigma-Aldrich
Trans-2,cis-6-nonadienal (+96%)	C ₉ H ₁₄ O	d = 0.866	Sigma-Aldrich
Undecylenic aldehyde (95%)	C ₁₁ H ₂₀ O	d = 0.81	Sigma-Aldrich
(S)-(-)- α -Methylbenzylamine (p \geq 98%)	C ₈ H ₁₁ N	d = 0.952	Fluka Chemie GmbH
(R)-(+)- α -Methylbenzylamine (p \geq 98%)	C ₈ H ₁₁ N	d = 0.952	Fluka Chemie GmbH
Dodecanal	C ₁₂ H ₂₄ O	d = 0.831	Sigma-Aldrich
Paraformaldehyde	HO(CH ₂ O) _n H	Reagent grade	Molar Chemicals KFT
Resorcinol	C ₆ H ₆ O ₂	Analytical grade	Reanal
Ultra-pure water (Milli-Q grade water)	—	Resistivity/ Conductivity at 25°C: 18 M Ω .cm ⁻¹ / 5.5x10 ⁻⁶ S.m ⁻¹	—

3.2 Synthesis of ionophores

As discussed in *Chapter 2*, the synthesis of Calix[4]resorcinarenes is based on acid-catalyzed cyclo-condensation reactions. Thus, **Fig. 3.1** displays the production methodology of resorcinarene derivatives, by using resorcinol and various aldehydes as starting reagents.

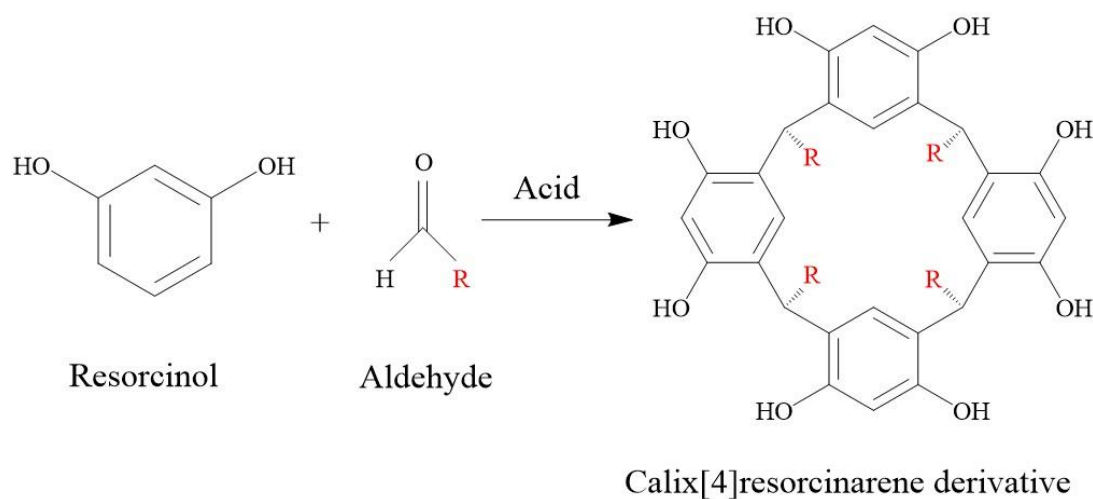


Fig. 3.1: Common synthetic route of calix[4]resorcinarene derivatives.

The employed ionophores in the thesis work were synthesized in the lab of *Prof. Telegdi Judit*. *C-dec-9-enylcalix[4]resorcinarene* (**I₁**) and *C-undecylcalix[4]resorcinarene* (**I₂**) (**Fig. 3.2**) were produced according to *Aoyama et al.* [149,150] by dissolving resorcinol (0.23 mmol, 0.025 g) and 0.23 mmol of aldehyde (*undec-10-enal* for **I₁** and *dodecanal* for **I₂**) into absolute ethanol (240 mL). The solution was cooled down to 0°C, and 37 mL of concentrated HCl was added, after an hour of stirring, the solution was heated and refluxed for twelve hours. The recrystallization via methanol and a (1:1) mixture of acetone: hexane, gave **I₁** as a yellowish-orange solid (Yield: 49 %, m.p.:277°C), and **I₂** as a beige solid (Yield: 48.8%, m.p.: 294°C).

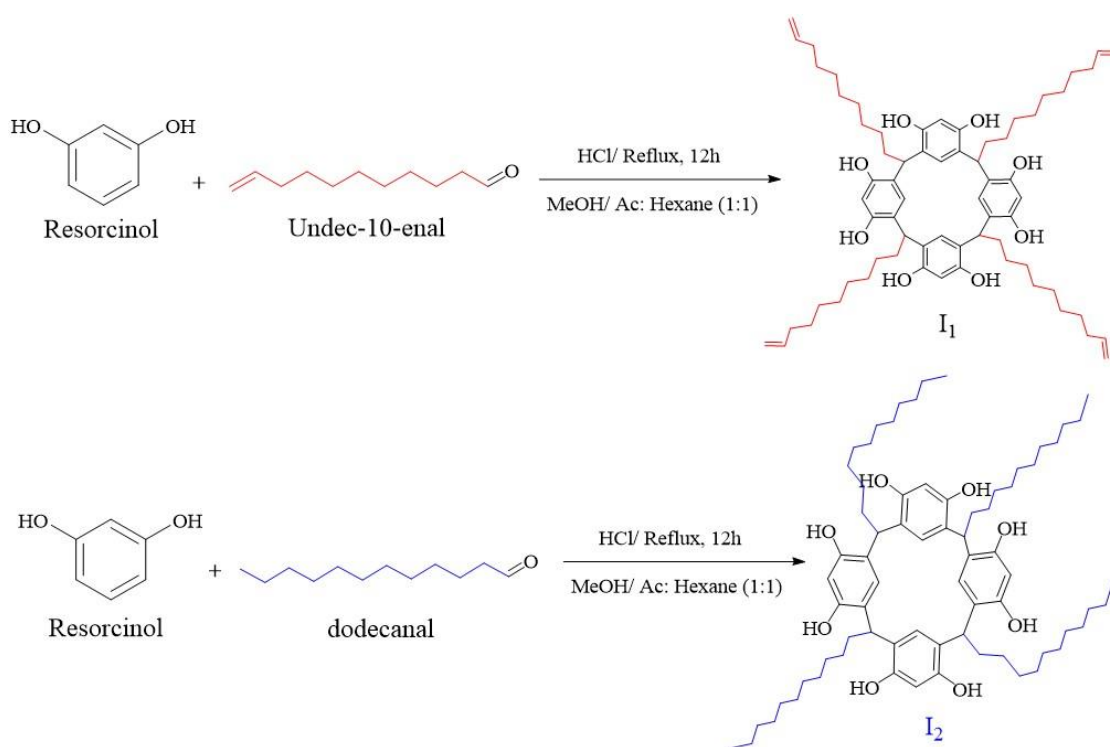


Fig. 3.2: Synthetic approach for ionophores **I₁** and **I₂**.

Two novel enantiomeric compounds bearing chiral moieties (**Fig. 3.3**), namely: *C-dec-9-enylcalix[4]resorcinarene-O-(S-)- α -methylbenzylamine* (**I₃**), and *C-dec-9-enylcalix[4]resorcinarene-O-(R+)- α -methylbenzylamine* (**I₄**) were produced by dissolving 50 mmol of *C-dec-9-enylcalix[4]resorcinarene* (**I₁**) in a (1:1) mixture of methanol-THF. Then, 50 mmol of paraformaldehyde and 25 mmol of either (*S*-)- α -methylbenzylamine (to get **I₃**) or (*R*+)- α -methylbenzylamine (to get **I₄**) was added. The resulting solutions were stirred for an hour under argon atmosphere, then refluxed for a half day time (12h), and the solvents were removed using a rotary evaporator. The recrystallization of the obtained precipitates was

performed twice though acetonitrile, giving compounds **I**₃ and **I**₄ as yellowish-orange solids (Yield: 50%, m.p: 70-72°C).

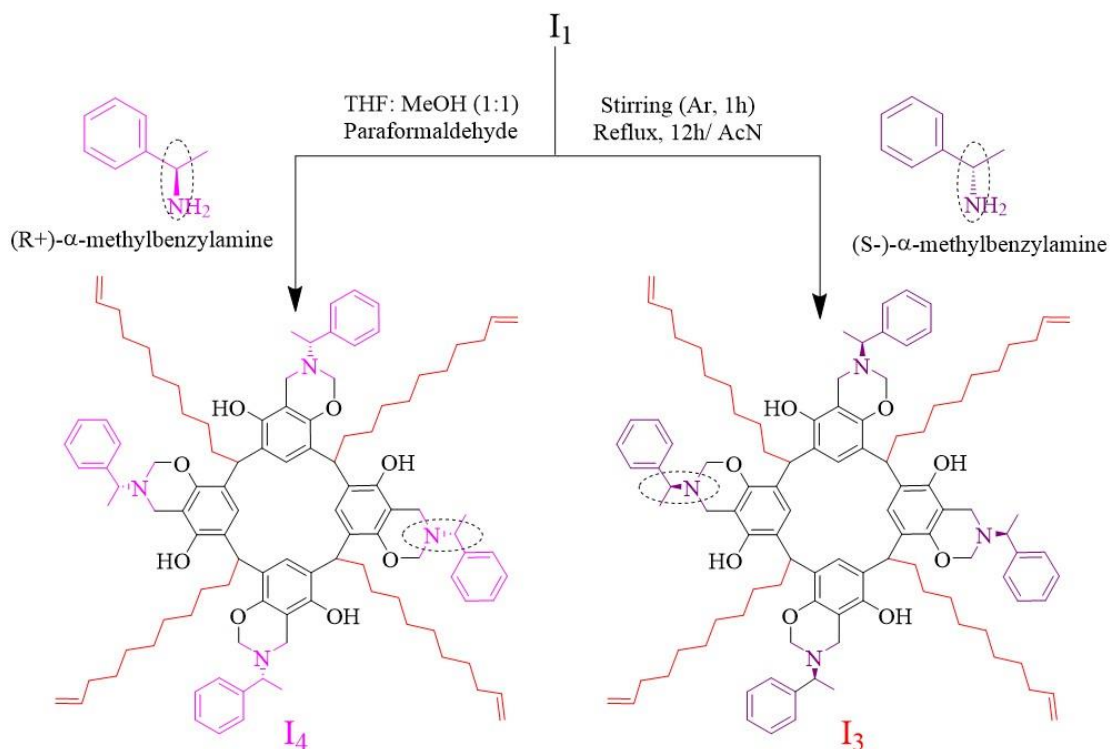


Fig. 3.3: Synthetic procedure for compounds **I**₃ and **I**₄.

Additional ionophores were synthesized, viz. *C-nonylcalix[4]resorcinarene* and *C-trans-2, cis-6-octa-1,5-dienylcalix[4]resorcinarene*, whereas *4-tert-butylcalix[4]arene* was purchased from Sigma-Aldrich. Due to their poor solubility in the majority of organic solvents, they weren't applied in further studies.

3.3 Ionophores analytical characterization methods

3.3.1 Attenuated Total Reflectance-Fourier Transform Infra-Red spectroscopy (ATR-FTIR)

To determine the ionophores' characteristic functional groups, for concluding their possible chemical structures, ATR-FTIR experiments were carried out on a Varian 2000 FTIR spectrometer (Scimitar Series, Varian Inc., US), the apparatus is equipped with a Mercury–Cadmium–Telluride (MCT) detector, and an ATR single reflection diamond unit (Specac Ltd, UK). The spectra were collected indoors of the middle infrared spectral range (4000–400 cm^{-1}), with a resolution of 4 cm^{-1} . For each spectrum, 64 individual scans were averaged, and all spectra were corrected by the data acquisition software (Varian ResPro 4.0) [137].

3.3.2 Nuclear Magnetic Resonance (NMR) spectroscopy

The molecular arrangement analysis is granted by the NMR technique, allowing the complete structure determination by providing aromatic and aliphatic chemical shifts. Complementing infrared profiles of the ionophores. NMR investigations were performed on Varian VNMR SYSTEM® spectrometers, using an indirect detection triple resonance $^1\text{H} \{^{13}\text{C}, \text{X}\}$ Z-gradient probe. The spectra were acquired at 600 MHz (400 MHz) in DMSO- d_6 at 25 °C (40 °C, 50 °C), with referencing both the carbon and the proton chemical shifts to the residual solvent signals ($\delta_{1\text{H}} = 2.50$ ppm, $\delta_{13\text{C}} = 39.5$ ppm). For enantiomeric compounds, the conditions were: (CDCl_3 , 400 MHz, 25 °C, residual solvent signals: $\delta_{1\text{H}} = 7.26$ ppm, $\delta_{13\text{C}} = 77.16$ ppm) [137].

3.3.3 Thermogravimetry-Differential Scanning Calorimetry-Mass Spectrometry (TG-DSC-MS)

Using thermal analyses, we aimed to study the behavior of the ionophores subjected to temperature variations under a controlled environment, for purity and thermal stability investigations, besides calorimetric melting points determination. A further aspect is to examine via mass spectrometry, the nature of released volatile products. Correspondingly, real-time coupled thermal analyses (TG-DSC) were accomplished via a Setaram Labsys Evo thermal analyzer, these analyses were carried out by placing sample amounts of 7 to 8 mg into 100 μL (Aluminium crucibles) in the following conditions: (Atmosphere: Helium (6.0), flow rate: 90 $\text{mL}\cdot\text{min}^{-1}$, heating rate: 20°C $\cdot\text{min}^{-1}$, temperature range: 20-500 °C). The output data were evaluated and corrected using the Calisto Processing, ver. 1.492 (Thermoanalyzer's processing software) [137].

To evaluate the decomposition products, the Evolved Gas Analysis through Mass Spectrometry (EGA-MS), were carried out on a Pfeiffer Vacuum OmniStar™ Gas Analysis System. For EGA-MS investigations, the mass spectrometer was operating in Electron Impact Mode (EIC) with a scan speed of 20 $\text{ms}\cdot\text{amu}^{-1}$ in the mass interval of 10-111 amu, and the spectra were collected in the SEM Bar Graph Cycles Acquisition Mode: Recording of the Total Ion Current (TIC), the Separate Ion Current (SIC), and the correspondent bar graph spectra for 101 masses. The transfer lines and gas splitters to the spectrometer were thermostated to 230 °C [137].

3.3.4 X-Ray Powder Diffraction (XRD)

To extract information on the crystalline structure of evaluated ionophores, the XRD technique was employed. The ionophores' diffractograms were recorded through the (1810/3710) Philips powder diffractometer assisted with a Bragg–Brentano para-focusing geometry using a CuK α monochromatic radiation ($\lambda = 0.154056$ nm). Suitable ground amounts of ionophores were positioned in the sample holder under pressure and then put inside the diffractometer chamber.

The data were collected at room temperature in reflection mode, with an exposure time of 1.00 s at each point, and a step of 0.04° in the 2θ range of $3-77^\circ$ [137].

3.3.5 Polarimetry

One extensively used technique for enantiomeric discrimination is the *polarimetry* method. It's based on measuring the polarized light deviation passing through a solution containing chiral compounds (Optically active). While studying enantiomers, their physical and chemical properties are identical, but polarized light is differently affected by them; the rotation amount (Specific rotation) tend to be similar but in opposite directions, the specific rotation $[\alpha]_D$, is generally calculated using the expression: $[\alpha]_D = (100 \times \alpha)/(l \times c)$, where 'c' stands for the solution's concentration in (g/100 ml) 'α' is the detected rotation, 'l' is the optical path length (dm), and 'D' is the light wavelength (nm). The optical rotation activities were performed on a JascoP-2000 Polarimeter. The products were dissolved in chloroform with a 0.1 g/100 ml in a 1 dm polarimeter tube at room temperature. A Sodium 'D line' was used (589.3 nm) [137].

The specific optical rotation ($[\alpha]_D$) values for "I₃" and "I₄" are -185.9° , and $+185.0^\circ$, respectively. The obtained values are almost similar and in the opposite sign, evidencing that compounds 'I₃' and 'I₄' are enantiomeric compounds.

3.4 Interfacial interactions based on Langmuir films: Surface Pressure-Area (Π-A) isotherms

Intended for examining the complexing abilities of the ionophores towards the set of studied cations, methods as pressure-area isotherms seem to be powerful tools, giving insights on the possible molecular interactions taking place at the water/air interface between the ultra-thin monolayers and water subphases modified upon adding heavy metals. Aiming to produce stable Langmuir ultra-thin films and surface pressure-area isotherms, a rectangular Langmuir-Blodgett trough was used (Model 611, NIMA Technology Ltd. Coventry, England), **Fig. 3.4**, with dimensions of 30 cm length, 20 cm width, and 0.5 cm depth, as well, it is equipped with a sensing filter paper of 20 mm length '*Wilhelmy surface pressure sensor*' [138].

Milli-Q deionized water was used as a blank subphase, later modified by different heavy metals (Cd^{2+} , Pb^{2+} , Cu^{2+} , and Hg^{2+}) of various concentrations (specific amounts of their salts were mixed carefully with Milli-Q water to get several subphases). The resulting solutions ($V \approx 0.5$ L) were poured inside the Langmuir trough. Next, the monolayers of ionophores were prepared by uniformly spreading 20 μL of macrocyclic solutions (dissolved resorcinarenes in chloroform with a 1 mg. mL^{-1} concentration) onto the water/air interface using a Hamilton microsyringe, after 10 min for solvent evaporation, the barrier was closed to record the

isotherms with a $100 \text{ cm}^2 \cdot \text{min}^{-1}$ average compression speed. The trough was enclosed in a box and thermostated to $20 \pm 0.5^\circ\text{C}$ throughout all tests (A triplicate repetition to ensure the stability and reproducibility of the isotherms was performed) [138].

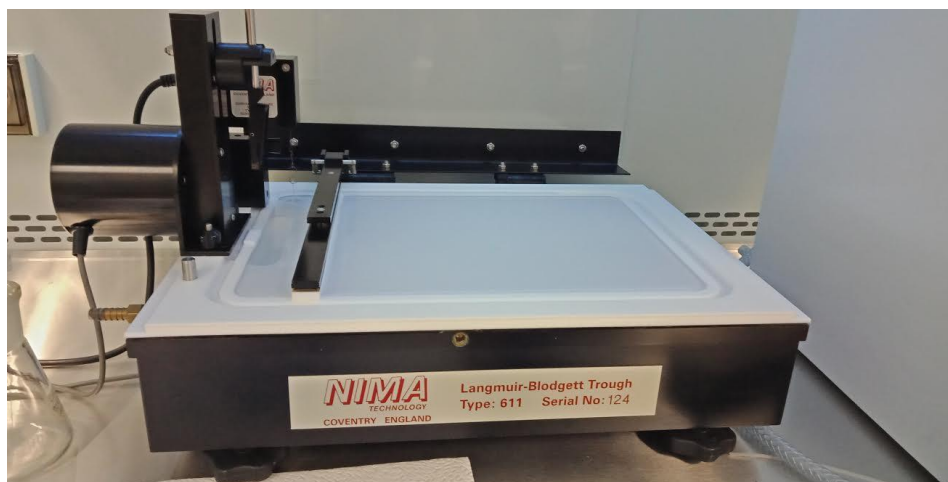


Fig. 3.4: Langmuir-Blodgett trough (Model 611, NIMA Technology Ltd.)

3.5 Heavy metals detection processes: Quartz Crystal Microbalance with Impedance measurement (QCM-I) and electrochemical tests

3.5.1. Electrode pretreatments

In order of having the best sensing performances, suitable cleaning procedures must be applied, to ensure surface purity before further modification. Rinsing and activation of gold electrodes were carried out ensuing a simple procedure:

- Quartz crystals (QCs) were cleaned via acetone for 10 min, followed by a washing with piranha solution ($1/3 \text{ H}_2\text{O}_2 + 2/3 \text{ H}_2\text{SO}_4$) or Hellmanex III solution for 10 min, and then, a rigorous rinsing with Milli-Q water, and let dry at room temperature inside a desiccator [53,65,67].
- For removing potential contaminants on the screen-printed electrodes (SPEs), cyclic voltammetry (CV) was used for electrochemical cleaning through applying 20 CV cycles at $100 \text{ mV} \cdot \text{s}^{-1}$ scan rate in $0.05 \text{ M H}_2\text{SO}_4$ solution in the potential range from -1.5 to $+0.5\text{V}$, [125,127]. The electrochemical cleaning presented stable voltammograms, and the cleaned SPEs were rinsed with Milli-Q water and placed inside a desiccator at room temperature until further employment.

3.5.2. Ionophores immobilization on the gold sensing area

The ionophores were dissolved in chloroform ($2 \text{ mg} \cdot \text{mL}^{-1}$). Through subsequent intensive drop-casting of various Calix-solutions on top of the clean gold electrode of quartz crystals

(10 μL) and screen-printed electrodes (2 μL), resorcinarenes sensors were fabricated. The modified electrodes were later dried at room temperature and kept inside a desiccator awaiting further use.

3.5.3 Quartz Crystal Microbalance with Impedance (QCM-I) experiments

The Quartz Crystal Microbalance (QCM) consists of two gold electrodes plated onto a thin disk of quartz (piezoelectric material), consequently, if a mass is adsorbed onto its surface, the gained change in oscillation frequency is proportional to the amount of adsorbed mass [53,67]. The QCM-D standing for QCM with Dissipation mode offers an advanced layer characterization parameter, the so-called ‘Dissipation’, using the ring-down method, the applied AC voltage in QCM-D is alternately switched off, and the measured current as a function of time is generally fitted to the frequency (f) and to the decay time constant (τ), consequently producing the dissipation (D), the QCM-D permits simultaneous measurements of frequency and dissipation parameters (f_n, D_n) [53] at different overtones (n).

Unlike typical QCM-D, the QCM-I, denoting QCM with Impedance analysis, applies a network analyzer to measure the complex impedance/conductance spectra of the QCM sensor, for both: odd overtones and fundamental frequencies. The impedance spectra are fitted by the measuring software to exactly determine the frequency (f_n) (Conductance maximum frequency), and the Full Width at Half Maximum (FWHM) parameters. Both f_n and FWHM can be associated with dissipation variations. Employing a network analyzer, impedance analysis allows nonstop measurements of resonance parameters, including the resonance curve, the resonance frequency, and the FWHM calculations, FWHM is proportional to the dissipation energy (Eq. (3.1)), where D is the dissipation and Q is the quality factor. The impedance analysis is performed at each test time for each overtone [138,139].

$$D = \frac{1}{Q} = \frac{FWHM}{f} \quad (3.1)$$

Evaluating the resorcinarenes’ sensing abilities towards heavy metals cations, coated crystals employing the ionophores as detection networks were immobilized, and real-time onsite label-free QCM-I detection experiments were performed utilizing the QCM-I.008 apparatus developed by *MicroVaccum Ltd* (**Fig. 3.5**). The device’s resonance sensitivity in liquid is 0.2 Hz, the dissipation sensitivity is 1×10^{-7} , and the mass sensitivity is $\leq 1 \text{ ng} \cdot \text{cm}^{-2}$. All sensing investigations were controlled utilizing the BioSense Software V.3.1. The employed crystals were AT-cut chips (Via cutting the quartz mineral at 35.25° orientation to the optical axis) and were purchased from *MicroVacuum Ltd*. They had a diameter of 14 mm and a 5 MHz

fundamental frequency, the quartz mineral was sandwiched between two gold electrodes, providing gold as a sensing area.



Fig. 3.5: QCM-I 008 unit setup (Courtesy of MicroVacuum Ltd).

The first step of a QCM-I analysis is the resonance frequency measurement based on the electrical conductance curve, the difference in frequency between coated and uncoated sensors is used for the loaded mass calculations using the Sauerbrey equation (Eq. (2.3)). In this step, the measurement's central parameters are the resonance frequency (f_{res}) and the bandwidth (FWHM), other parameters can be recorded (G_{off} , G_{max} , and B_{off}), apart from dissipation.

The water model solutions of 5, 25, 250, 500, and 1000 ppm were set by mixing convenient amounts of $(\text{Pb}(\text{NO}_3)_2)$, $(\text{Cd}(\text{NO}_3)_2)$, (HgCl_2) , $(\text{Cu}(\text{NO}_3)_2)$ salts with Milli-Q deionized water, and the QCM-I measurements were thermostated to 25°C. The flow cell volume was $\sim 40 \mu\text{L}$, and the flowrate was $200 \mu\text{L}\cdot\text{min}^{-1}$ using a peristaltic pump.

At first, we aimed to study the effect of heavy metals on bare crystals by injecting solutions of heavy metals through the QCM-I fluidic cell, containing bare crystals. Then, they were replaced by the resorcinarene sensors, aiming to study the heavy metals concentration effect on the newly developed modified electrodes.

As shown in **Fig. 3.6**, the solution of the heavy metals ions (1) flows through a peristaltic pump (2) into the flow cell (4) comprising the Calix-modified sensor (5) at the QCM-I instrument (3). By laterally vibrating the quartz crystal, the QCM-I generates the impedance/conductance spectra (6) employing a network analyzer (5). The data in the form of frequency, dissipation, and FWHM variations are calculated and processed by the software (7). Discharge waste container (8). The data were recorded for selected overtones $n = 1, 3, 5,$ and 7 representing 5, 15, 25, 35 MHz frequencies, correspondingly. The normalization frequency and FWHM

variations is conducted by dividing the change in the measured values by the overtone (n) number (Eq. (3.2)):

$$\Delta F = \frac{\Delta F_n}{n}, \quad \Delta FWHM = \frac{\Delta FWHM_n}{n} \quad (3.2)$$

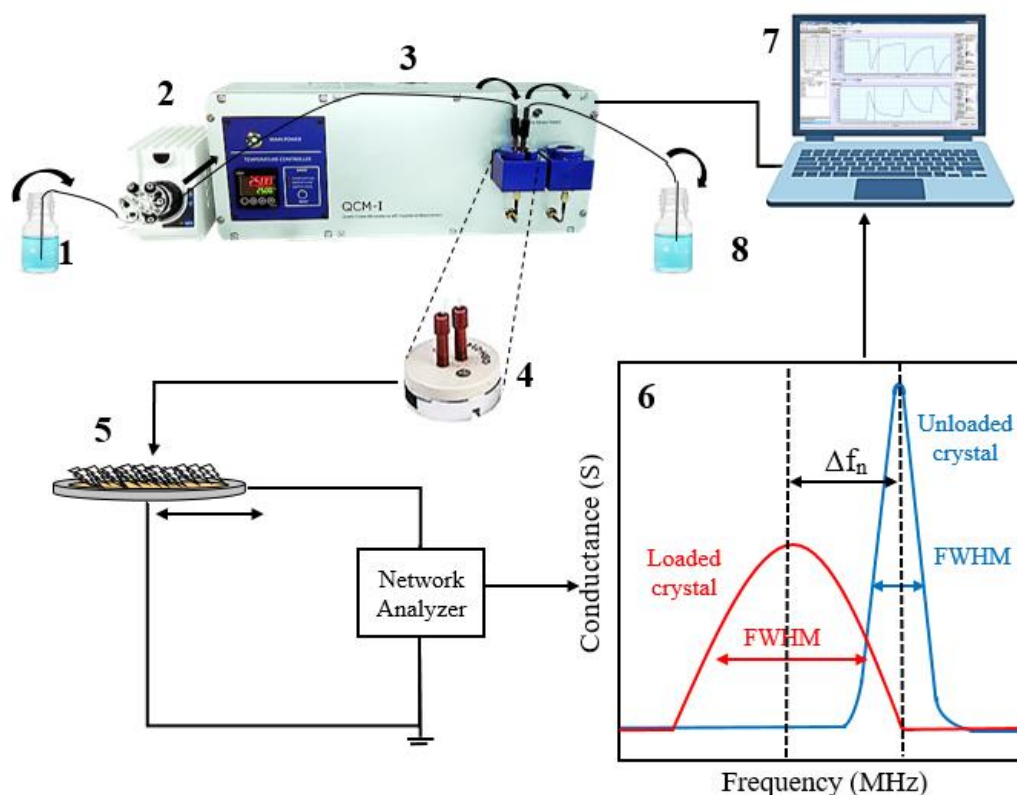


Fig. 3.6: Fluidic QCM-I setup and data assessment process.

3.5.4 Electrochemical detection experiments

Inspecting the ionophores' capabilities for the heavy metals detection, electrochemical studies were carried out employing cyclic voltammetry (CV), square wave voltammetry (SWV), and electrochemical impedance spectroscopy (EIS), to study the influence of the electrode modification on the electrode-solution interface properties, to perform the electrochemical characterization, and to investigate the sensing applications of the modified sensors. The voltammetry tests CV and SWV were performed on a Gamry interface 1010E potentiostat/galvanostat apparatus (**Fig. 3.7**) controlled by the Gamry inst. framework software, whereas the EIS experiments were carried out employing a Solartron 1250 frequency analyzer and a Solartron 1286 electrochemical interface (**Fig. 3.8**) controlled by the *ZPlot* software.

The electrodes (Equilibrium SAS, France) were composed of three electrodes printed system (2 mm OD gold working electrode, a U-shaped large gold counter electrode, and an Ag/AgCl reference electrode) connected to the potentiostat through a connector cable.

Fig. 3.7:

Gamry Interface
1010E potentiostat
and the employed
electrochemical cell



Fig. 3.8:

Solartron 1250
frequency analyzer
and Solartron 1286
electrochemical
interface



3.5.4.1 Screen-printed electrode (SPE) characterization

Before each EIS, CV, and SWV characterization measurements, the SPE was immersed into the cell containing 0.2 M HCl and the target metal ions which were stirred for 3 min to accumulate the metal ions at open circuit potential. The electrochemical characterization of the bare/modified electrodes in the absence/presence of 1ppm of heavy metals dissolved in 0.2 M HCl solution was completed (**Fig. 3.9**) employing the following conditions [125,127]:

- *Electrochemical impedance spectroscopy* was performed at the open circuit potential (OCP), by applying a 10 mV *ac* amplitude sine wave signal in the frequency range from 65 kHz to 1 Hz;
- *Cyclic voltammetry*: Forward and back potential scans were applied in the potential range from - 0.75 V to + 0.5 V at a scan rate = 0.05 V.s⁻¹.
- *Square wave voltammetry*: Frequency of 15 Hz, deposition time of 60 s, deposition potential of -1V within the potential window from -1 to +0.5 V.

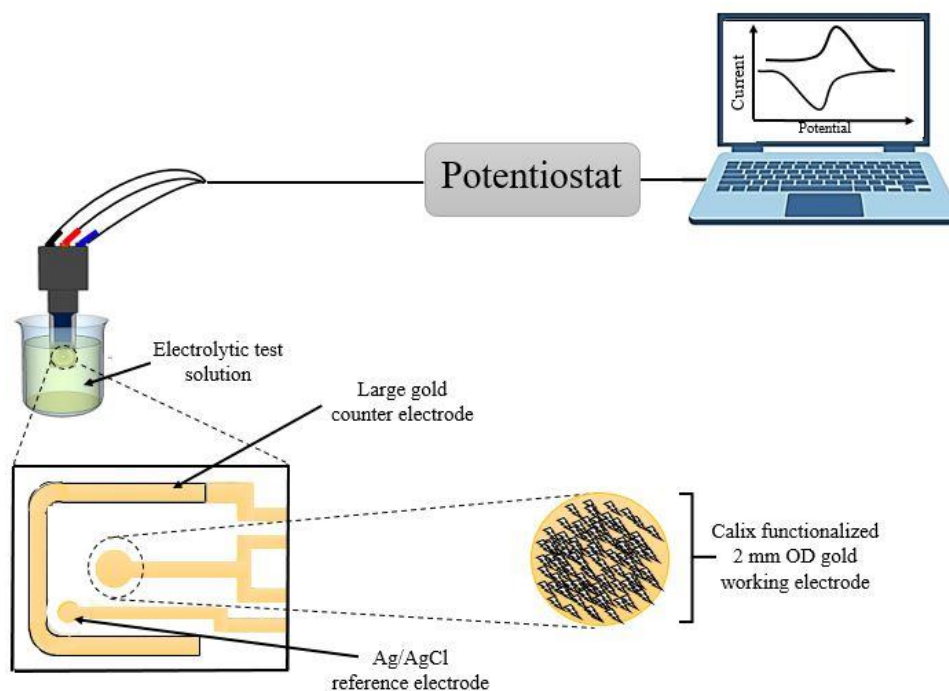


Fig. 3.9: Electrochemical detection setup and data assessment process

3.5.4.2 Experimental parameters optimization

Aiming to enhance the detection capacities of the prepared sensors towards various heavy metals, the physicochemical parameters having a direct influence on the square wave voltammetry (SWV) signals were optimized, namely: supporting electrolyte, pH, accumulation potential, and accumulation time [125,127].

3.5.4.2.1 Effect of supporting electrolyte

The influence of various supporting electrolytes was examined in order of choosing the most suitable one for offering the highest detection magnitude. The square wave voltammetry (SWV) conditions were similar to those employed in the electrochemical characterization part. The employed electrolytes are hydrochloric acid HCl 0.2 M ($pH_i = 0.7$), potassium chloride KCl 0.2 M ($pH_i = 6.8$), and acetate buffer ACB 0.2 M ($pH_i = 5.3$), which was prepared by mixing 15.4 g of ammonium acetate and 2.06 mL of glacial acetic acid in 990 mL of distilled water.

3.5.4.2.2 Effect of pH

The electrolytic medium's pH is highly affecting the interactions between the sensing platform and the target ions. Therefore, the detection response in 0.2 M HCl has been investigated by changing the pH values from 0.7 to 8. The pH was adjusted by a 0.1 M sodium hydroxide solution NaOH ($pH_i = 13$) and was monitored by the ADWA AD8000 digital pH meter. The conditions were similar to those employed in the electrochemical characterization part.

3.5.4.2.3 Effect of accumulation time and potential

The accumulation time and potential effects of the heavy metals on the sensing platforms have been studied within the timeframe from the 30 s to 180 s and within potential values ranging from -2V to -1V. The purpose was to optimize both effects to produce higher signals and so decent detection performance.

3.5.4.3 Calibration studies

The detection capability of the sensors towards various heavy metals with concentrations ranging from 1 to 100 ppb was examined under optimized conditions, and so for determining the statistical detection characteristics (linear ranges, detection, and quantification limits).

3.5.4.4 Interference studies

Aimed at evaluating the effect of interfering ions on the heavy metals detection and selectivity, the applicability of the proposed sensors was tested upon adding metal ions such as Al^{3+} , K^+ , Mg^{2+} , Zn^{2+} , and Ni^{2+} , usually present in water sources. Interfering ions of 4 ppm (40 folds compared to target ions) were added to 0.2 M HCl containing 100 ppb of heavy metals (Pb^{2+} , Cd^{2+} , Cu^{2+} , Hg^{2+}), and detection studies were performed under optimized conditions.

3.5.4.5 Reproducibility and repeatability

The terms accuracy, stability, and precision are used in labeling the quality of an output signal:

- *Accuracy* is the extent to which a given measurement agrees with the definition of the quantity being measured.
- *Reproducibility* is the ability of a single input standard to produce the same output signal, without alteration, each time it is put into operation.
- *Stability* pronounces the amount something changes as a function of parameters such as time, temperature.
- *Precision* is the degree to which a given set of measurements of one sample agrees with the mean of the set.

For a sensor platform, reproducibility and repeatability are the factors labeling its performance against the target elements to be detected: To evaluate the *repeatability* of our modified sensors, each platform has been employed to detect 100 ppb of heavy metals under optimized conditions by running three successive measurements. Hence, for assessing the *reproducibility*, three different electrodes have been modified by the same macrocyclic element and used to detect 100 ppb of heavy metals under optimized conditions. The relative standard deviation (RSD) was calculated to evaluate these parameters [125,127].

C

Chapter 4: Experimental results

4.1 Introduction

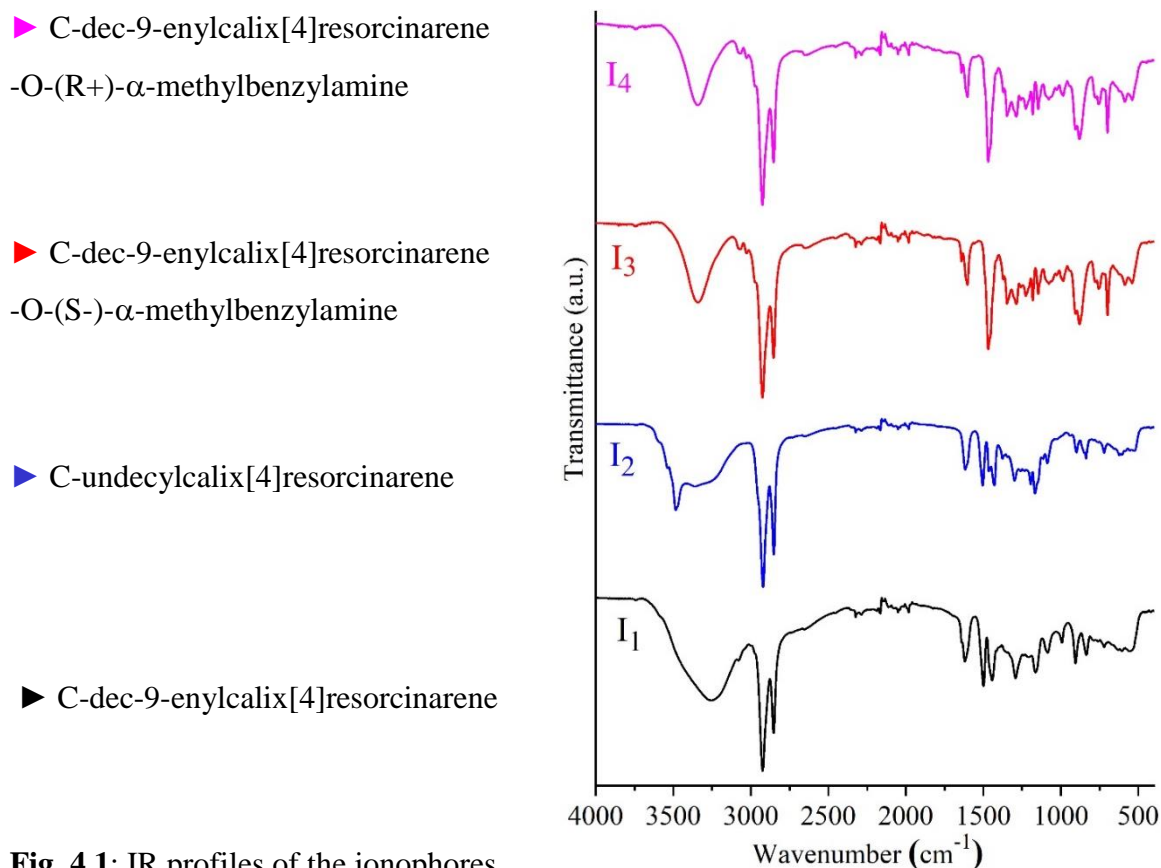
Aiming at developing sensitive and selective chemosensors for heavy metals detection, we undertook the production of recognition ionophores based on macrocyclic organic molecules, the choice fell on calix[4]resorcinarene derivatives on account of their reputation in electroanalytical applications [151–153]. The characterization of the synthesized ligands is provided in the first section of this chapter. Next, the evaluation of their encapsulation and complexation properties towards a set of cations (Hg^{2+} , Pb^{2+} , Cd^{2+} , and Cu^{2+}) is appraised using the Langmuir isotherms, while the detection application is deliberated in the last section of this chapter.

4.2 Ionophores' characterization results

4.2.1 Attenuated Total Reflectance-Fourier Transform Infrared spectroscopy (ATR-FTIR)

A first step towards the structural characterization of various synthesized ligands is the infrared spectral analysis, because of its capability in determining the major functional groups of a molecule. The infrared profiles for ionophores (I₁-I₄) are displayed in **Fig. 4.1**. By inspecting **Fig. 4.1**, all ionophores showed a large strong band at 3253 cm^{-1} (I₁), 3484 cm^{-1} (I₂), and 3340 cm^{-1} (I₃, I₄), corresponding to the *associated hydroxyl groups' (O-H) stretching vibration*. The physically absorbed water or molecular free OH groups can lead to this vibration as well; Nevertheless, the *associated resorcinolic (O-H) bond* is justified by dint of *the (C-O) stretching vibrations* (1164 cm^{-1} (I₁), 1195 cm^{-1} (I₂), 1226 cm^{-1} (I₃, I₄)), as well by the *in-plane deformations of (O-H) bonds* (1292 cm^{-1} (I₁), 1377 cm^{-1} (I₂), 1348 cm^{-1} (I₃, I₄)).

Major spectral dissimilarities are observed in the fingerprint region (2000-400 cm^{-1}), explained by the substituents diversity, e.g. various alkyl chains, cyclic ethers, and tertiary amines; the existence of all characteristic functional groups was apparent in this region. **Tables A.1-3 (Appendix. A)** contains detailed insights on various infrared assignments i.e. vibration frequencies and intensities.



4.2.2 Nuclear Magnetic Resonance (NMR) spectroscopy

Supporting the infrared analysis for (I₁-I₄), their ¹H NMR and ¹³C NMR spectra were recorded and are shown in **Fig. 4.2** and **Figs. B.1-3 (Appendix B)**, the NMR spectral profiling is offering chemical shifts of typical aliphatic and aromatic carbons and protons, accordingly confirming the proposed theoretical structures. Additionally, **Table B.1 (Appendix B)** summarizes the acquired assignments from the ionophores' spectra.

4.2.3 Thermogravimetry-Differential Scanning Calorimetry-Mass Spectrometry (TG-DSC-MS)

Besides the infrared and nuclear magnetic resonance profiling of ionophores (I₁-I₄), further investigations using thermal analyses were accomplished; aspiring to give insights on the thermal stability of (I₁-I₄), to define their calorimetric melting points (For comparison purpose with those determined directly), and to prove that the molecules are contaminant-free (pure), **Fig. 4.3** is displaying, therefore, the corresponding thermogravimetric (TG) and heat flow (DSC) curves. From **Fig. 4.3**, it is noticeable on the TG curves, that I₁ and I₂ had a small mass loss step (I₁ ~ 1.36%, I₂ ~ 1.1%) at lower temperatures (From 40 to 120°C). Though, the enantiomers I₃ and I₄ presented no mass loss at this heating level. Assessing the thermal

stability, I₂ showed the highest one, as from 120 to 300°C, this ionophore exhibited no mass loss; however, above the mentioned temperature, it starts to degrade rapidly. The outstanding thermal stability of I₂ is mainly due to its saturated carbon side chains, following this concept, I₁, I₃, and I₄ should be less stable thermally, because of the (C=C) unsaturation in the side chains' end of I₁, seemingly for enantiomers I₃ and I₄ plus their different substituents; which is the case, as the degradation of I₁ starts above 250 °C, and that of I₃ and I₄ starts above 180°C in a bi-step decomposition. Up to 500°C, the observed total mass losses are as follow: I₁ ~ 89.76%, I₂ ~ 86.94%, I₃ ~ 82.52% and I₄ ~ 82.38%.

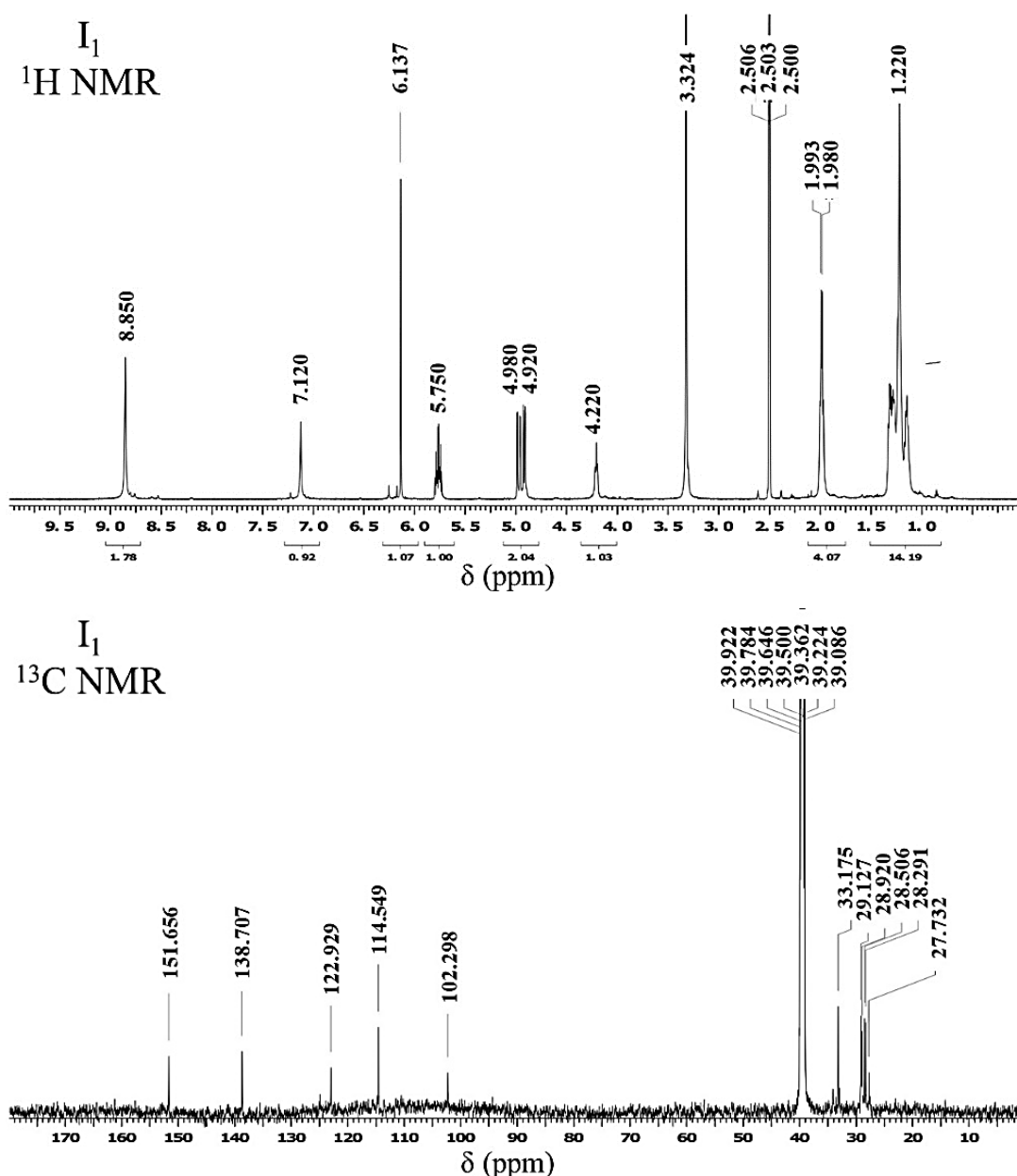


Fig. 4.2: Proton (¹H) and Carbon (¹³C) NMR spectra of ionophore (I₁) C-dec-9-enylcalix[4]resorcinarene.

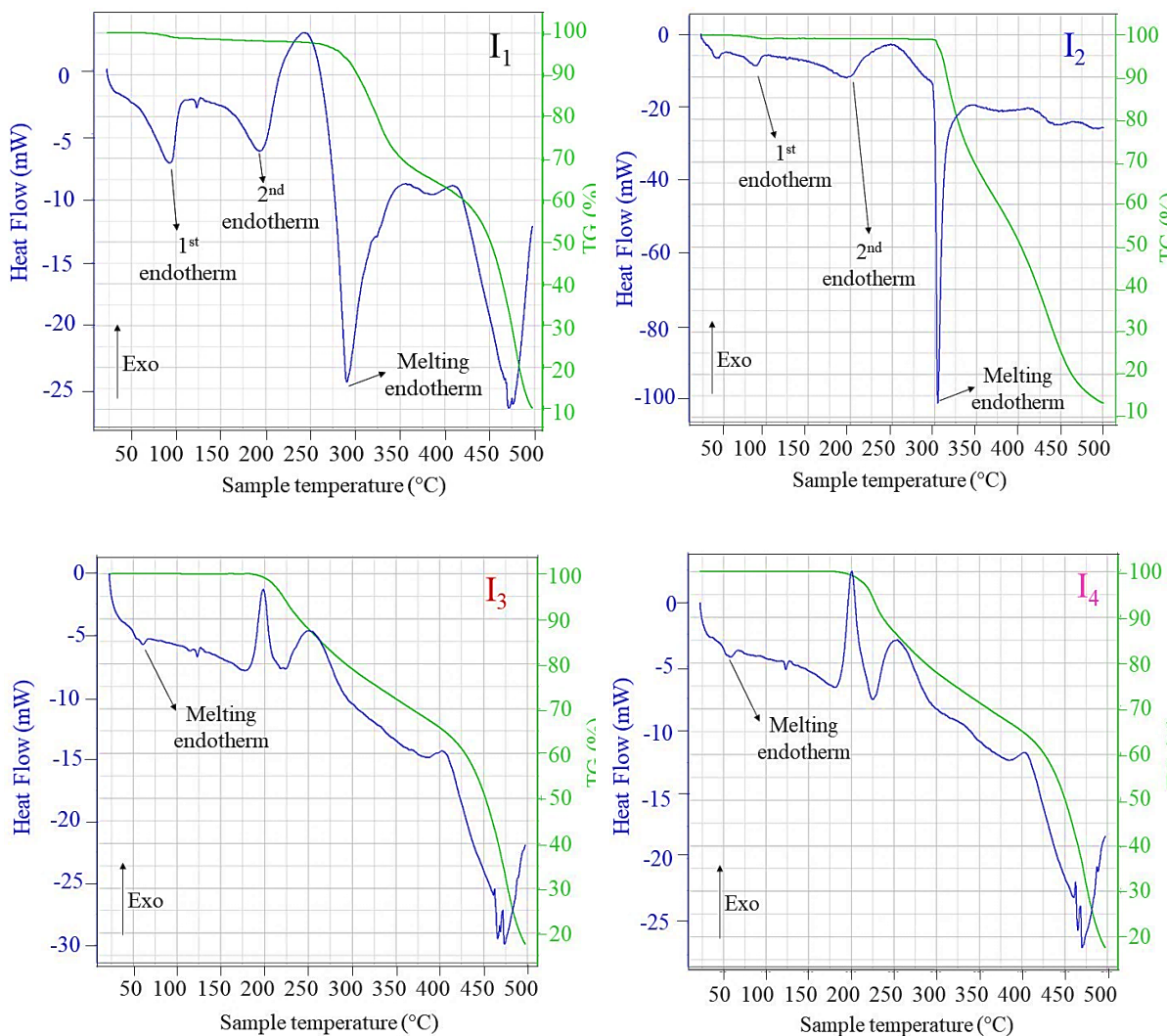


Fig. 4.3: TGA and DSC graphs for ionophores I₁-I₄

On the heat flow patterns of ionophores I₁ and I₂, small endotherms (~90°C) are seen, accompanied by small mass losses, these types of endotherms are owing to the evaporation of physically bound water or else solvents leftover from the synthesis process. A second endothermic peak was observed for I₁ (~194.1°C) and I₂ (~196.9°C), mostly caused by intermolecular changes in the resorcinarenes' common rings, since it was not accompanied by mass losses. A third endothermic transformation is observed for both I₁ (Onset temperature (T_0) = 269.5°C), peak maximum (T_m = 289.9°C)) and I₂ (Onset temperature (T_0) = 300.75°C), peak maximum (T_m = 304.23°C)), these peaks are corresponding to the calorimetric melting points of both ionophores, which are in good agreement with those determined directly (277°C for I₁ and 294°C for I₂). From the shapes of melting endotherms (A small broader peak for I₁ and a very intense sharp peak for I₂), one can recognize that I₁ is partly crystallized and I₂ is

crystallized. Not many endotherms were perceived in the case of enantiomers I_3 and I_4 , since from 50 °C up to 75 °C on their DSC curves, only one small broad endotherm is observed, corresponding to their melting: I_3 (Onset temperature ($T_0 = 48.6$ °C), peak maximum ($T_m = 61$ °C)), I_4 (Onset temp. ($T_0 = 49.22$ °C), peak maximum ($T_m = 60$ °C)), the stated calorimetric melting points are in decent agreement with the experimental ones (70-72 °C), and generally such shape of melting endotherms matches with a semi-crystallized compound. Though, thermal events detected after 180 °C, correspond to the enantiomers' degradation.

Aiming at evaluating the ionophores' purity, evolved gas analyses via mass spectrometry were carried out, the spectra were recorded at the point when the release of the evolved gases takes place at a higher rate, those spectra were determined via differential thermogravimetry patterns and corrected by transfer time from the thermogravimetric analyses to the mass spectrometer.

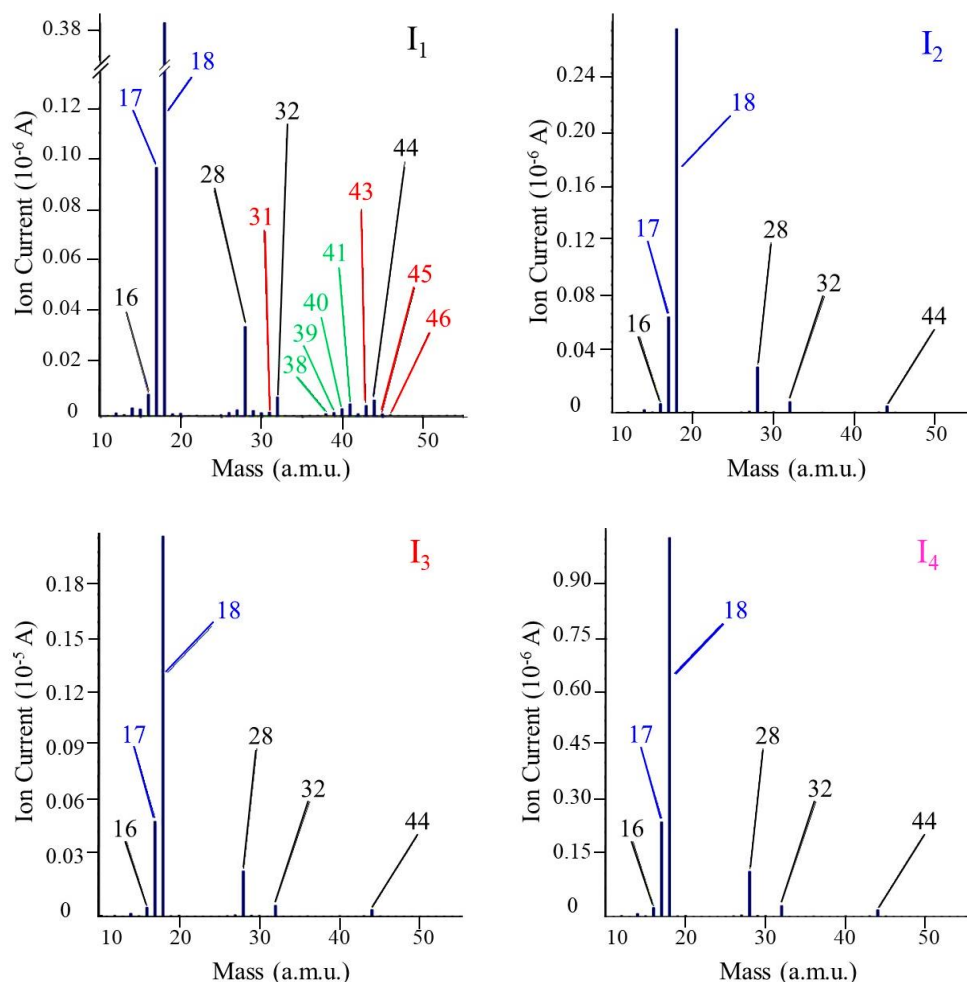


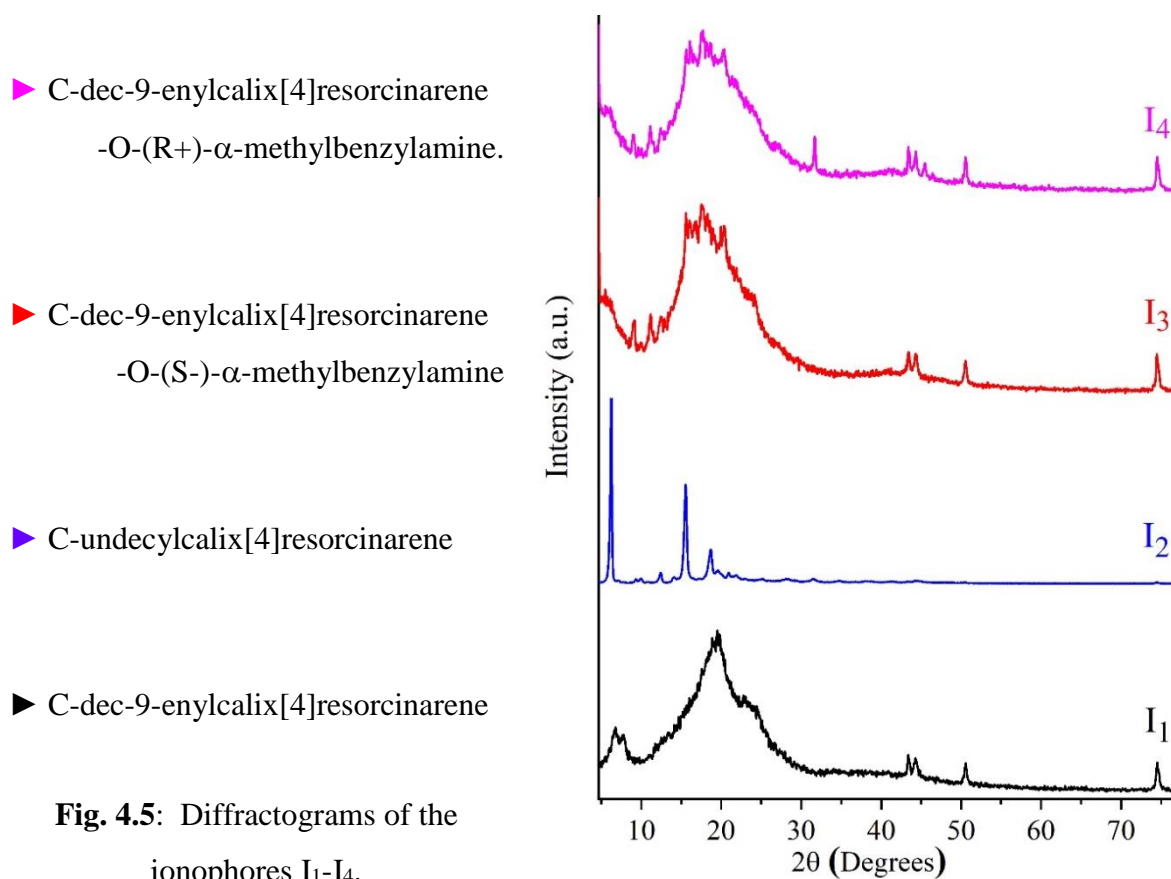
Fig. 4.4: Characteristic MS of evolved volatiles from ionophores I_1 - I_4 .

The mass spectra are displayed in **Fig. 4.4**, the analogous mass spectra of I_1 showed that the major component of the evolved gases is water (m/z : 18, 17), approving the physically bound water evaporation, peaks of residual air entrapped within transfer lines during the changing

samples' process were observed (m/z : 44 (CO_2), 32 (O_2), 28 (N_2) and 16 (O)), traces of ethanol (m/z : 46, 45, 43, 31) and acetonitrile (m/z : 41, 40, 39, 38) were also detected, and are mainly remaining from the synthesis and purification procedures. Considering I_2 , I_3 , and I_4 , peaks of residual air (m/z : 44 (CO_2), 32 (O_2), 28 (N_2), and 16 (O)) and water (m/z : 18, 17) were identified on their mass spectra. The results confirm the purity of the synthesized molecules.

4.2.4 X-Ray Powder Diffraction results

The XRPD was accomplished as a complementary characterization method to those debated above, to distinguish the ionophores' crystallinity degree and to compare it with the heat flow outcomes. The X-ray diffractograms are shown in **Fig. 4.5**, where, I_1 , I_3 , and I_4 are showing a semi-crystalline structure, whereas I_2 is presenting a crystalline behavior, which is correlating decently with the presented melting peaks in heat flow curves (Small broader endotherms for I_1 , I_3 , and I_4 and very intensive sharp endotherm at 300°C for I_2).



Due to the enantiomeric properties of I_3 and I_4 , which were revealed by their similar FTIR, P.XRD, and TG.DSC.MS results, besides presenting the same specific light deviation value in opposite signs (polarimetry), only I_3 will be used for further layer applications.

4.3 Heavy metals subphases/Ionophores interfacial interactions

4.3.1 Introduction

The pertinence assessment of the proposed ionophores should be appraised; before any potential sensing or detection application towards the metals ions in aqueous environments, the complexation properties of these ions and the ligands are of huge importance. Accordingly, preliminary studies, such as pressure-area isotherms, have shown interesting indications on the intermolecular interactions capable of occurring between the water-based subphases, and the ultra-thin monolayers on the water/air interface [154–159].

4.3.2 Surface pressure-area (Π -A) isotherms' results

Pointing at evaluating the influence of different heavy metals on the resorcinarenes-based Langmuir films, we recorded the variations of surface pressure Π (stated in mN/m) versus the molecular area (\AA^2). The outcomes exhibited good stability and reproducibility regarding the isotherms (each test was performed at least in triplicate). The surface pressure-area (Π -A) isothermal evolution of ionophores-based ultra-thin films I_1 , I_2 , I_3 against various heavy metals (Cd^{2+} , Cu^{2+} , Hg^{2+} , and Pb^{2+}) amounts are demonstrated.

4.3.2.1 Phase transition descriptions

4.3.2.1.1 Langmuir isotherms' results for ionophore I_1

The isotherms of C-dec-9-enylcalix[4]resorcinarene monolayers (I_1) using pure water and different heavy metals concentrations as aqueous subphases are shown in **Fig. 4.6**, whereas **Table C.1 (Appendix C)** is summarizing their Langmuir data. They mainly presented two phase transitions, manifesting in a first gas-liquid and a second liquid-liquid(quasi-solid) evolution. In the case of *cadmium ions* (**Fig. 4.6. a**), the isotherms underwent the 1st transition at ~ 107 , ~ 173 , ~ 167 , $\sim 194 \text{ \AA}^2/\text{Molecule}$ correspondingly for 0, 5, 25, 250 ppm, whereas the 2nd was observed at ~ 105 , $\sim 115 \text{ \AA}^2/\text{Molecule}$ for 25 and 250 ppm. The value of surface pressure increased without an obvious phase transition reaching the collapse pressure in the case of water and 5 ppm subphases. *Copper ions*-based subphase (**Fig. 4.6. b**) similarly went through the 1st transition at ~ 107 , ~ 169 , ~ 230 , $\sim 330 \text{ \AA}^2/\text{Molecule}$, and the 2nd transition at ~ 87 , ~ 91 , $\sim 160 \text{ \AA}^2/\text{Molecule}$ is noticeable for 5, 25, 250 ppm, considering the blank subphase, only the gas-liquid transition was gotten while increasing the pressure up to collapse ($A_c = 65 \text{ \AA}^2/\text{Molecule}$, $\Pi_c = 32 \text{ mN/m}$). In the case of *mercury subphases* (**Fig. 4.6.c**), the 1st phase transition is obtained at ~ 107 , ~ 225 , ~ 240 , $\sim 310 \text{ \AA}^2/\text{Molecule}$, and the 2nd phase transition is shown at ~ 130 , ~ 135 , $\sim 180 \text{ \AA}^2/\text{Molecule}$ for 5, 25, and 250 ppm, the pressure increased reaching collapse without further phase transitions in case of pure water. For *lead ions* (**Fig. 4.6.d**), the

1st transition was obtained at ~ 290 , ~ 360 $\text{\AA}^2/\text{Molecule}$, and the 2nd at ~ 147 , ~ 183 $\text{\AA}^2/\text{Molecule}$ for 25 and 250 ppm. Although, the 0 and 5 ppm isotherms showed only a gas-condensed liquid evolution at ~ 107 and 150 $\text{\AA}^2/\text{Molecule}$, respectively.

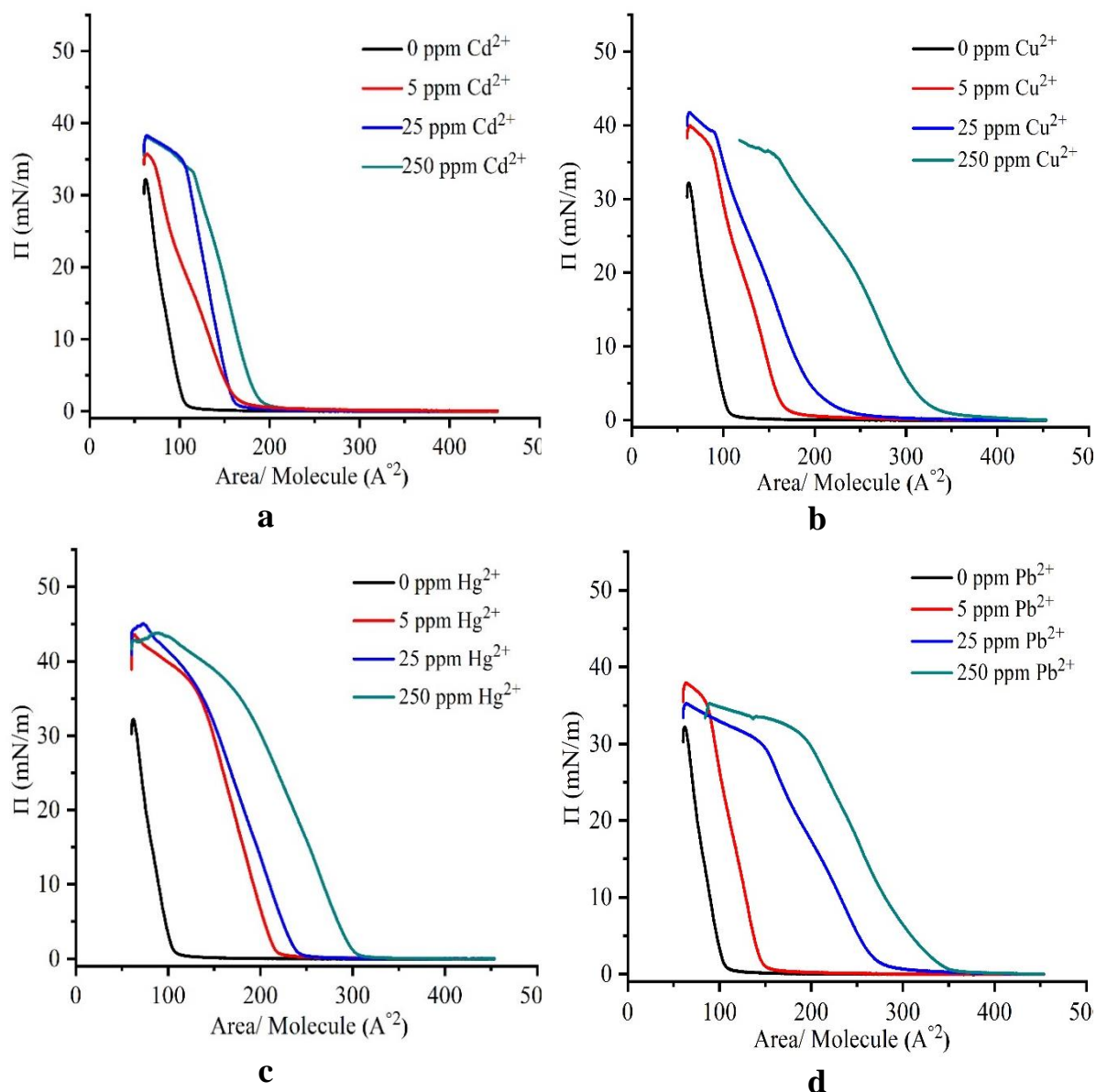


Fig. 4.6: Langmuir (Π -A) isotherms for ionophore I_1 at different concentrations.

4.3.2.1.2 Langmuir isotherms' results for ionophore I_2

The corresponding Langmuir isotherms formed by the C-undecylcalix[4]resorcinarene monolayers at the air/water interface are displayed in **Fig. 4.7**, moreover, their isothermal data are recapitulated in **Table C.2 (Appendix C)**. The isotherms of I_2 went through one phase transition (gas-liquid (condensed liquid)) for all heavy metals subphases, except the case of *cadmium cations* (**Fig. 4.7.a**), where two-phase evolutions were perceived, the 1st at ~ 135 , ~ 160 , ~ 230 , ~ 340 $\text{\AA}^2/\text{Molecule}$ for 0, 5, 25, 250 ppm, and the 2nd (liquid-liquid (quasi solid))

at ~ 135 , ~ 170 $\text{\AA}^2/\text{Molecule}$ for 25, 250 ppm. Nevertheless, for 0 and 5 ppm concentrations, the pressure reached the collapse without further transitions. The gas-liquid isothermal evolution was similarly detected at ~ 135 , ~ 190 , ~ 385 , ~ 475 $\text{\AA}^2/\text{Molecule}$ for 0, 5, 25, 250 ppm of *copper* (**Fig. 4.7.b**), at ~ 135 , ~ 230 , ~ 300 , ~ 330 $\text{\AA}^2/\text{Molecule}$ for 0, 5, 25, 250 ppm of *mercury* (**Fig. 4.7.c**), and ~ 135 , ~ 165 , ~ 190 ~ 315 $\text{\AA}^2/\text{Molecule}$ for 0, 5, 25, 250 ppm of *lead* (**Fig. 4.7.d**). A slight slope variation in the 250 ppm isotherm of Hg^{2+} ions at ~ 171 $\text{\AA}^2/\text{Molecule}$ was noticed; mainly attributed to some intermolecular changes rather than a liquid-liquid evolution, except that, all isotherms reached the collapse pressure without extra phase transitions.

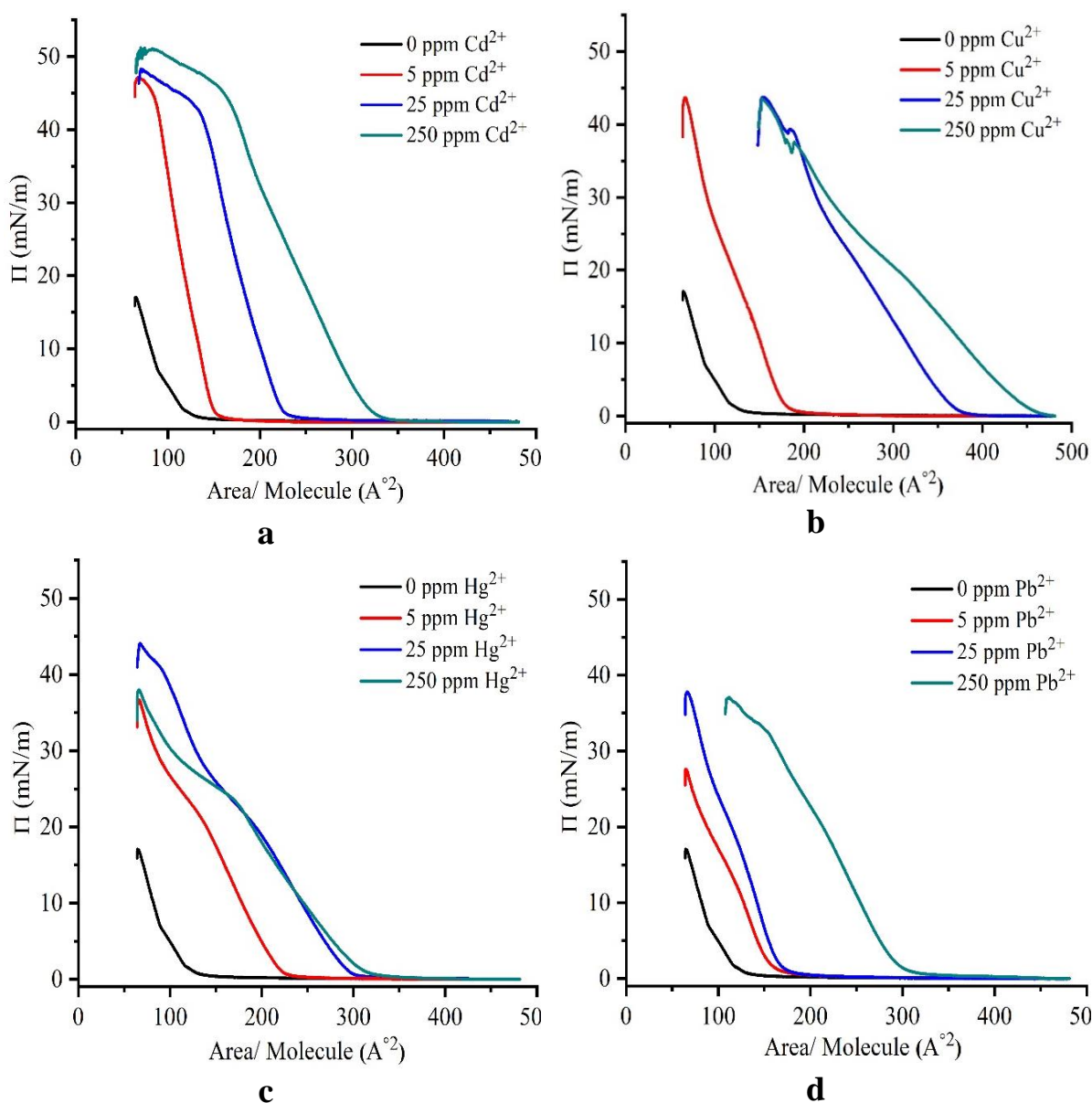


Fig. 4.7: Surface Pressure-Area isotherms for ionophore I_2 at different concentrations.

4.3.2.1.3 Langmuir isotherms' results for ionophores I_3

Fig. 4.8 presents the Langmuir isotherms of I_3 , while **Table C.3 (Appendix C)**, is giving insights into the isothermal data. The isotherms went through one transition interpreted by a gas-liquid (condensed liquid) phase evolution, excluding the case of *cadmium cations* when a second liquid-liquid transition was seen.

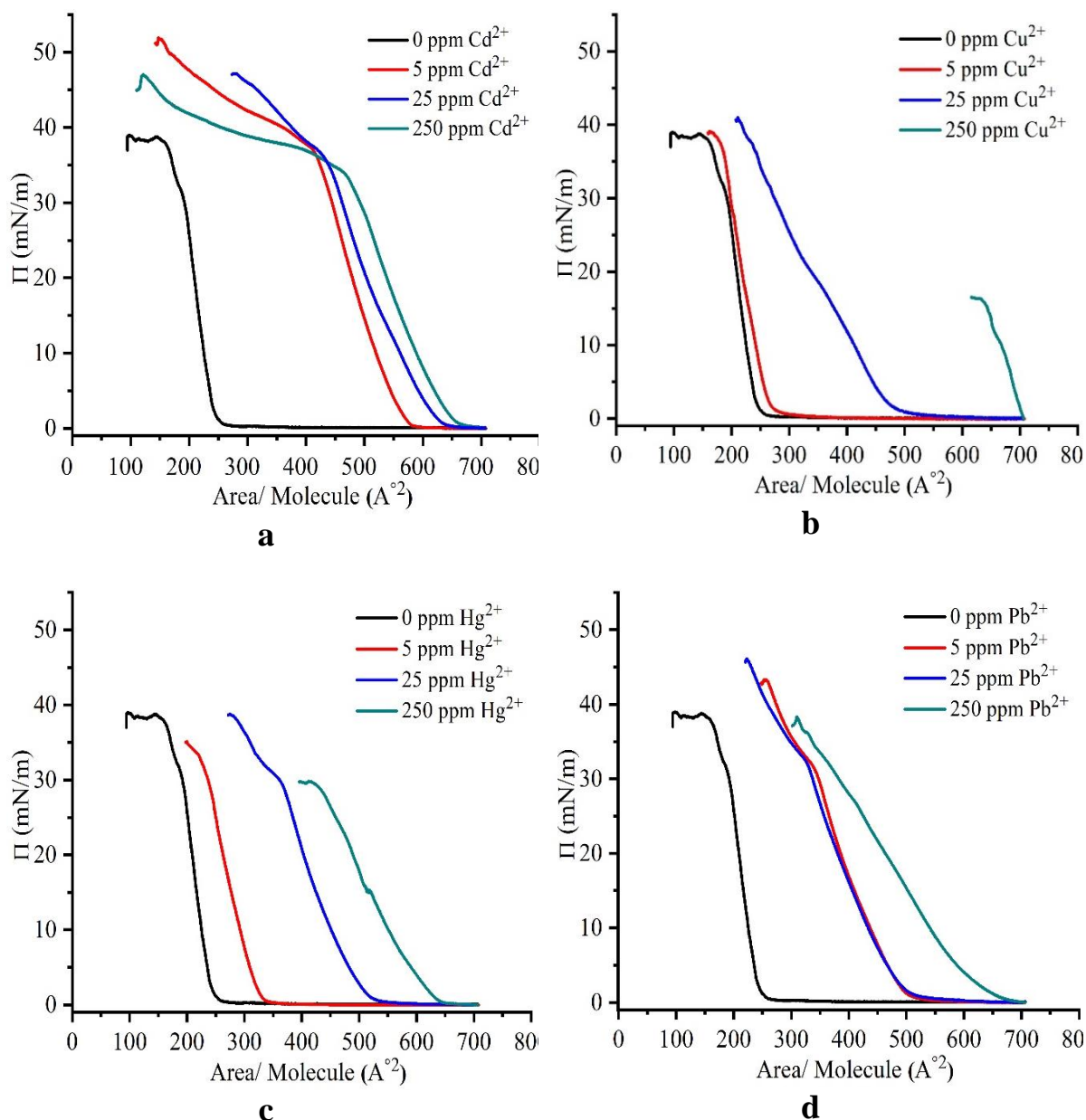


Fig. 4.8: Langmuir isotherms for ionophore I_3 at different concentrations.

Considering Cd^{2+} subphases, the 1st evolution was at ~ 255 , ~ 585 , ~ 640 , $\sim 665 \text{\AA}^2/\text{Molecule}$ (**Fig. 4.8.a**) for 0, 5, 25, 250 ppm. Although the 2nd evolution for the 5, 25, 250 ppm concentrations was at ~ 413 , ~ 440 , $\sim 465 \text{\AA}^2/\text{Molecule}$, no evident transitions were observed in the case of pure water subphase while increasing the pressure to collapse.

The gas-condensed liquid transition is observed in the case of *copper ions* at ~ 255 , ~ 275 , 505 , $\sim 710 \text{ \AA}^2/\text{Molecule}$ (**Fig. 4.8.b**) respectively for 0, 5, 25, 250 ppm. For *mercury subphases*, it's detected at ~ 255 , ~ 340 , ~ 540 , $\sim 645 \text{ \AA}^2/\text{Molecule}$ (**Fig. 4.8.c**) for 0, 5, 25, 250 ppm, correspondingly. For *lead cations*, it was gotten at ~ 255 , 500 , 515 , $\sim 680 \text{ \AA}^2/\text{Molecule}$ (**Fig. 4.8.d**) sequentially for pure water, 5, 25, 250 ppm. Notwithstanding the changes in the isotherms slopes which are mainly due to intermolecular changes, the pressure reached collapse while increasing the ions amounts in solution without obvious phase transitions in cases of Cu^{2+} , Hg^{2+} , and Pb^{2+} cations.

4.4 Results of Quartz Crystal Microbalance with Impedance measurements (QCM-I)

4.4.1 Introduction

This section gives insights on outcomes from static in-situ QCM-I measurements applied to detect heavy metals in water samples, firstly unmodified (Bare) quartz crystal resonators were used, and later, ionophores-modified QCM chemosensors were employed. The data in form of frequency, dissipation, and Full Width at Half Maximum (FWHM) variations, were collected from a newly commercialized instrument and were the subject of further evaluation. Herein, the introductory exploitation of this type of measurement showed its effectiveness in analytical applications for toxic metallic elements sensing.

4.4.2 Effect of heavy metals ions on the gold surface of quartz crystals

A first step towards the sensing application is to study the effect of the heavy metals ions on bare crystals upon adding rising amounts of ions (Cd^{2+} , Cu^{2+} , Hg^{2+} , and Pb^{2+}). For that reason, frequency (ΔF), dissipation (ΔD), and Full Width at Half Maximum (ΔFWHM) shifts were recorded on unmodified quartz crystals through in-situ QCM-I measurements, **Fig. 4.9** is displaying therefore those variations in function of time.

The quartz resonators' gold electrodes did not detect toxic metals, as no decrease in frequency (Mass loading on the crystal surface) was noted for all cases of study. A rigid character of the electrodes' surfaces was dominant, as no changes in dissipation energy were obvious ($\Delta D \sim 0$). However, some fluctuations were existing in the majority of plots, explained by the dry electrode's surface wetting due to straight exposure to aqueous solutions. The inability of bare gold surfaces to sense heavy metals proves that neither physical nor chemical modification or interaction has occurred, the later interactions are essential in increasing the quartz crystal's sensitivity, where taking advantage of detection networks is compulsory.

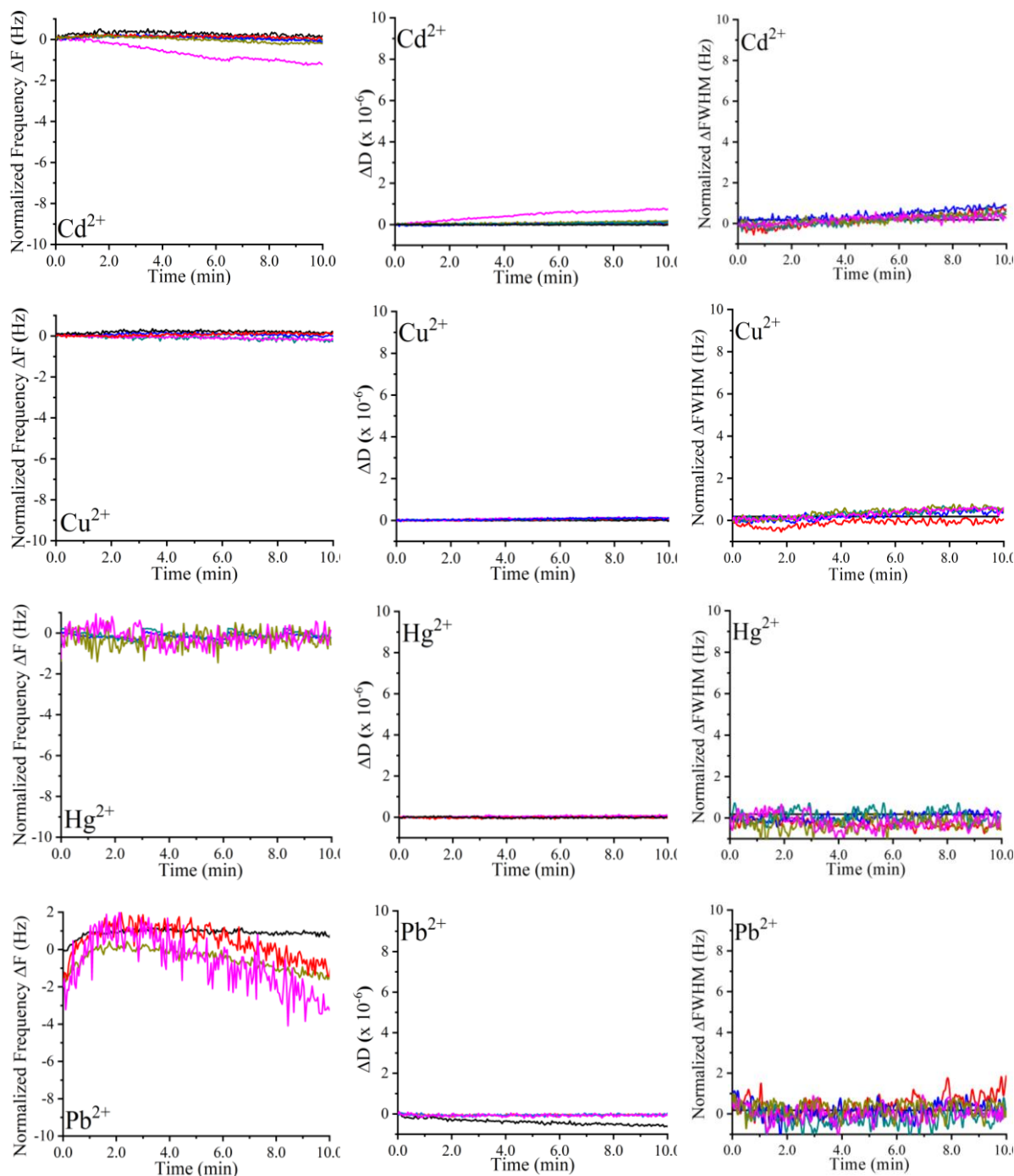


Fig. 4.9: Normalized frequency, dissipation, and FWHM shifts of unmodified crystal resonators against various ions amounts (— 0, — 5, — 25, — 250, — 500, and — 1000 ppm) in time

4.4.3 Heavy metals' concentration effect on resorcinarenes-piezogravimetric-sensors

Targeting water environmental monitoring via applied in-situ QCM-I analysis, drop-coated crystal gold electrodes using ionophores I₁, I₂, and I₃ as sensing-elements platforms were constructed, aiming at evaluating their heavy metals' detection capacities in model solutions modified via adding toxic metallic elements. Hence, **Figs. 4.10-12** are exposing the sensing

shifts (Normalized frequency: $\Delta F_n/n$, normalized dissipation: ΔD_n , and normalized full width at half maximum: $\Delta FWHM_n$) of Calix-chemosensors against increasing concentrations of ions in time, and **Tables D.1-3 (Appendix D)** are offering a summary of $\Delta F_n/n$, ΔD_n , and $\Delta FWHM_n$ values, collected at endpoints of the detection plots.

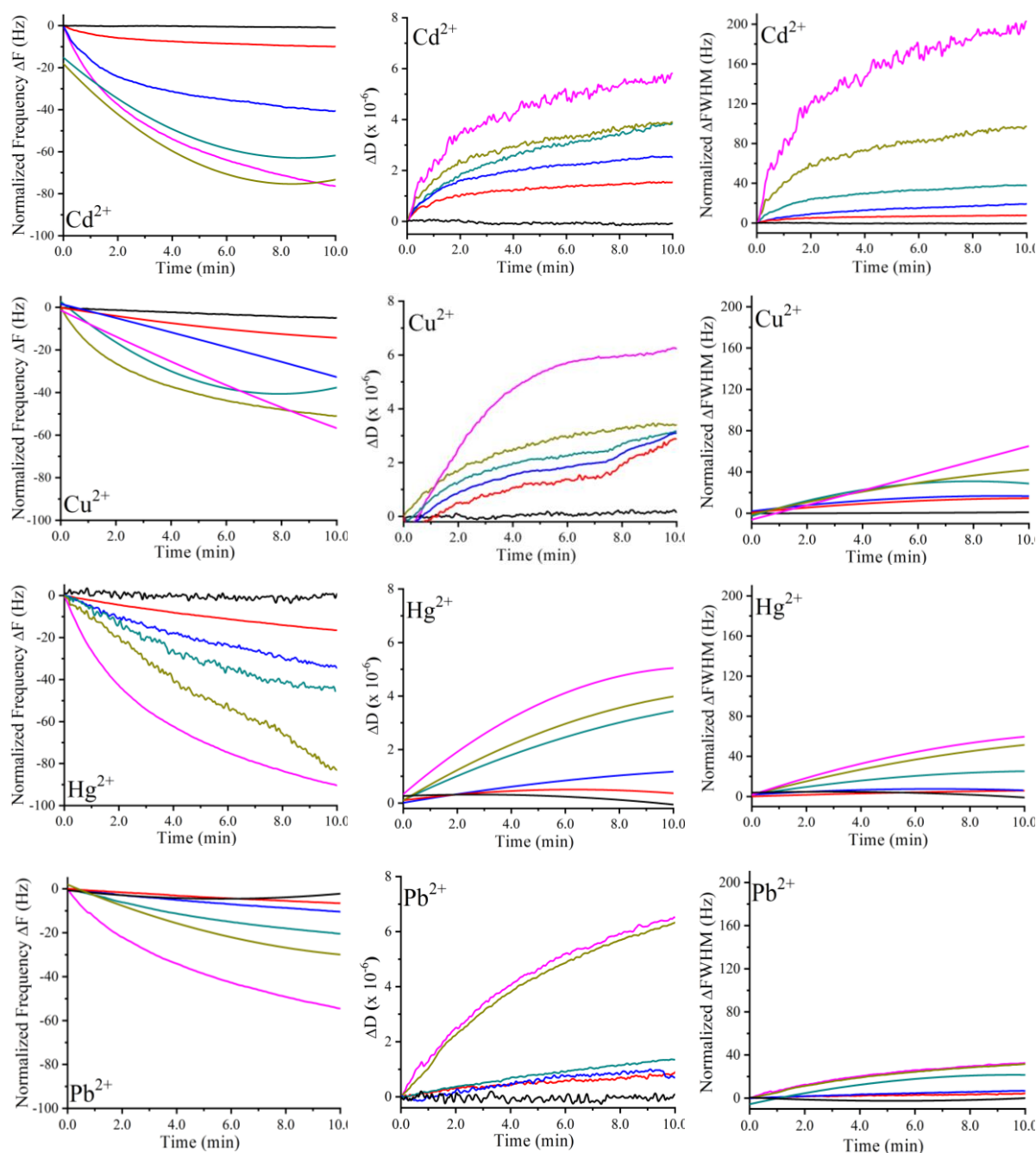


Fig. 4.10: Normalized frequency, dissipation, and FWHM shifts for ionophore I₁ based QCM sensor against various ions amounts (—0, —5, —25, —250, —500, and —1000 ppm) in time

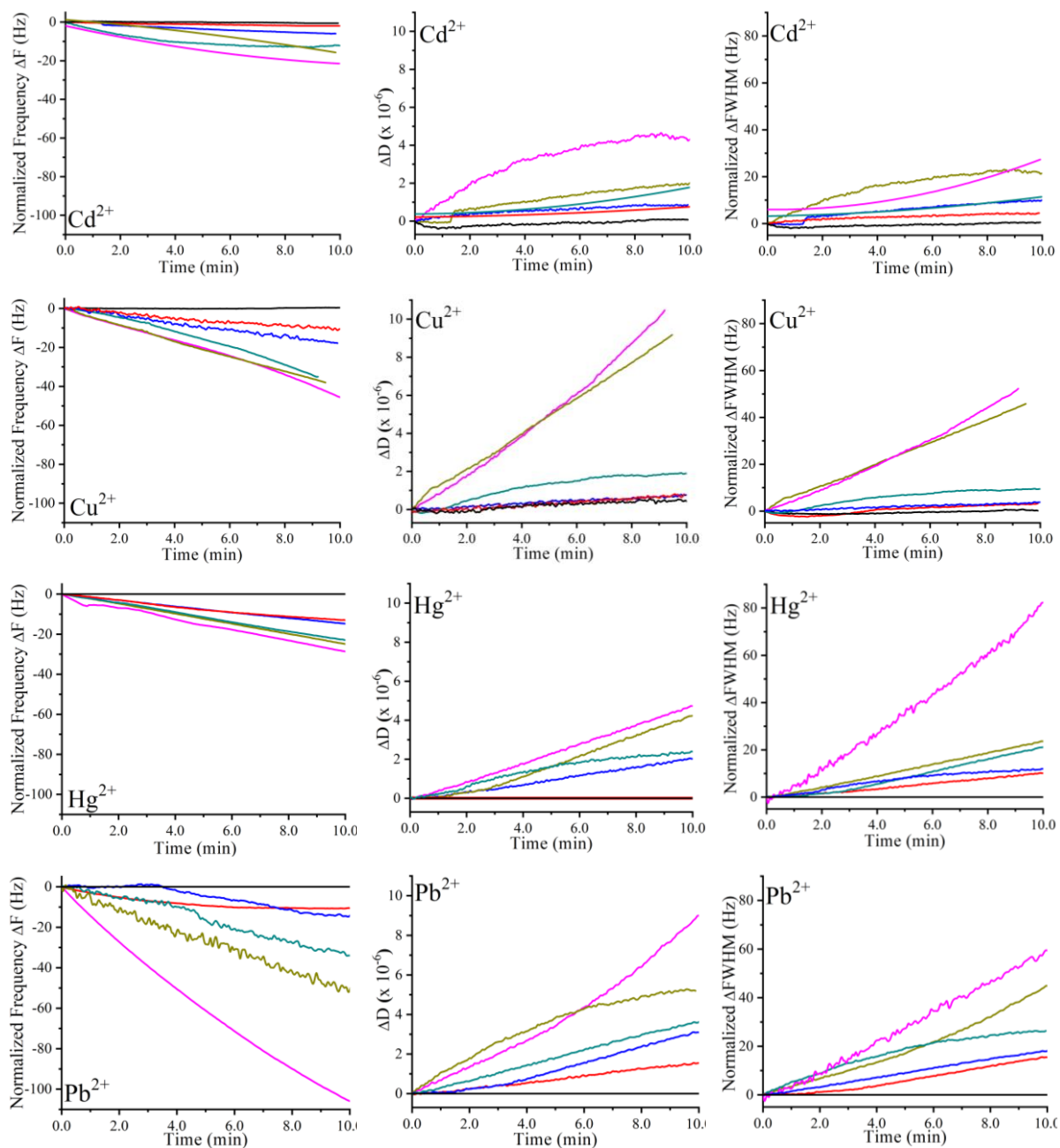


Fig. 4.11: Normalized frequency, dissipation, and FWHM variations for ionophore I₂ based QCM sensor against various ions amounts (—0, —5, —25, —250, —500, and —1000 ppm) in time

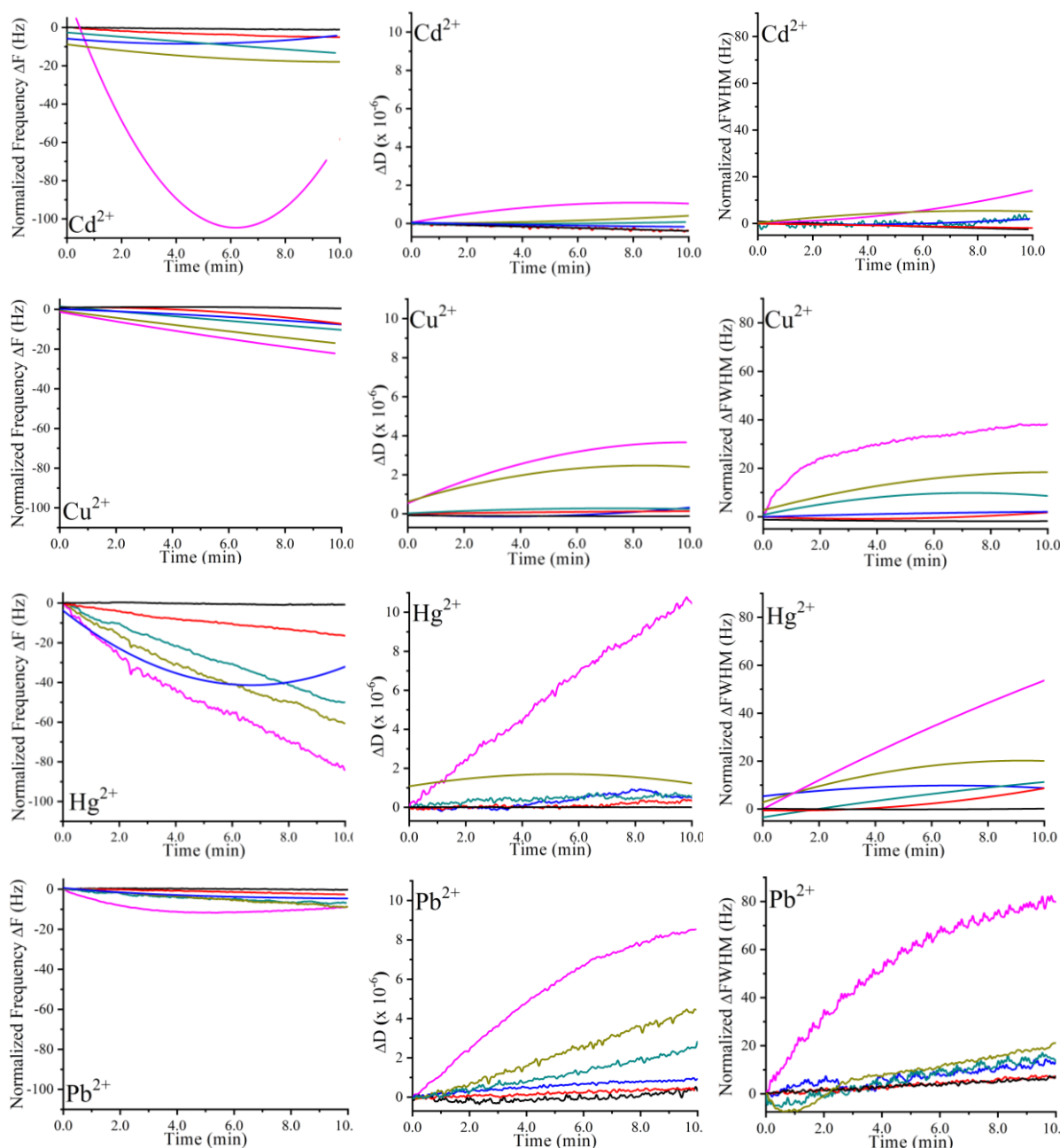


Fig. 4.12: Normalized frequency, dissipation, and FWHM variations for compound I_3 based QCM sensor against various ions amounts (—0, —5, —25, —250, —500, and —1000 ppm) in time

4.5 Electrochemical characterization

4.5.1 Cyclic voltammetry (CV) and Square wave voltammetry (SWV)

The electrochemical behavior of the sensing platforms was preliminarily examined employing CV. **Fig. 4.13** presents the CV signatures of the bare and modified electrodes in the presence and **absence** of ions. As displayed in **Fig. 4.13**, no significant analytical signals (Redox peaks) appeared in the absence of ions for the bare (a) and modified electrodes (c) in 0.2 M HCl. While, bare gold electrodes (b) presented moderate responses when the ions were added to the

electrolytic medium, and further modifications of the electrodes with ionophores I₁-I₃ (**d**) have enhanced the well-defined oxidation current peaks of heavy metals on their respective potentials. However, the cathodic reduction peaks of heavy metals are not well-separated and intense as the anodic ones. The observed increase in the CV current peaks of heavy metals after the modification of electrodes is owing to the fast electron-transfer rate at the ionophores@electrodes platforms and their conductive nature, besides the complexation or chelation process between the ions in electrolytic medium and the impregnated resorcinarenes in the electrodes.

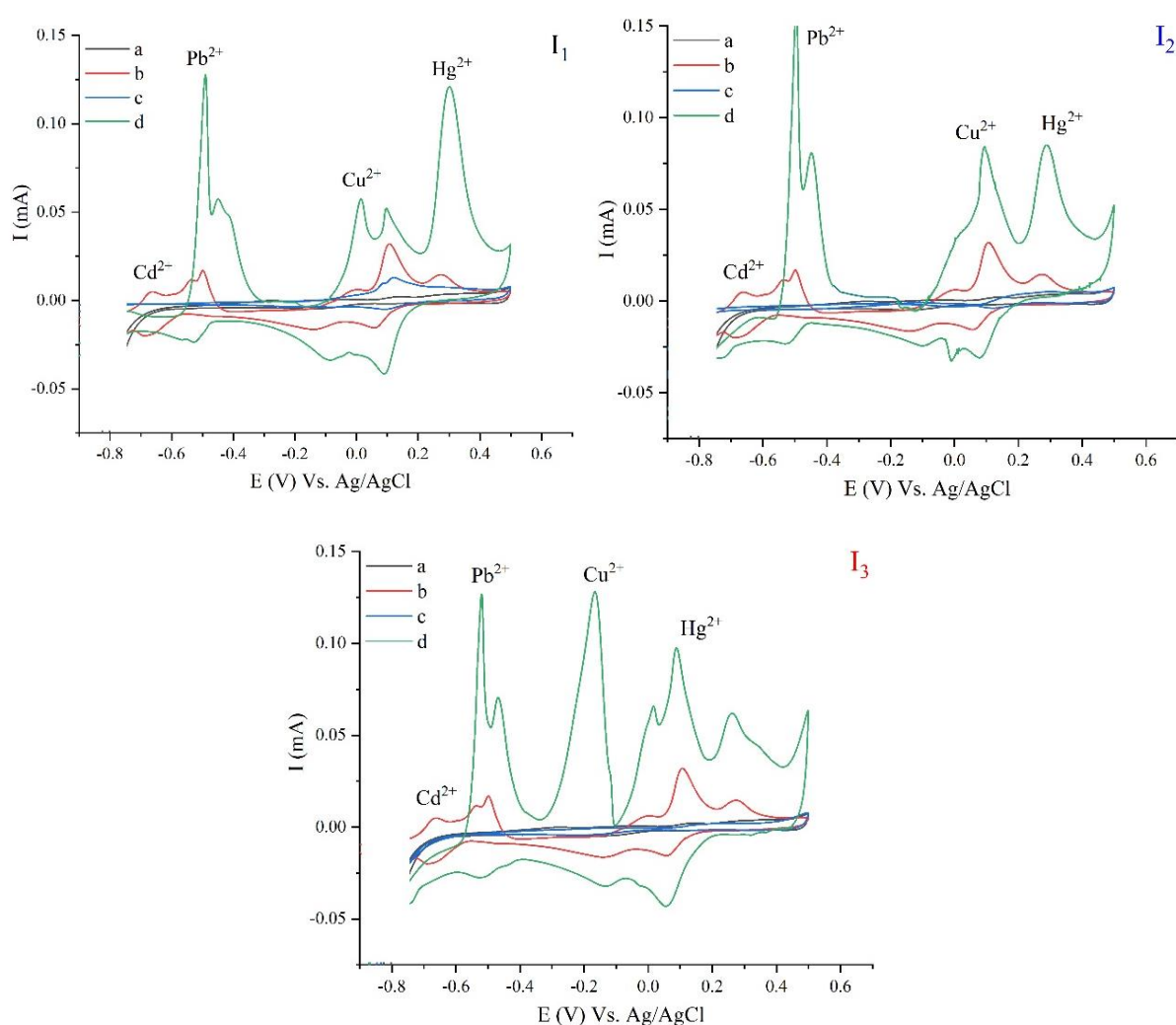


Fig. 4.13: Overlaid voltammograms of a) bare electrodes in 0.2 M HCl, b) bare electrodes in the presence of 1 ppm each of heavy metals in 0.2 M HCl, c) modified electrodes in 0.2 M HCl, d) modified electrodes in the presence of 1 ppm each of heavy metals in 0.2 M HCl.

The SWV signatures of the bare and modified electrodes in the presence and absence of heavy metals were also studied to complement the CV characterization and are shown in **Fig. 4.14**

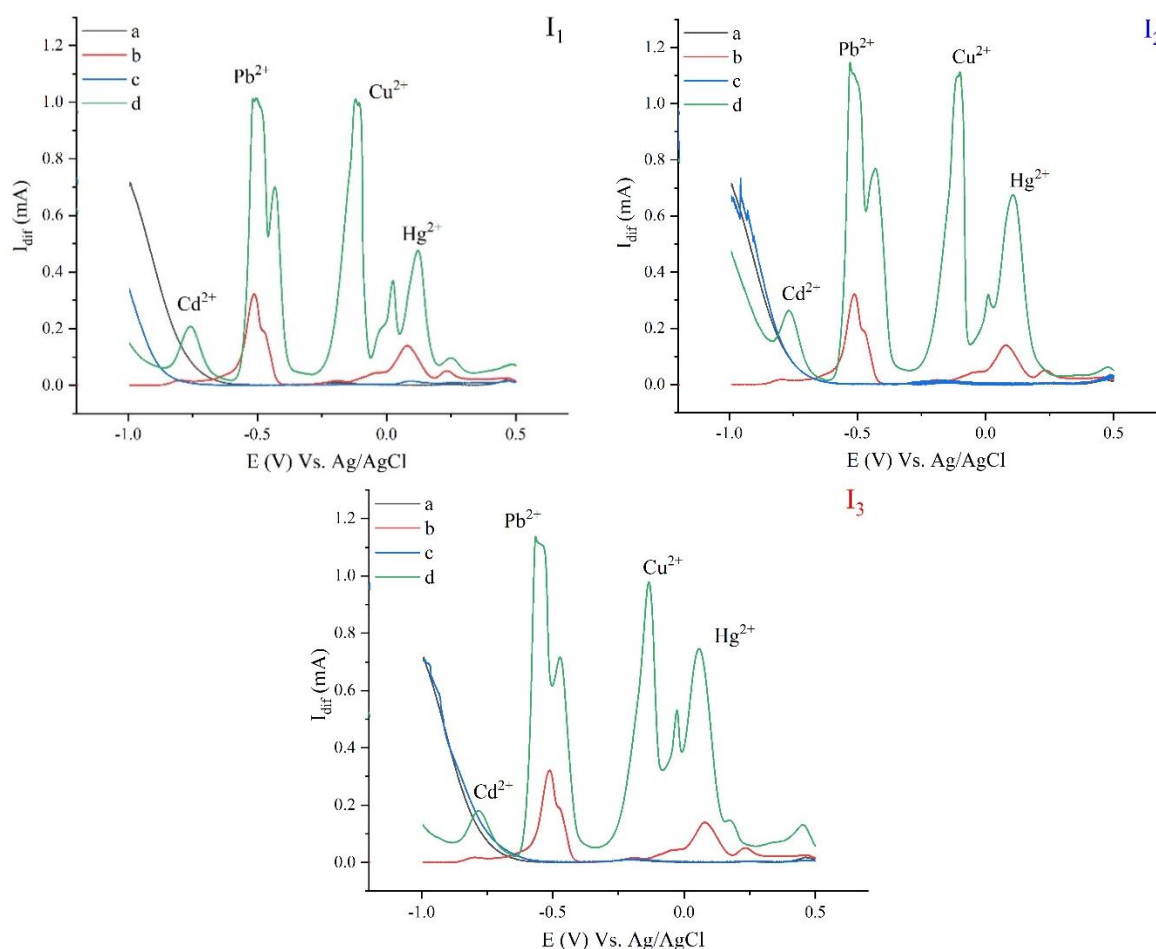


Fig. 4.14: SWV signatures of a) bare electrodes in 0.2 M HCl, b) bare electrodes in the presence of 1 ppm each of heavy metals in 0.2 M HCl, c) modified electrodes in 0.2 M HCl, d) modified electrodes in the presence of 1 ppm each of heavy metals in 0.2 M HCl.

The SWV signatures are in decent agreement with the CV results, where the bare (**a**) and modified electrodes (**c**) did not represent any anodic signal. After adding the heavy metals to the medium, the appearance of net well-separated peaks of heavy metals centered at their pertaining potentials was noticed with enhanced current intensity when coming to the ionophores@electrodes (**d**) compared to the bare gold electrodes (**b**), meaning that the sensitivity of the electrodes has increased notably after their modification, owing to the heavy metals accumulation on their surfaces, the high adsorption capacity, and the large electroactive surface of resorcinarenes platforms.

4.5.2 Electrochemical impedance spectroscopy (EIS)

The EIS technique was employed for characterizing the interface (solution/electrodes surfaces), the gained EIS outcomes were plotted in a Nyquist diagram form showing the real and imaginary parts of the impedance (**Fig. 4.15**). The Nyquist plots displayed a semicircle in the high frequencies associated with an electron transfer limited process, and a further line at low frequencies, indicating a diffusion-controlled process.

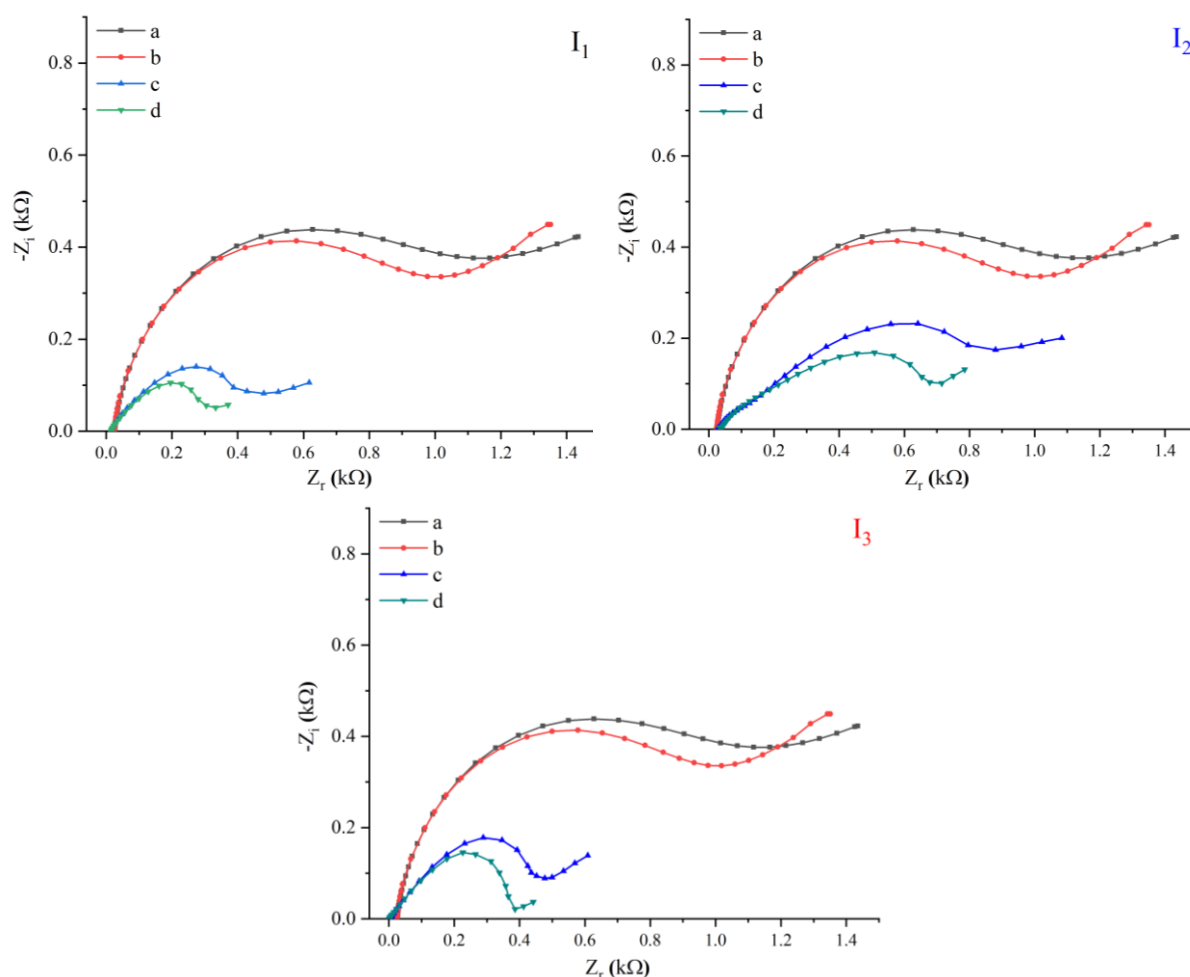


Fig. 4.15: EIS Nyquist plots of **a**) bare electrodes in 0.2 M HCl, **b**) bare electrodes in the presence of 1 ppm each of heavy metals in 0.2 M HCl, **c**) modified electrodes in 0.2 M HCl, **d**) modified electrodes in the presence of 1 ppm each of heavy metals in 0.2 M HCl.

In the case of bare electrodes **Fig. 4.15 (a)** and **(b)**, the semicircle diameter equal to the charge transfer resistance (R_{ct}) decreased after the addition of 1 ppm of heavy metals in 0.2 M HCl. Further decrease in R_{ct} was revealed after modifying the electrodes' surfaces with different ionophores **Fig. 4.15 (c)** and **(d)**. The smallest R_{ct} values were associated with the modified electrodes in the presence of 1 ppm of heavy metals in 0.2 M HCl **(d)**. The decrease in R_{ct}

values of the modified electrodes indicates the electrode surface conductivity improvement from one side and the enhanced electron transfer properties from another.

4.6 Optimization of the physicochemical parameters

The optimization study of various parameters affecting the sensing of heavy metals was examined employing square wave voltammetry (SWV). The supporting electrolyte, pH, accumulation potential, and accumulation time were adjusted to conclude the best conditions for achieving an enhanced detection.

4.6.1 Effect of supporting electrolyte

The electrolytic solution plays a vital role in boosting the medium's conductivity where the electrochemical detection is taking place, supporting electrolytes viz. 0.2M HCl ($\text{pH}_i = 0.7$), KCl 0.2M ($\text{pH}_i = 6.8$), and ACB 0.2M ($\text{pH}_i = 5.3$) were employed herein for selecting the appropriate one to be utilized in further detection investigations.

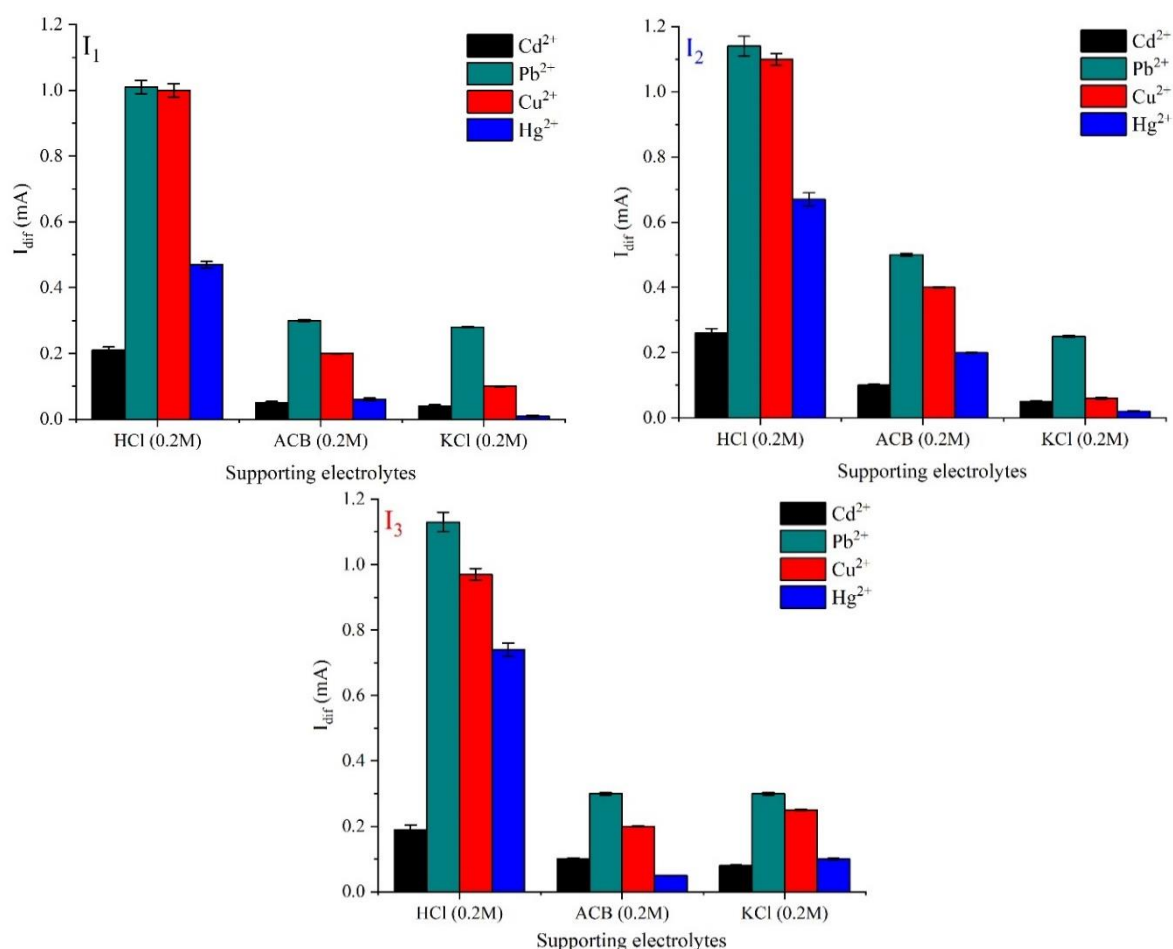


Fig. 4.16: Influence of various supporting electrolytes on the electrochemical signals of the modified electrodes in presence of 1 ppm each of heavy metals.

In **Fig. 4.16**, it was observed that the uppermost SWV current intensities were obtained utilizing 0.2 M HCl as an electrolytic medium, which is explained by its greater conductivity ensuring a fast charge transport process of the heavy metals and stabilizing them at the modified electrode's surface. Therefore, 0.2 M HCl was selected as the optimal supporting electrolyte to be used in further detection studies.

4.6.2 Effect of pH

The complexation process of the heavy metals within the resorcinarenes@electrodes is highly affected by the medium's pH. Hence, the sensing of heavy metals in HCl 0.2 M ($\text{pH}_i = 0.7$) has been examined by adjusting the pH values over a range from 0.7 to 8 (**Fig. 4.17**).

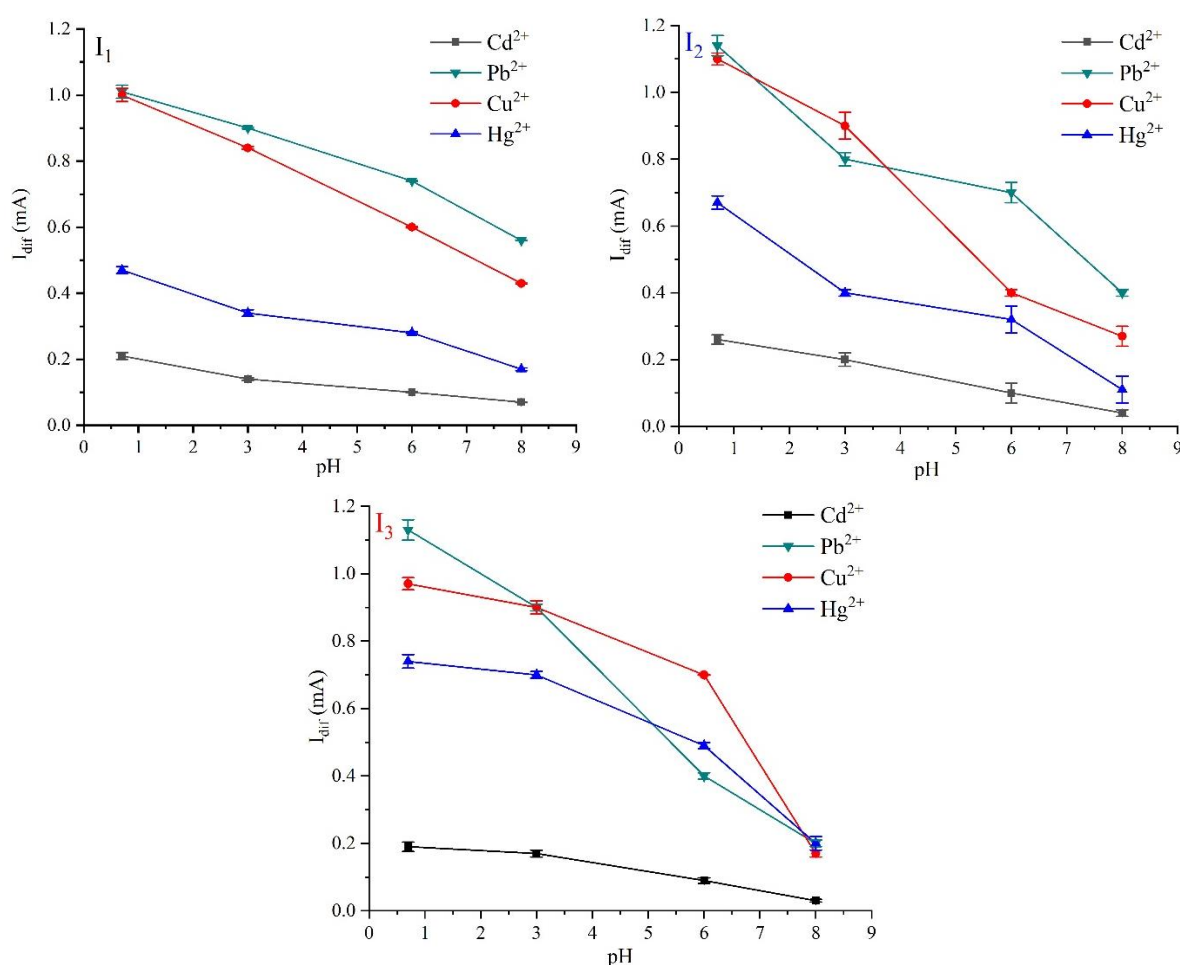


Fig. 4.17: Influence of different pH values on the SWV signals of the modified electrodes in presence of 1 ppm each of heavy metals in 0.2 M HCl ($\text{pH}_i = 0.7$).

The optimal pH of 0.2 M HCl for obtaining the highest current is 0.7 (**Fig. 4.17**), which is applied in further SWV detection studies. However, while increasing the pH, a decrease in the peak current values was observed for all heavy metals, explained by their hydrolysis and the

formation of insoluble metal hydroxides on the electrode surface at higher pH values, causing current fluctuations and decrease.

4.6.3 Effect of accumulation time

The effect of accumulation time on the SWV signals was studied from 30 to 180 s (**Fig. 4.18**), the current values increased upon the increase of accumulation time up to 90s, owing to the progressive buildup of heavy metals on the modified electrodes' surfaces. After 90 s, the current values dropped gradually due to the surface saturation process, meaning that the equilibrium conditions between the complexed heavy metals and those present in the electrolytic solution were achieved. The 90 s accumulation time was selected as optimal and was employed in further electrochemical examinations.

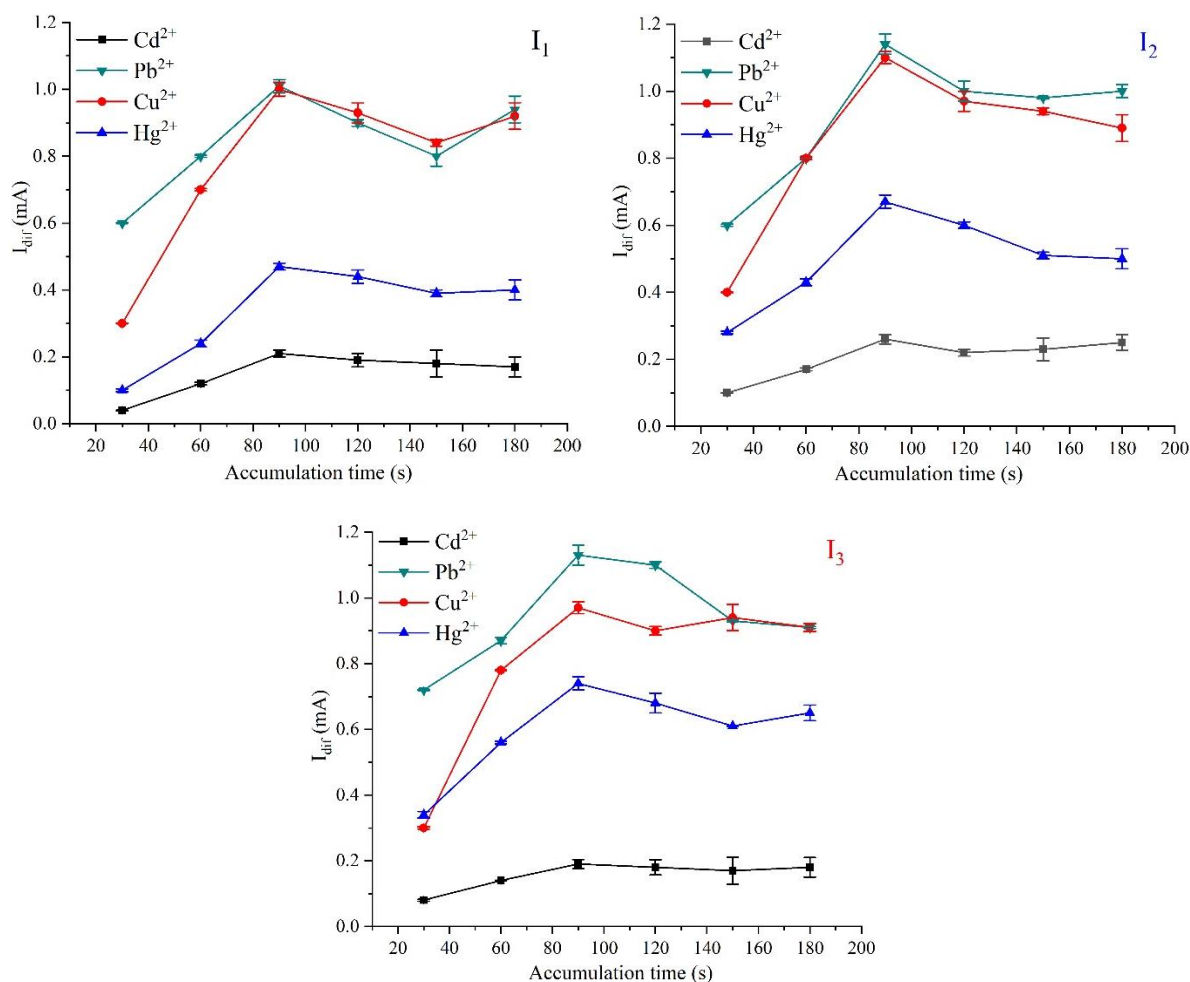


Fig. 4.18: Influence of accumulation time on the SWV signals of the modified electrodes in presence of 1 ppm each of heavy metals in HCl 0.2 M (pH = 0.7).

4.6.4 Effect of accumulation potential

The effect of accumulation potential on the SWV current peaks of heavy metals was examined in a potential frame ranging from -1V to -2V (**Fig. 4.19**), the peak currents of various heavy metals reached their maximum at -1.2 V. Once the potential is shifted towards more negative values, a decrease in the peak currents of heavy metals is observed. Generally, such trend is explained by the hydrogen evolution reaction, this later was proved by the presence of bubbles on the electrodes' surfaces during the measurements. So, an accumulation potential of -1.2 V was employed in further studies as optimal.

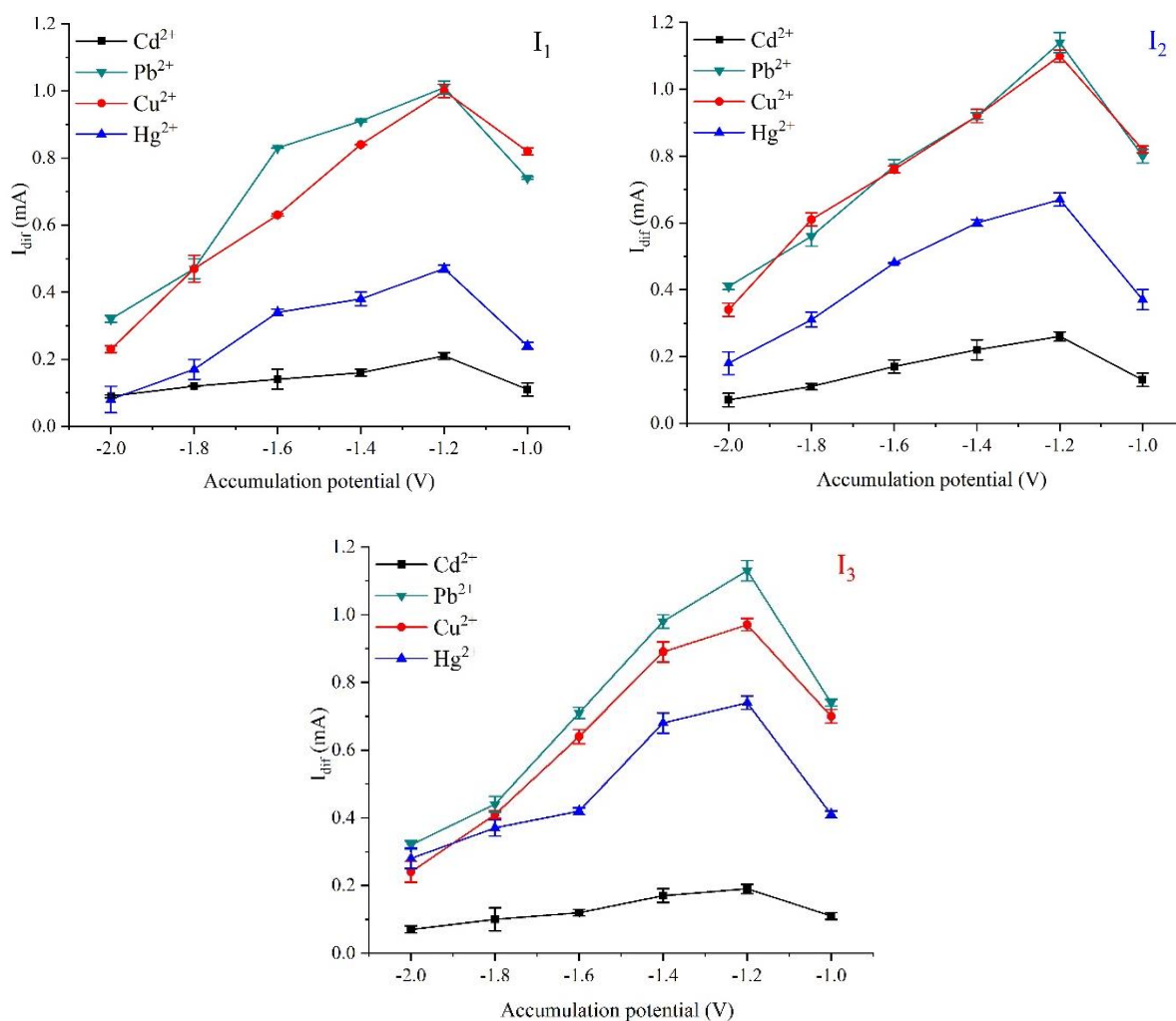


Fig. 4.19: Influence of accumulation potential on the SWV signals of the modified electrodes in presence of 1 ppm each of heavy metals in 0.2 M HCl (pH = 0.7).

C

hapter 5: Discussions

5.1 Introduction

- The Langmuir results are analyzed, in terms of limiting area variations and ionic selectivity, and the potential interfacial complexation mechanism is discussed;
- The sensing characteristics (detection limits, quantification limits, linear ranges, sensitivity, and selectivity) from the quartz crystal microbalance are stated, moreover, the piezogravimetric detection mechanism is deliberated;
- The detection features from the electrochemical results, besides the interferences studies and the evaluation of the repeatability and reproducibility of the sensors, are indicated, and the electrochemical detection mechanism is debated.

5.2 Langmuir isotherms

Convenient information on Langmuir ultra-thin films is obtained through phase evolutions, a schematic of a typical surface pressure-area (Π -A) isotherm demonstrating these transitions is displayed in **Fig. 5.1**.

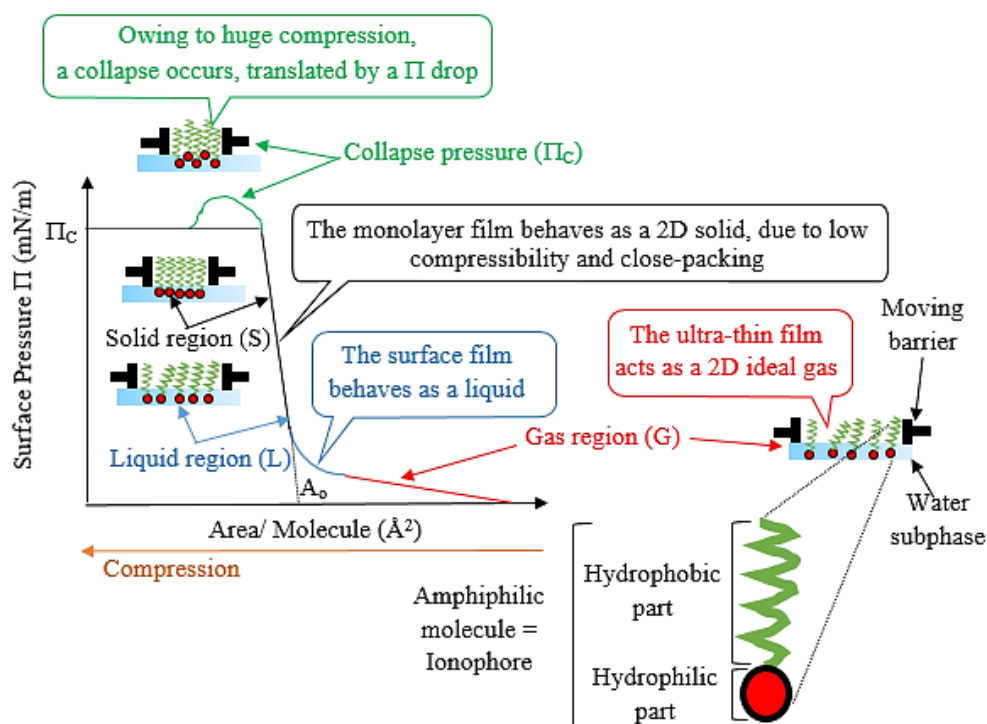


Fig. 5.1: Langmuir isotherm schematic highlighting various monolayers' phases.

To simplify the task, the two-dimensional (2D) Langmuir film is having a more or less resemblance to the three-dimensional (3D) solid, liquid, and gas states, it acts as a 2D gas if the area/molecule is adequately high (No interactions between amphiphilic molecules are taking place), resembling a 3D gas state. Initial monolayer compression leads to a 2D expanded liquid (1st phase transition), this state is equivalent to a regular 3D liquid. Further compression causes condensation of the expanded liquid phase and leads to a 2D condensed liquid (2nd phase transition), this later is comparable to a 3D liquid-solid evolution but does not give a real 2D solid at all times. After this stage, the monolayer collapses in a 3D stacking and loses its properties.

5.2.1 Limiting area variations and their effect on ionic selectivity

The variations of A_{lim} (*Limiting area/molecule: acquired via extrapolation of the Langmuir isotherm's linear part on the X-axis*) are a robust indication of interactions occurring at the monolayer/subphase level. While using ionophores as ultra-thin films for potential detection applications targeting heavy metals. The complexation reactions between the ionophores and the heavy metals are translated by an A_{lim} increase while adjusting the ions amounts. Though, depending on the favorable electronic interactions, ionic selectivity against the ions present in the subphase is performed by ionophores. **Fig. 5.2** illustrates the A_{lim} dependence on the heavy metals concentrations for ionophores I₁-I₃, whereas the A_{lim} values are recapitulated in **Tables C.1-3 (Appendix C)**.

As seen in **Fig. 5.2**, in the case of *cadmium* subphase, the A_{lim} values were obtained at ~110, ~130, ~160, ~185 Å²/Molecule for I₁, at ~105, ~150, ~220, ~320 Å²/Molecule for I₂, and at ~240, ~550, ~580, ~630 Å²/Molecule for I₃ sequentially for 0, 5, 25, 250 ppm.

Through rising *copper ions* amounts in the subphase, the A_{lim} values increased accordingly ~110, ~150, ~200, ~320 Å²/Molecule for I₁, ~105, ~140, ~370, ~450 Å²/Molecule for I₂. and for I₃ at ~240, ~270, ~440, ~700 Å²/Molecule consecutively for 0, 5, 25, 250 ppm.

Considering the *mercury* subphase, the A_{lim} values were ~110, ~220, ~240, ~300 Å²/Molecule for I₁, ~105, ~220, ~290, ~310 Å²/Molecule in case of I₂. Also, ~240, ~320, ~480, ~600 Å²/Molecule for I₃ for pure water, 5, 25, 250 ppm sequentially.

Likewise, for *lead ions*, the limiting areas were ~110, ~150, ~275, ~320 Å²/Molecule for I₁, ~105, ~160, ~170, ~300 Å²/Molecule in case of I₂, and at ~240, ~450, ~490, ~620 Å²/Molecule in case of I₃ for 0, 5, 25 and 250 ppm serially.

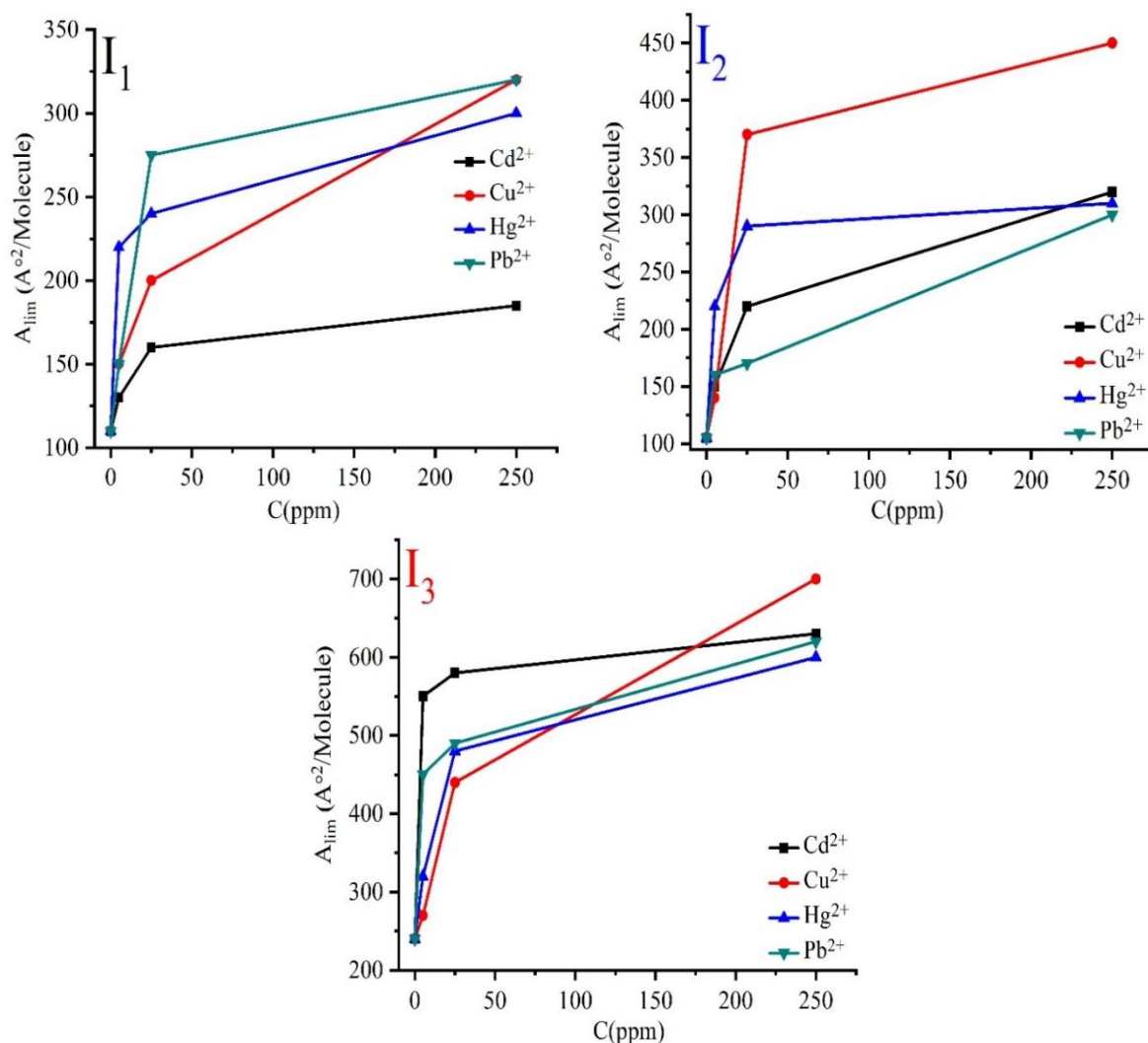


Fig. 5.2: Limiting area (A_{lim}) dependence on heavy metals concentration for ionophores I₁-I₃.

The notable systematic increase in terms of limiting area detailed in the previous paragraphs is disclosing the high inclusion taking place at the water/air interface level, it indicates similarly that all ionophores were capable of binding to various cations from one side, and demonstrates the incorporation and integration (via complexation reactions and electrostatic interactions) of these cations within the resorcinarene monolayers from another. As revealed previously, ionic selectivity is distinguished, specifically as follows:

Order of A_{lim} for I₁: (I₁)-Pb²⁺ > (I₁)-Hg²⁺ > (I₁)-Cu²⁺, (I₁)-Cd²⁺,

Order of A_{lim} for I₂: (I₂)-Cu²⁺ > (I₂)-Hg²⁺ > (I₂)-Cd²⁺, (I₂)-Pb²⁺,

Order of A_{lim} for I₃: (I₃)-Cd²⁺ > (I₃)-Pb²⁺ > (I₃)-Hg²⁺, (I₃)-Cu²⁺.

The above sequences indicate that I₁ is selective to lead ions, I₂ is selective to copper ions over others, and I₃ presented a higher selectivity towards cadmium ions.

5.2.2 Heavy metals adsorption within oligomeric ultra-thin films

The Langmuir isotherms' stability is a crucial factor in inspecting interactions between the monolayers and the subphase, this feature renders in forming well-ordered and insoluble stable ultra-thin films capable of interacting with target elements. On account of the resorcinarenes' amphiphilic characteristics, enclosing all at once hydrophilic and hydrophobic parts, this key parameter is present. The prospective orientation assumptions of ligands I₁, I₂, and I₃ is manifesting in a cone conformation at the interface level, supported by hydrogen bindings between the subphase-water molecules and the resorcinols' hydroxyl (I₁-I₃) and amine groups (I₃), other substituents as alkene and alkane chains are hydrophobic and supposed to front the air, while the ionophores' common ring is parallel to the water-air interface as clarified in **Fig. 5.3**, whereas **Fig. 5.4** displays the potential interfacial interaction mechanism between the ions and the ligands.

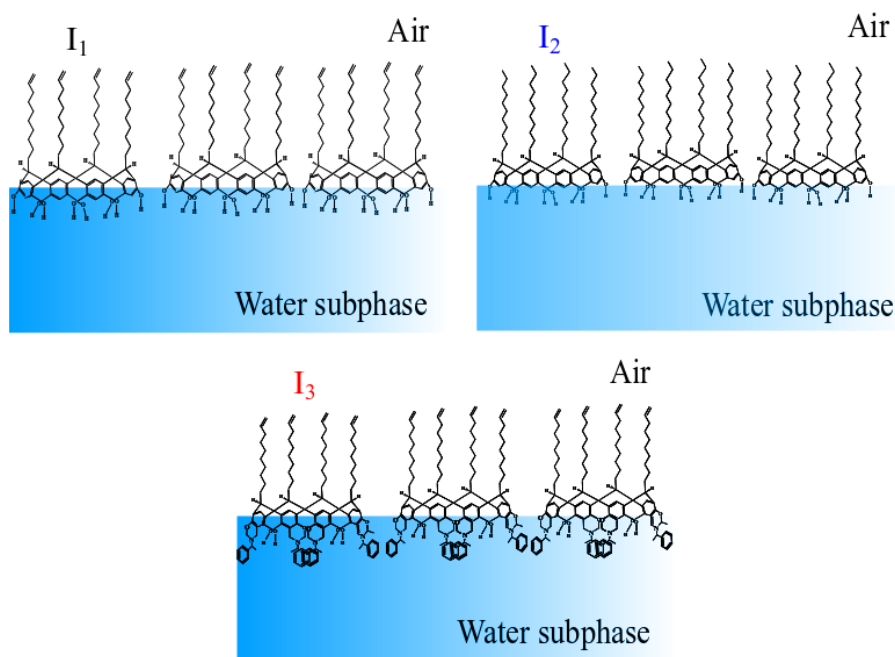


Fig. 5.3: Prospective arrangements of ionophores I₁-I₃ on the water-air interface

The heavy metals' adsorption within Langmuir monolayers is mainly quantified by assessing interfacial tensions in the function of heavy metals amounts, constructing the Gibbs adsorption isotherm, and simply interpreted by the Gibbs equation (Eq. (5.1)).

$$d\gamma = -\Gamma^{HM}RTd\ln(a_{HM}) \quad (5.1)$$

Where γ , T , R , a_{HM} , and Γ^{HM} are the surface tension, the temperature, the universal gas constant, the heavy metals' activity and the heavy metals' adsorption factor respectively.

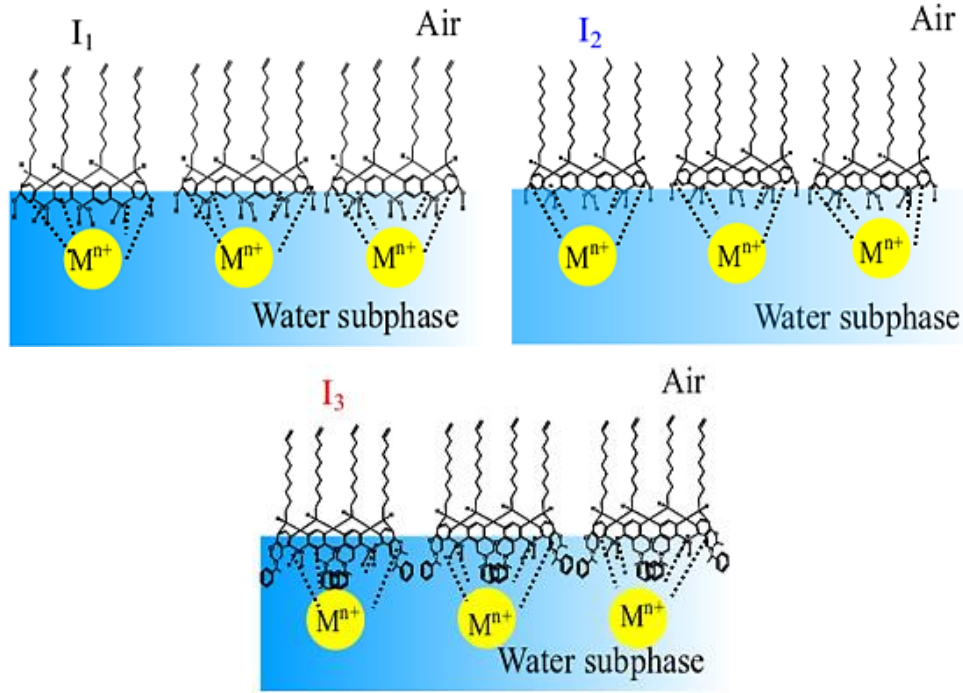


Fig. 5.4: Potential interfacial complexation mechanism between ionophores I₁-I₃ and the heavy metals ($M^{n+} = Cd^{2+}, Cu^{2+}, Hg^{2+}$ and Pb^{2+}).

Approximately, the Γ^{HM} equals the Γ_{max}^{HM} considered as the heavy metals' maximum adsorption factor, additionally the heavy metals' activities are equivalent to their concentrations ($a_{HM} \sim C_{HM}$) in diluted solution conditions. The integration of (Eq. (5.1)) leads to the so-called 'Gibbs-Shishkovsky' empirical equation Eq. (5.2) [157].

$$\Pi_c^{H_2O} - \Pi_c^{HM} = b \ln(C_{HM}) \quad (5.2)$$

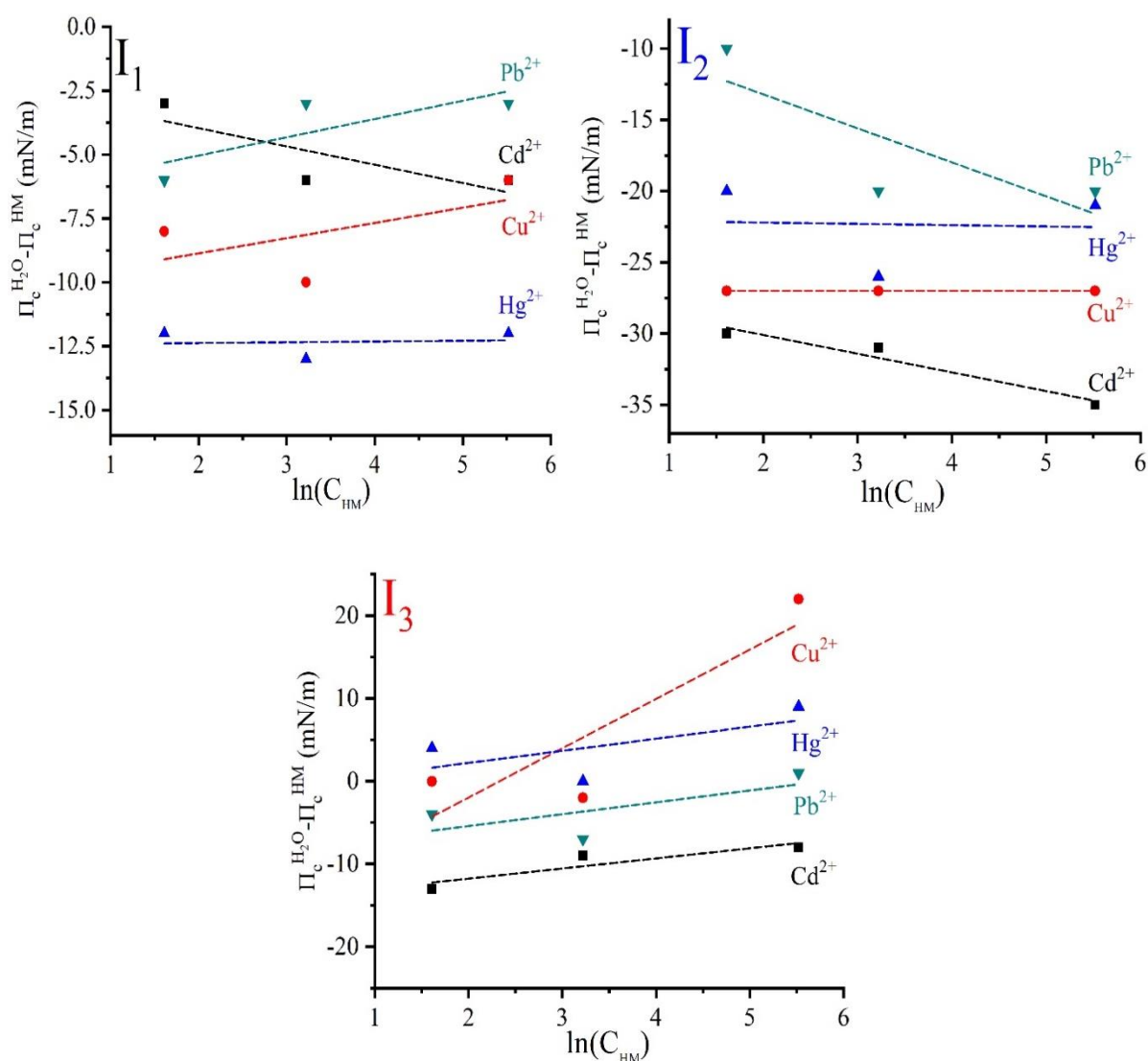
The benefit of Eq. (5.2) manifests in plotting the collapse pressure variations ($\Pi_c^{H_2O} - \Pi_c^{HM}$), calculated from the isothermal data, vs. $\ln(C_{HM})$, and by extracting Γ_{max}^{HM} from the slope ' b ' of the Gibbs isotherm as shown in Eq. (5.3):

$$b \sim \Gamma_{max}^{HM} RT \quad (5.3)$$

The Gibbs adsorption isotherms of I₁-I₃, better known as Γ_{max}^{HM} definition plots are displayed in **Fig. 5.5**, from this later, it is obvious that the collapse pressure variations were affected by the presence of the heavy metal in the subphase, which was translated by nearly linear plots for all ionophores, and maximal adsorptions as described in **Table 5.1**.

Table 5.1: $\Gamma_{\max}^{\text{HM}}$ values for ionophores I₁, I₂, I₃.

Various ions	$\Gamma_{\max}^{\text{HM}} * 10^{-7} \text{ (mol.m}^{-2}\text{)}$		
	I ₁	I ₂	I ₃
Cd ²⁺	- 2.93	- 5.37	5.01
Cu ²⁺	2.44	0	24.40
Hg ²⁺	0.12	- 0.36	6.00
Pb ²⁺	2.93	- 9.77	5.86

**Fig. 5.5:** $\Gamma_{\max}^{\text{HM}}$ definition plots for ionophores I₁-I₃ in the function of heavy metals' amounts

5.3 Quartz Crystal Microbalance with Impedance measurement (QCM-I)

The heavy metals sensing through the introductory application of Calix-based piezogravimetric sensors disclosed its success since the decrease in frequency with increasing the ions amounts

is directly related to the mass loading of heavy metals on the sensor's surface (Fig. 5.6 and Figs. 4.9-12). Another feature confirming this prospect is the full width at half maximum variation (Basis of a QCM-I measurement), showing a simultaneous increase, commonly the crystal's loading drives to the above-discussed shifts.

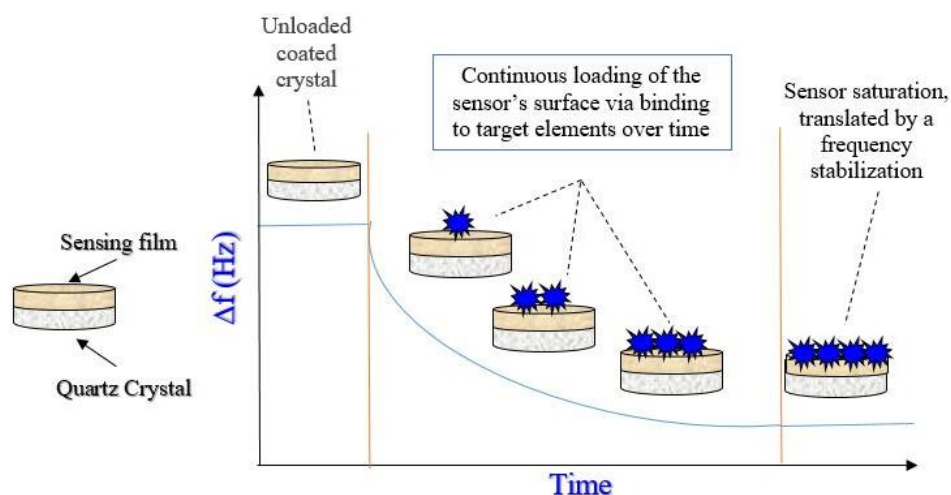


Fig. 5.6: Frequency variation upon continuous loading of the sensor's surface over time

The resorcinarene thin films' viscoelastic properties were monitored simultaneously with the frequency shifts (ΔF_n) and the full width at half maximum variations ($\Delta FWHM_n$), by recording the energy dissipation shifts based on the oscillation amplitude's variations in time (Via ring-down method). Generally, the higher is the dissipation shift ($\Delta D > 2 \times 10^{-6}$), the softer is the adlayer (Fig. 5.7), and accordingly, the viscoelastic model description cannot follow the Sauerbrey equation (Eq. (2.3)) [160].

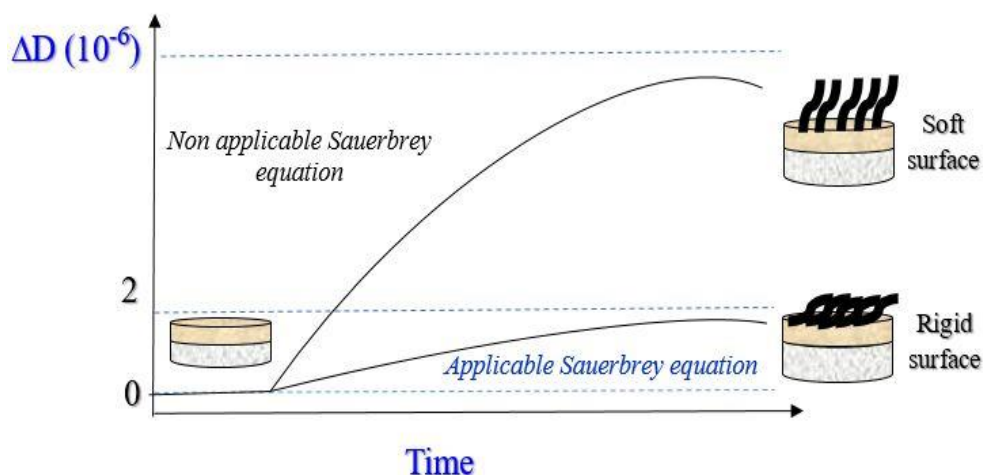


Fig 5.7: Dissipation energy factor variations in time

Exploring (Figs. 4.9-12), the dissipation shifts showed a significant viscoelastic character of the adlayer with increasing amounts of metals ions. The obvious thin films' soft coverage once the sensor is exposed to higher metals ions concentrations is possibly either due to a minor number of not attached macrocycles to the gold electrodes, or to loosely bound chains network.

5.3.1 Sensing characteristics

The sensors' applicability depends on their detection features manifesting in sensitivity (S), linear range (LR), the limit of detection (LOD), and the limit of quantification (LOQ). However, excellent sensing characteristics are considered as small LODs and LOQs, high sensitivities, and wide LRs. To evaluate the metrological parameters, the sensors' dynamic ranges based on the frequency and full width at half maximum variations for ionophores I₁-I₃ are presented in Fig. 5.8, whereas Table 5.2 is recapping those parameters.

The detection features were calculated from $LOD = 3.3\sigma/S$ and $LOQ = 10\sigma/S$, where σ is the standard deviation and S is the linear range's slope, or else the sensor's sensitivity. The developed detection platforms showed respectful sensing characteristics (wide linear responses, noble sensitivities, low LODs, and LOQs), either based on frequency or else on full-width variations, as can be seen in Table 5.2. The detection limits in the case of Hg²⁺, Pb²⁺, and Cd²⁺ ions were slightly higher than the recommended thresholds. However, in the case of Cu²⁺, they were inferior to the thresholds stated by WHO (2 ppm) and USEPA (1.3 ppm).

Table 5.2: Metrological parameters of resorcinarene-based QCM sensors.

Ionophores	HM ions	Detection features based on $\Delta F_n/n$				Detection features based on $\Delta FWHM_n/n$			
		LR (ppm)	S (Hz/ppm)	LOD (ppm)	LOQ (ppm)	LR (ppm)	S (Hz/ppm)	LOD (ppm)	LOQ (ppm)
I ₁	Cd ²⁺	2-25	1.571	0.61	1.83	250-1000	0.225	0.32	0.96
	Cu ²⁺	0.5-25	1.056	0.01	0.03	2-1000	0.052	0.57	1.71
	Hg ²⁺	3-25	1.215	0.88	2.64	1-500	0.093	0.37	1.11
	Pb ²⁺	2-1000	0.045	0.47	1.42	3-500	0.057	0.89	2.67
I ₂	Cd ²⁺	5-25	0.215	1.82	5.46	5-1000	0.021	1.63	4.90
	Cu ²⁺	250-1000	0.554	0.87	2.61	1-250	0.028	0.18	0.54
	Hg ²⁺	5-250	0.039	2.53	7.59	3-500	0.030	0.76	2.28
	Pb ²⁺	2-500	0.080	0.48	1.46	1-1000	0.048	0.20	0.60
I ₃	Cd ²⁺	5-500	0.040	1.50	4.50	3-1000	0.009	0.89	2.96
	Cu ²⁺	5-1000	0.010	0.93	2.79	1-1000	0.038	0.20	0.66
	Hg ²⁺	3-25	1.171	0.99	2.99	0.5-1000	0.030	0.11	0.36
	Pb ²⁺	25-1000	0.008	0.45	1.35	5-1000	0.034	1.77	5.31

The selectivity evaluation based on frequency shifts (Fig. 5.8) indicates that I₁ is selective to Hg²⁺ and Cd²⁺, I₂ to Cu²⁺ and Pb²⁺, whereas I₃ is selective to Hg²⁺ and Cd²⁺, this appraisal is in good agreement with the ionic binding preferences from the Langmuir results.

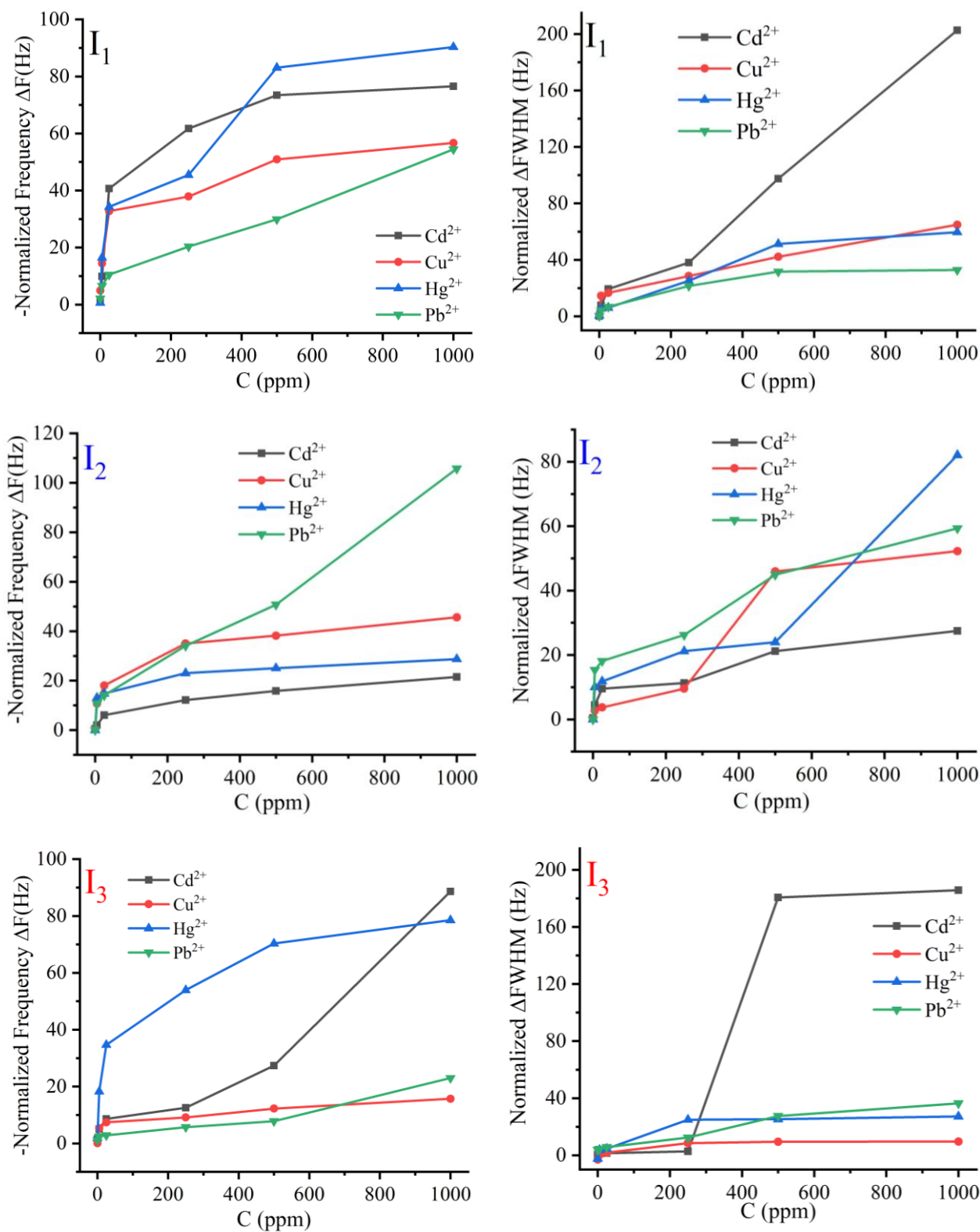


Fig. 5.8: Dynamic ranges for ionophores I₁-I₃ based on the normalized frequency and full width at half maximum variations.

5.3.2 Ionophores' attachment on the gold surface

Ensuring the best performance of the developed sensors, detection platforms should be well attached and well-constructed, the ligands affixation on the quartz crystal surface is then ascertained by electrostatic interactions (Mainly Van der Waals (*VDW*) dispersion forces with a quantum mechanical nature, manifesting in dipoles produced via quantum fluctuations) between heteroatoms, i.e. O, N, aromatic cycles' electrons, end carbon chain double bonds, and the gold surface. Reimers et al. [161] showed that aromatic cycles and carbon chains interact strongly with coinage metals-based surfaces such as gold, resulting in their adsorption via *VDW* interactions comparable to covalent attachment in terms of strength. For a clarified overview, the free gold atoms can either react with their 'd' or 's' orbitals ($d^{10}s^1$ as electronic valence configuration), due to their high reactivity and capability of covalent binding to carbon atoms forming single, double, and even triple bonds [162,163]. However, when gold atoms are attached forming a single Au-Au bond via s-s orbitals, their reactivity weakens, which is the case of noble gold surfaces, yet, this fact is not disturbing the *VDW* dispersive forces for those bonds formed via 'd' orbitals of gold surface and carbon atoms as an example [164,165]. Besides the later interaction, electron flow between N, O, and gold surface atoms is ensured through a moment dipole polarization creating an electron density stream.

5.3.3 Ionophores' affinity toward heavy metals

The full width at half maximum shifts ($\Delta FWHM$) of piezogravimetric sensors coated with ionophores I₁-I₃ for the affinity evaluation toward Pb²⁺, Hg²⁺, Cd²⁺, and Cu²⁺ in aqueous solution, were plotted in the form of Radar plots, the variations in $\Delta FWHM$ are offered for each ion (Cd²⁺, Hg²⁺, Pb²⁺, and Cu²⁺), at each concentration (5, 25, 250, 500, and 1000 ppm), and combining the response of the three calixresorcinarenes at the same time, this approach is advantageous to understand the chemosensors' detection performances and it is recommended to comprehend the sensing behavior and affinities of different oligomers towards the ions in aqueous solutions. When comparing responses of the studied potential sensors (**Figs. 5.9-12**), it's revealed that I₃ had moderate detection ability towards all heavy metals ions with selective preferences, though compounds I₁ and I₂ had significantly powerful interactions and high binding affinities.

From **Fig. 5.9**, it's notable that I₁ showed the highest detection sensitivity toward Cd²⁺ ions at all tested concentrations while I₂ was effective at lower concentrations (5 and 25 ppm). As the amount of cation increased, the sensitivity of I₂ decreased slightly. I₃ produced low sensitivity.

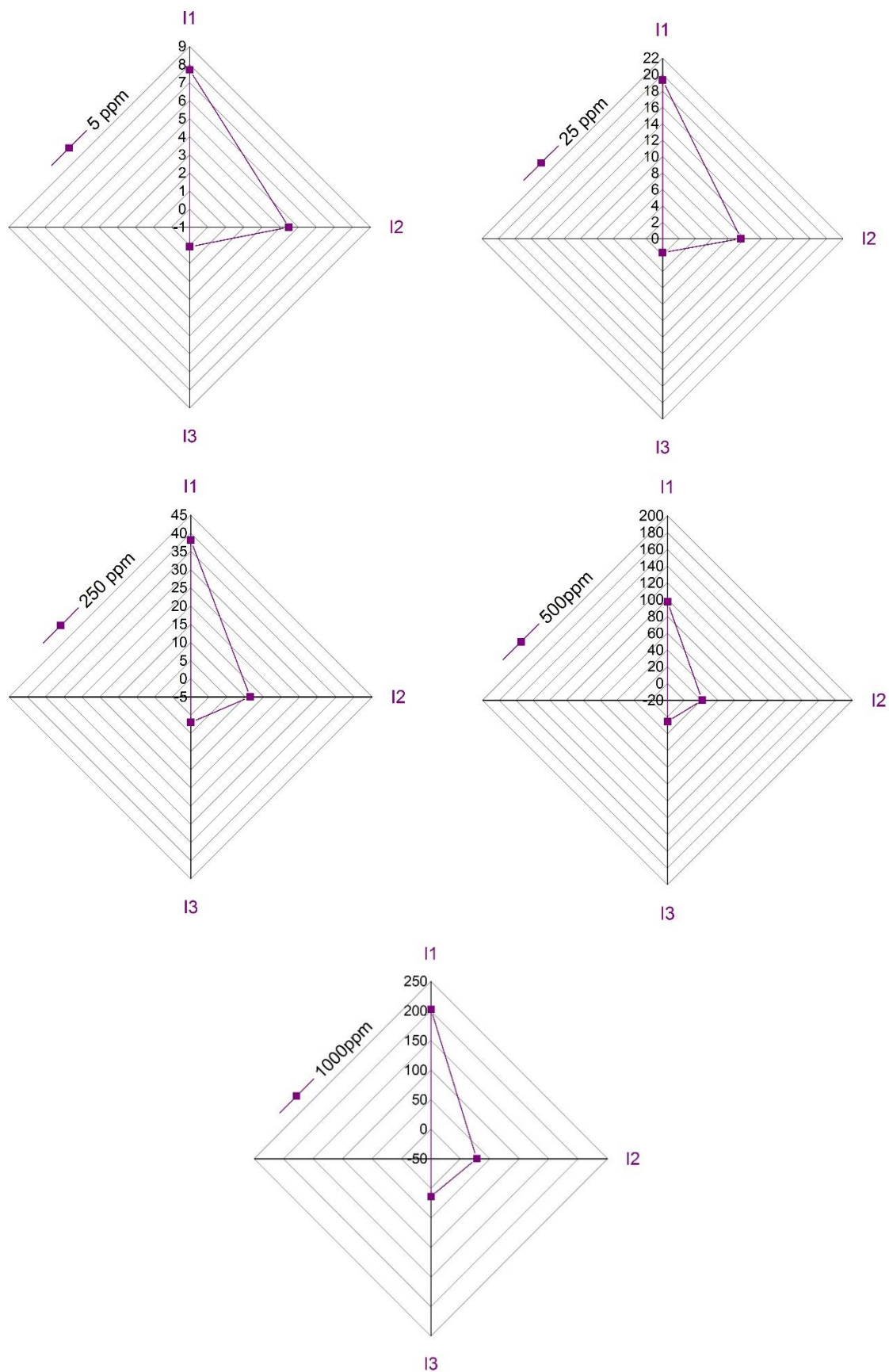


Fig. 5.9: Full width at half maximum variations of the Calix-QCM chemosensors (I₁, I₂, I₃) for different concentrations (5, 25, 50, 500, and 1000 ppm) of Cd^{2+} .

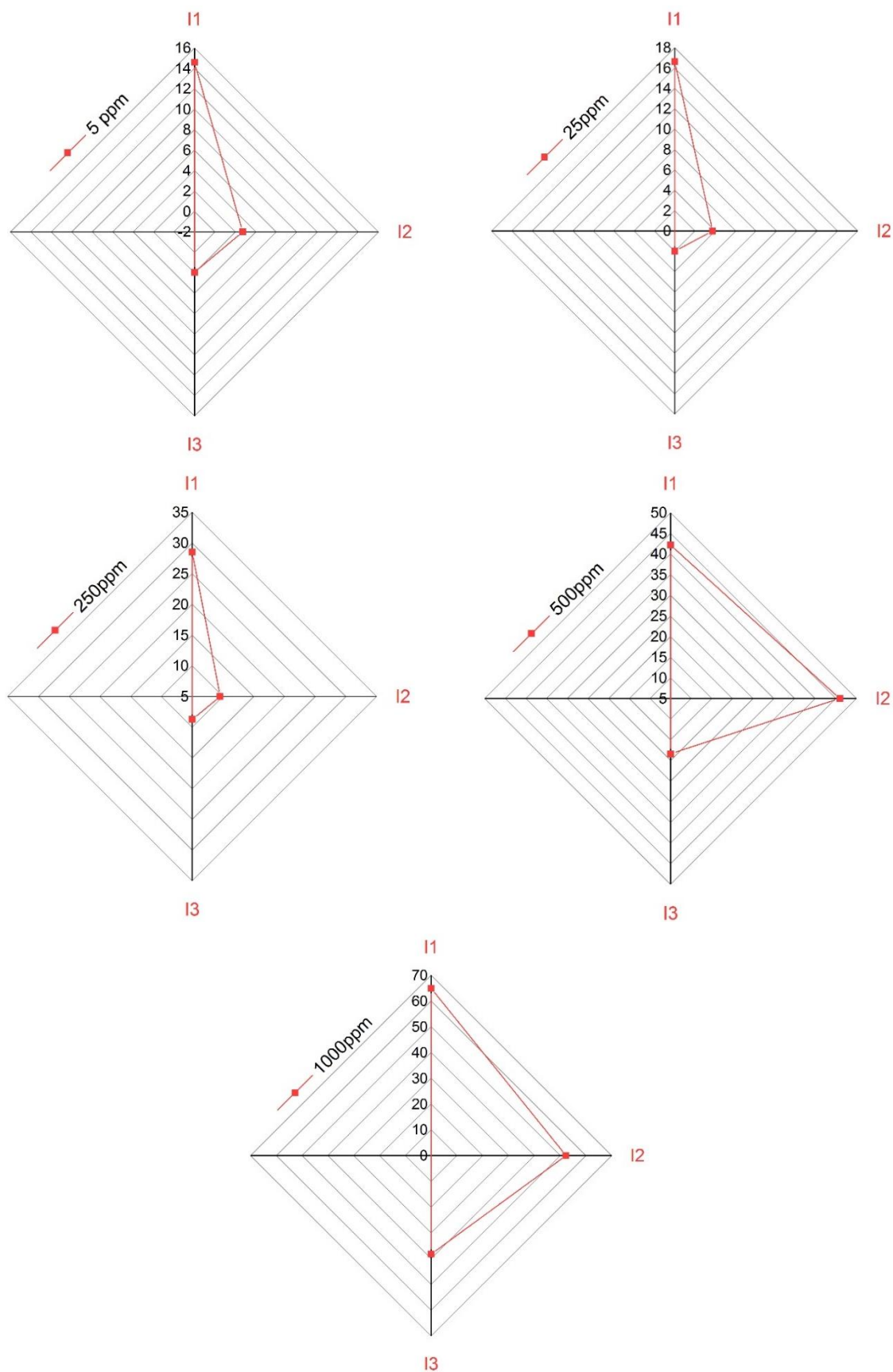


Fig. 5.10: Full width at half maximum variations of the Calix-QCM chemosensors (I_1 , I_2 , I_3) for different concentrations (5, 25, 50, 500, and 1000 ppm) of Cu^{2+} .

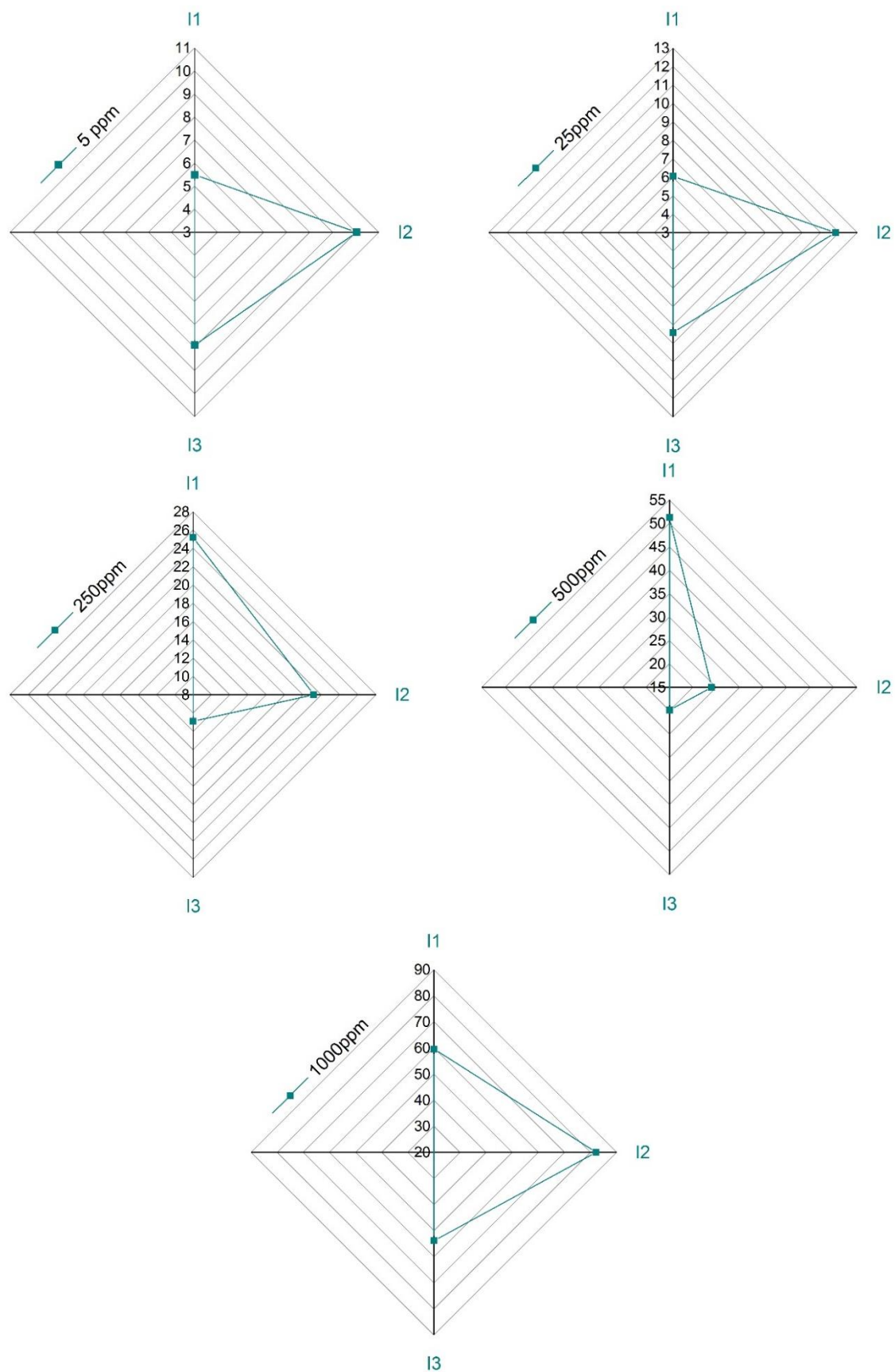


Fig. 5.11: Full width at half maximum variations of the Calix-QCM chemosensors (I_1 , I_2 , I_3) for different concentrations (5, 25, 50, 500, and 1000 ppm) of Hg^{2+} .

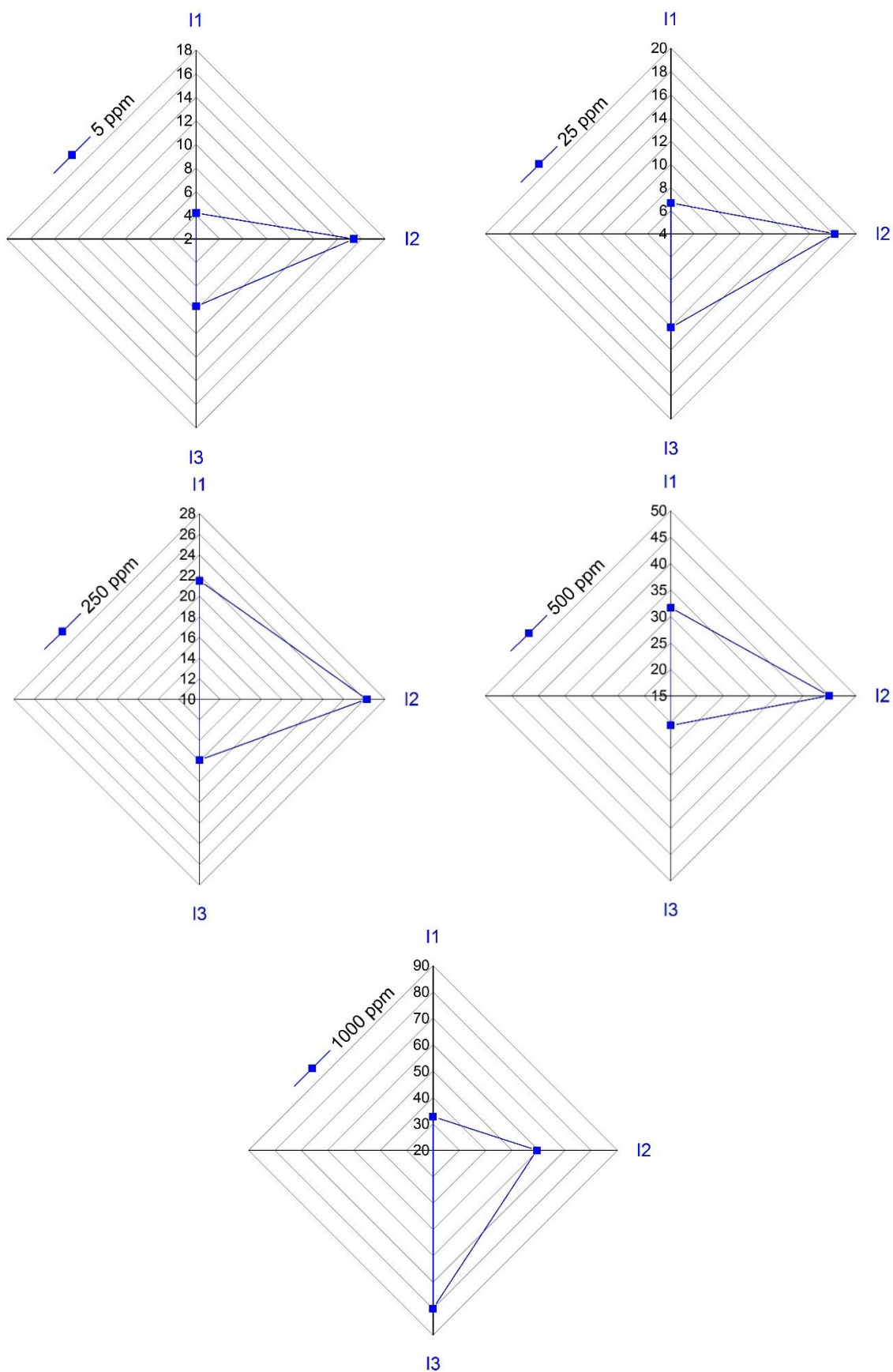


Fig. 5.12: Full width at half maximum variations of the Calix-QCM chemosensors (I_1 , I_2 , I_3) for different concentrations (5, 25, 50, 500, and 1000 ppm) of Pb^{2+} .

Fig. 5.10 is associated with the detection of Cu^{2+} ions by ionophores I_1 - I_3 at different amounts, it's revealed that I_1 produced the best detection sensitivity all over the concentration range and the detection increased by increasing the Cu^{2+} concentration. I_2 showed good detection at concentrations above 500 ppm while low detection at lower concentrations. I_3 showed a slight increase at 1000 ppm.

The detection sensitivity toward Hg^{2+} ions is illustrated in **Fig. 5.11**, I_2 displayed the highest detection sensitivity at all tested concentrations while I_1 had high detection at concentrations above 250 ppm. I_3 displayed moderate detection at lower concentration values.

The case of Pb^{2+} ions detection by I_1 - I_3 is depicted in **Fig. 5.12**. Similar to the case of Hg^{2+} , I_2 once again is the most sensitive toward all tested concentrations, while I_1 was more effective as the ions concentration was increased. I_3 had moderate detections, respectively.

5.4 Electrochemical determination of heavy metals

The analytical performance of the proposed electrochemical sensors was examined under the determined optimal conditions (0.2 M HCl, pH = 0.7), accumulation potential of -1.2 V for an accumulation time of 90 s). **Fig. 5.13** presents the overlaid square wave voltammograms (SWV) for the simultaneous electrochemical determination of heavy metals (HMs) in the concentration range from 1 to 100 ppb based on the I_1 - I_3 @Screen printed electrodes (SPEs), whereas the corresponding calibration curves are displayed as inserts.

The peak separation in the SWV signals is large to quantify each metal ion distinctly. On the voltammograms of I_1 @SPE and I_2 @SPE, some peaks appeared apart from those corresponding to the heavy metals, owing either to non-complexed analytes trapped on the modified SPEs surfaces (electroactive impurities formerly present in the electrolytic solution) or due to the resorcinarenes' leaching.

Based on the constructed calibration curves (**Fig. 5.13**), a perfect linear relationship between the concentrations of heavy metals and the responses in peak currents was established (see correlation coefficients in **Table 5.3**). The limits of detection (LODs) and limits of quantification (LOQs) were calculated from $\text{LOD} = 3.3\sigma/S$ and $\text{LOQ} = 10\sigma/S$, where σ is the standard deviation of the blank (based on three measurements) and S is the linear range's slope, or else the sensor's sensitivity.

The proposed sensors presented wide linear responses and noble sensitivities, the attained LODs and LOQs are much lower than the recommended thresholds stated by the WHO and the USEPA, therefore confirming the ultra-sensitivity of our sensing platforms.

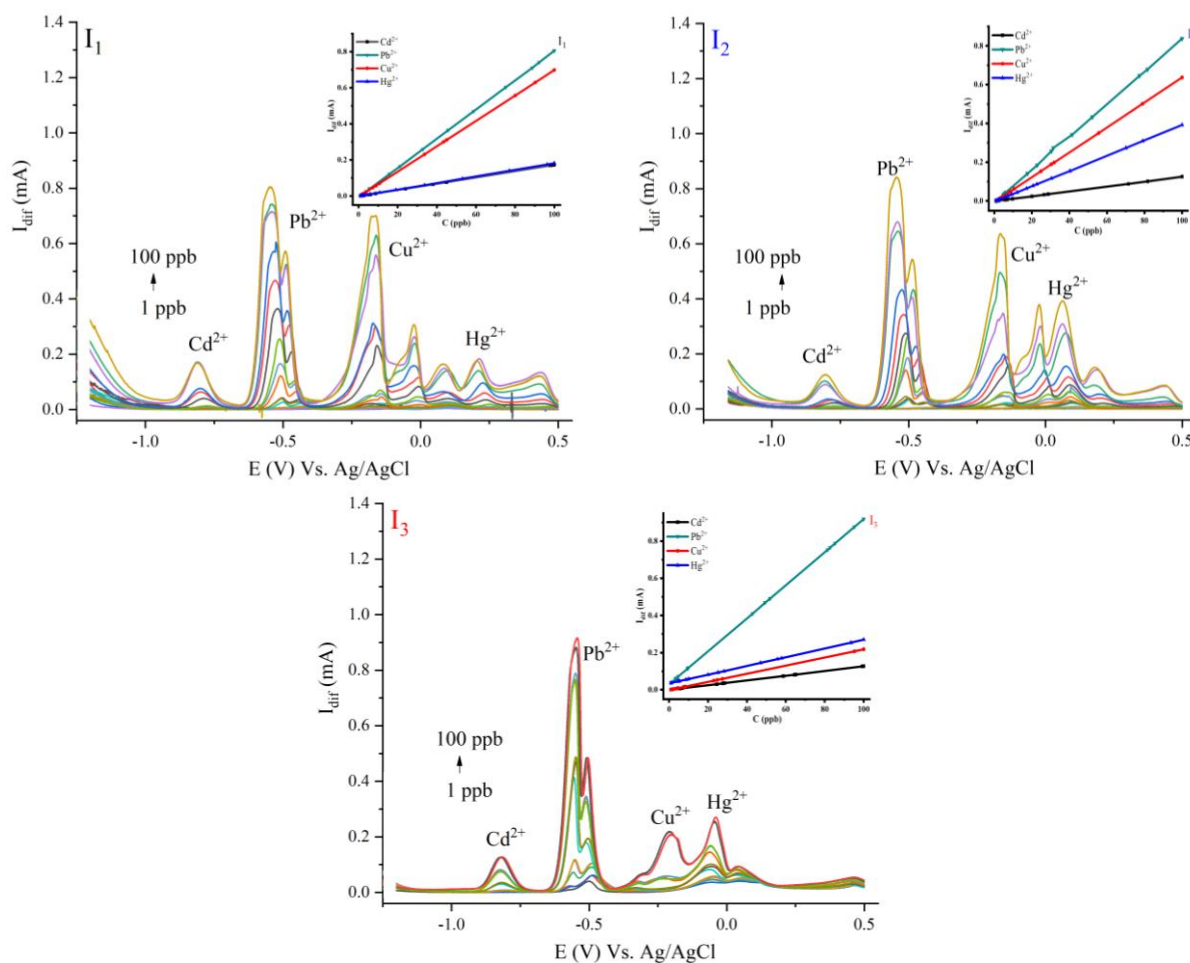


Fig. 5.13: Simultaneous electrochemical determination of the studied heavy metals in the concentration range from 1 to 100 ppb under optimal conditions based on I₁-I₃ modified SPEs, the inserts are presented for the corresponding calibration curves.

Table 5.3: Metrological parameters of the developed sensors based.

Ionophore	Ions	LR (ppb)	Fitting equation	R ²	LOD (ppb)	LOQ (ppb)
I ₁	Cd ²⁺	1-100	$I = 0.0017 * C_{Cd^{2+}} - 0.0016$	0.9999	0.37	1.11
	Pb ²⁺	1-100	$I = 0.0081 * C_{Pb^{2+}} - 0.0064$	0.9999	0.19	0.57
	Cu ²⁺	1-100	$I = 0.0070 * C_{Cu^{2+}} - 0.0049$	0.9999	0.23	0.70
	Hg ²⁺	1-100	$I = 0.0018 * C_{Hg^{2+}} - 0.0006$	0.9999	0.41	1.23
I ₂	Cd ²⁺	1-100	$I = 0.0013 * C_{Cd^{2+}} - 0.0011$	0.9999	0.39	1.17
	Pb ²⁺	1-100	$I = 0.0084 * C_{Pb^{2+}} - 0.0071$	0.9997	0.17	0.51
	Cu ²⁺	1-100	$I = 0.0064 * C_{Cu^{2+}} - 0.0061$	0.9999	0.25	0.75
	Hg ²⁺	1-100	$I = 0.0039 * C_{Hg^{2+}} - 0.0034$	0.9999	0.29	0.87
I ₃	Cd ²⁺	1-100	$I = 0.0013 * C_{Cd^{2+}} - 0.0002$	0.9999	0.38	1.14
	Pb ²⁺	1-100	$I = 0.0089 * C_{Pb^{2+}} + 0.0293$	0.9999	0.15	0.45
	Cu ²⁺	1-100	$I = 0.0022 * C_{Cu^{2+}} - 0.0013$	0.9999	0.33	0.99
	Hg ²⁺	1-100	$I = 0.0024 * C_{Hg^{2+}} + 0.0344$	0.9999	0.31	0.93

5.4.1 Interferences study

The effect of interfering ions on the heavy metals determination and the sensors' selectivity was investigated via adding metal ions frequently present in water matrices, i.e. Al^{3+} , K^+ , Mg^{2+} , Zn^{2+} , and Ni^{2+} . A 4 ppm concentration (40 folds) of each interfering ion was added to 0.2 M HCl ($\text{pH} = 0.7$) containing 100 ppb of heavy metals, **Fig. 5.14** is therefore displaying a comparison of the heavy metals peak currents for the developed sensors in the absence (control) and in the presence of interfering ions under the determined optimal conditions.

Analyzing **Fig. 5.14** and **Table 5.4**, the calculated signal deviations of 100 ppb of heavy metals are less than 5%, so the studied interfering cations did not affect the simultaneous detection of heavy metals while applying the optimized procedure, which withstands the potential employment of our sensors for the simultaneous selective determination of heavy metals.

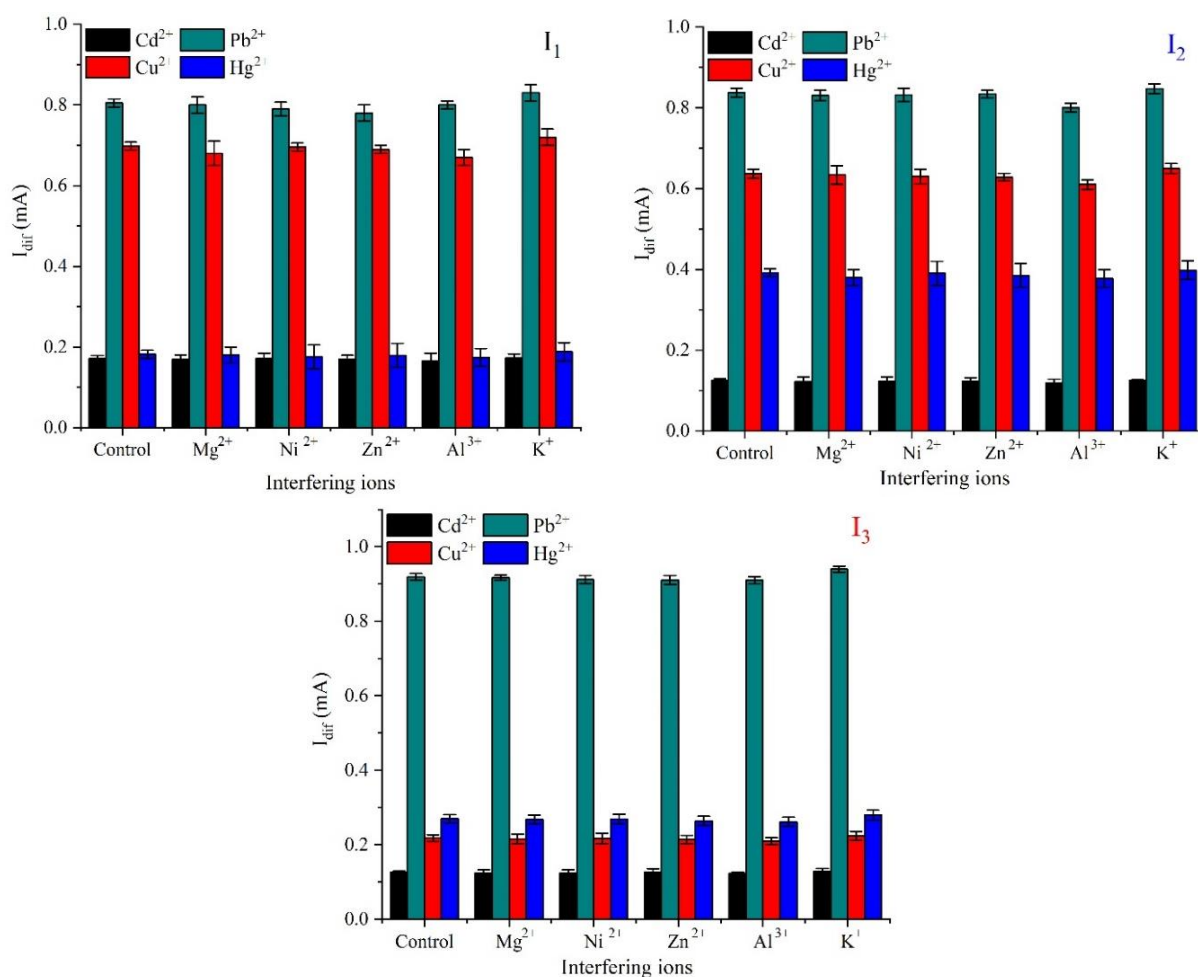


Fig. 5.14: Bar charts representing the heavy metals peak currents for the I₁-I₃@SPEs sensors in the absence (control) and the existence of interfering ions under optimal conditions.

Table 5.4: Current peak deviations for 100 ppb of HM in the presence of 40 folds' excess of interfering ions.

Ionophores	Interfering ions	Peak deviation (%) = $\left(\frac{I_{\text{control}} - I_{\text{control+interfering}}}{I_{\text{control}}} \right) \times 100$			
		Cd ²⁺	Pb ²⁺	Cu ²⁺	Hg ²⁺
I ₁	Mg ²⁺	1.17	0.62	2.57	1.10
	Ni ²⁺	0.58	1.86	0.30	3.84
	Zn ²⁺	1.17	3.10	1.15	1.64
	Al ³⁺	4.06	0.62	4.01	- 4.40
	K ⁺	- 0.60	- 3.11	- 3.15	- 3.29
I ₂	Mg ²⁺	2.40	0.95	0.47	3.06
	Ni ²⁺	1.60	0.72	1.10	0.51
	Zn ²⁺	0.80	0.47	1.26	1.78
	Al ³⁺	4.80	4.53	4.23	3.83
	K ⁺	- 0.56	- 1.07	- 2.04	- 1.53
I ₃	Mg ²⁺	1.57	0.21	0.91	0.74
	Ni ²⁺	2.36	0.76	0.45	0.37
	Zn ²⁺	0.78	0.87	1.83	2.22
	Al ³⁺	3.15	0.98	3.66	2.96
	K ⁺	- 1.96	- 2.28	- 2.75	- 3.70

5.4.2 Examination of reproducibility and repeatability

Under optimized conditions, the sensors' reproducibility has been evaluated employing three modified electrodes for each ionophore to simultaneously detect 100 ppb of heavy metals. Likewise, for the examination of repeatability, utilizing one modified electrode for each ionophore, three successive square wave voltammetric scans were performed to quantify 100 ppb of heavy metals. The outcomes in terms of residual standard deviation (RSD) are tabulated in **Table 5.5**. The RSDs did not pass 5 %, indicating excellent reproducibility and repeatability of the developed sensors, and so their potential practical utilization to determine trace levels of heavy metals simultaneously with high analytical selectivity.

Table 5.5: RSDs related to reproducibility and repeatability of the developed sensors.

Ionophore	RSD related to reproducibility				RSD related to repeatability			
	Cd ²⁺	Pb ²⁺	Cu ²⁺	Hg ²⁺	Cd ²⁺	Pb ²⁺	Cu ²⁺	Hg ²⁺
I ₁	4.68	3.93	3.64	3.24	2.19	2.56	1.44	2.18
I ₂	4.78	3.71	3.55	4.84	2.93	2.12	3.24	2.56
I ₃	3.12	4.34	4.31	4.73	3.73	2.73	2.54	3.77

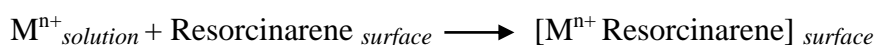
5.5 Heavy metals ions detection mechanisms

5.5.1 Piezogravimetric detection mechanism

Numerous factors must be involved in explaining the detection mechanism, for instance, the

complementarity between metal ions and resorcinarene cavity sizes, besides the molecular structure of ligands (substituents nature and number). Potential complexation interactions between sensing platforms and target ions are mainly of a non-covalent physical nature (VDW, cation- π ...etc.). Herein, we enlighten the sensing mechanism in three major steps:

- A first step manifesting in a complexation, or else host-guest interaction between the metals ions ($M^{n+} = Cd^{2+}, Cu^{2+}, Hg^{2+},$ and Pb^{2+}) and the resorcinarenes ($I_1, I_2,$ and I_3) already attached to the gold surface, either owing to an electron transfer from heteroatoms and nucleophilic elements towards heavy metals or due to their physical adsorption within the ligands' cavities, commonly these interactions are of VDW and cation- π origins:



- A second stage is the mass loading (accumulation) of metals ions on the solution-electrode interface;
- And the third phase of piezogravimetric detection thanks to the metal ions buildup on the resonator's surface.

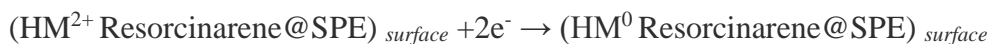
5.5.2 Electrochemical detection mechanism

The proposed sensing platforms could achieve low detection limits due to the analytical performance improvement; explained by the high complexation affinity between the heavy metals and the hydroxyl groups of the resorcinarenes plus the lone pair of electrons on the oxygen and nitrogen atoms (I_3), affording better conditions for a host-guest reaction, the suggested electrochemical mechanism can be clarified in three steps [125]:

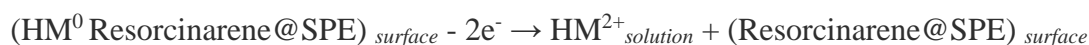
1. **Accumulation:** Physical adsorption of charged heavy metals (HMs) on the modified electrodes' surfaces (SPEs), mainly via electrostatic attractions:



2. **Preconcentration:** At a higher negative potential compared to that of the HM^{2+}/HM couples, the adsorbed HMs are electrodeposited on the modified SPEs through a cathodic reduction from a valence state of ($^{2+}$) to (0) to enhance the mass transfer rate, permitting the HMs to be deposited at the SPE surface:



3. **Stripping:** the electrodeposited HMs are turned back to the electrolytic solution through anodic oxidation, translated by an SWV analytic signal. In this step, a positive scan took place for the consistent determination of the four HMs:



C hapter 6: Conclusions & Future Recommendations

This research aimed to develop and identify effective methods and procedures to detect heavy metals ions in aqueous solutions, aiming to attain low detection limits (LODs).

- The primary phase of this dissertation research work was dedicated to the synthesis of the ionophores. Based on acid-catalyzed cyclocondensation reactions, a series of resorcinarene molecules including C-dec-9-enylcalix[4]resorcinarene (I₁) and C-undecylcalix[4]resorcinarene (I₂) were produced. Derived from the (I₁), two novel compounds bearing chiral moieties were synthesized, viz. C-dec-9-enylcalix[4]resorcinarene-O-(S-)- α -methylbenzylamine (I₃), and its enantiomer C-dec-9-enylcalix[4]resorcinarene-O-(R+)- α -methylbenzylamine (I₄).
- Once the chemicals were synthesized, analytical characterization methods as ATR-FTIR, NMR, thermal analyses, and X-ray diffraction were effectively employed to define their properties. The molecular functional groups acquired from the Infra-Red spectra of (I₁-I₄), besides the aromatic and chemical shifts gained from the NMR spectra confirmed their proposed theoretical structures. The thermal analyses confirmed their thermal stability and purity. And the X-ray diffractograms revealed a semi-crystalline character for all ionophores except I₂ which was crystalline, the heat flow outcomes were in decent accordance with the X-ray diffraction results.
- The complexation and detection abilities of heavy metals based on ionophores (I₁-I₃) were tested by Langmuir isotherms, quartz crystal microbalance with impedance measurements (QCM-I), and electrochemical methods. The results from the Langmuir ultra-thin monolayers of ionophores (I₁-I₃) at the water/air interface showed their capability of interacting with the studied ions (Cd²⁺, Cu²⁺, Hg²⁺, and Pb²⁺), where decent encapsulation characteristics were revealed along with ionic selectivity.
- Based on ionophores (I₁-I₃), detection platforms were fabricated on the gold sensing area of the quartz crystals (QCs) and screen printed electrodes (SPEs), for the detection of heavy metals in aqueous solutions via QCM-I and electrochemistry: Considering QCM-I, cleaned QCs were modified using (I₁-I₃) and were employed as detection platforms via monitoring the frequency, the dissipation, and the full width at half maximum (FWHM) shifts. The piezogravimetric sensors successfully detected the heavy metals and detection limits in the

ppm/ppb level were attained. The lowest LODs were associated with Cu^{2+} for I_1 (10.00 ppb), Pb^{2+} ions for I_2 (0.48 ppm), and I_3 (0.45 ppm). The selectivity evaluation based on frequency shifts indicated that I_1 is selective to Hg^{2+} and Cd^{2+} , I_2 to Cu^{2+} and Pb^{2+} , whereas (I_3) was selective to Hg^{2+} and Cd^{2+} .

- Novel voltammetric sensors were prepared by modifying the gold SPEs with ionophores (I_1 - I_3), the sensors were electrochemically characterized employing cyclic voltammetry (CV), square wave voltammetry (SWV), and electrochemical impedance spectroscopy (EIS), which showed the success of the electrode modification. After optimizing the experimental conditions (supporting electrolyte, pH, accumulation time, and accumulation potential), the sensors simultaneously detected heavy metals via SWV studies, and decent sensing characteristics were achieved, reaching detection limits in the ppb level, the lowest LODs were associated to Pb^{2+} and were as follow: $\text{I}_1 = 0.19$ ppb, $\text{I}_2 = 0.17$ ppb, $\text{I}_3 = 0.15$ ppb. The selectivity evaluation of the sensors was performed by studying the effect of interfering ions majorly present in water sources (Mg^{2+} , Ni^{2+} , Zn^{2+} , Al^{3+} , and K^+) on the SWV signals. The interfering ions did not affect the simultaneous detection of heavy metals ($\text{RSD} < 5\%$), and the sensors presented excellent repeatability and reproducibility ($\text{RSD} < 5\%$).

In summary, this dissertation has presented a new approach toward the environmental procedures for the detection of heavy metals ions in water. We have evaluated the chemical and physical properties of the investigated chemicals as detecting elements for hazardous cations. The resultant notions from these analyses lead to new concerns that can be taken into consideration in the *future works of this assignment*, and we trust that more evolvment can be made by:

- Suggesting new immobilization approaches for the ionophores on the gold surface.
- Applying gold nanoparticles in synergetic effect with the ionophores to amplify the frequency signal for the QCM analysis aiming to detect the heavy metals at a ppb level.
- Overcoming the selectivity limitations concerning the QCM analysis, and studying the effect of interfering ions.
- Elaborating the possibility of using computational calculations and simulations to understand the mechanisms of the detection process.
- Exploring the sensing abilities of the produced ionophores in the gas phase aiming to detect toxic gases.

This in turn leads to broad practical impact for facilitating environmental protection and avoiding extremely toxic contaminants in water.

N

ew scientific results

My thesis work was dedicated to the development and application of resorcinarene based ionophores as novel piezogravimetric and electrochemical chemosensing platforms, aiming at detecting heavy metals ions in aqueous solutions. In conformity with the established results and published papers, the following thesis points are concluded:

Point 1. A series of Calix[4]resorcinarene oligomers (I₁-I₄), comprising two novel ionophores (I₃, I₄) bearing chiral moieties, were effectively synthesized based on acid-catalyzed cyclo-condensation reactions.

After synthesis of the oligomers, I performed characterization of the oligomers using FTIR, ¹H NMR, and ¹³C NMR, TG-DSC-MS, and PXRD, to confirm their structures, thermal stability, purity, and crystalline behavior. Undeniably, an agreement between crystallinity degree and DSC outcomes (melting endotherms' shapes) was prominent. [publications: 1,4]

Point 2. I verified the synthesized oligomers' complexation capability and binding preferences towards HM cations (Cd²⁺, Cu²⁺, Hg²⁺, and Pb²⁺) present in the subphase by the Langmuir Π-A isotherms method.

Based on the limiting area variations acquired from the Langmuir isotherms, the ionophores showed ionic selectivity as follows: (I₁)-Pb²⁺, (I₁)-Hg²⁺, (I₂)-Cu²⁺, (I₂)-Hg²⁺, (I₃)-Cd²⁺, (I₃)-Pb²⁺. And, the interfacial interaction mechanism is described as a prospective orientation of (I₁-I₃) manifesting in a cone conformation at the interface level, supported by hydrogen bindings between the subphase-water molecules containing the heavy metals and the resorcinols' hydroxyl (I₁-I₃) and amine groups (I₃), other substituents as alkene and alkane chains are hydrophobic and supposed to front the air, while the ionophores' common ring is parallel to the water-air interface. [publications: 3,5]

Point 3. I successfully applied the newly developed QCM-I with the impedance measurement analyses (FWHM deviation) by fabricating mass-sensitive resorcinarene (I₁-I₃) chemosensors for detecting Cd²⁺, Cu²⁺, Hg²⁺, and Pb²⁺ ions in aqueous solutions.

The piezogravimetric sensors successfully detected the heavy metals and detection limits in the ppm/ppb level were attained. The fabricated sensors displayed high sensing characteristics (Wide linear ranges, high sensitivities, low detection, and quantification limits). Based on FWHM shifts, the ionic selectivity was noticeable: (I₁)-Cd²⁺, (I₁)-Hg²⁺, (I₂)-Cu²⁺, (I₂)-Pb²⁺, (I₃)-Cd²⁺, (I₃)-Hg²⁺. [publications: 4, 5, 6, 7]

Point 4. I assembled the Electrochemical sensing platforms based on (I₁-I₃) chemosensors and simultaneously detected heavy metals ions via SWV under optimized conditions, where decent detection characteristics (detection limits, sensitivity, selectivity, repeatability, and reproducibility) were achieved.

Based on (I₁-I₃) sensors, decent sensing characteristics were achieved, reaching detection limits in the ppb level, the lowest ones were associated with Pb²⁺ as follows: I₁= 0.19 ppb, I₂ = 0.17 ppb, I₃= 0.15 ppb. The sensors' selectivity evaluation was performed by studying the effect of interfering ions majorly present in water sources (Mg²⁺, Ni²⁺, Zn²⁺, Al³⁺, and K⁺) on the SWV output signals. The interfering ions did not affect the simultaneous detection of heavy metals (RSD < 5%), and the sensors presented excellent repeatability and reproducibility (RSD < 5%). [publication: 8]

L

ist of contributions

Publications in Scientific Journals

[PR-1] L. Eddaif, L. Trif, J. Telegdi, O. Egyed, and A. Shaban. *Calix[4]Resorcinarene Macrocycles: Synthesis, Thermal Behavior, and Crystalline Characterization*. **Journal of Thermal Analysis and Calorimetry** 137 (2019), 529-541. (Cited: 2, IF: 4.626, Q2)

[PR-2] L. Eddaif, A. Shaban, and J. Telegdi. *Sensitive Detection of Heavy Metals Ions Based on the Calixarene Derivatives-Modified Piezoelectric Resonators: A Review*. **International Journal of Environmental Analytical Chemistry** 99 (2019), 824-853. (Cited: 40, IF: 2.826, Q2)

[PR-3] L. Eddaif, A. Shaban, and J. Telegdi. *Application of the Langmuir Technique to Study the Response of C-dec-9-en-1-ylcalix[4]Resorcinarene and C-Undecylcalix[4]Resorcinarene Ultra-Thin Films' Interactions with Cd^{2+} , Hg^{2+} , Pb^{2+} , and Cu^{2+} Cations Present in the Subphase*. **Water, Air, & Soil Pollution** 230 (2019), 279:1–11. (Cited: 1, IF: 2.520, Q2)

[PR-4] L. Eddaif, A. Shaban, J. Telegdi, and I. Szendro. *A Piezogravimetric Sensor Platform for Sensitive Detection of Lead (II) Ions in Water Based on Calix[4]Resorcinarene Macrocycles: Synthesis, Characterization, and Detection*. **Arabian Journal of Chemistry** 13 (2020), 4448–4461. (Cited: 5, IF: 5.165, Q1)

[PR-5] L. Eddaif, A. Shaban, and I. Szendro. *Calix[4]Resorcinarene Macrocycles Interactions with Cd^{2+} , Hg^{2+} , Pb^{2+} , and Cu^{2+} Cations: A QCM- I and Langmuir Ultra- Thin Monolayers Study*. **Electroanalysis** 32 (2020), 755-766. (Cited: 2, IF: 3.223, Q2)

[PR-6] A. Shaban and L. Eddaif. *Comparative Study of a Sensing Platform via Functionalized Calix[4]resorcinarene Ionophores on QCM Resonator as Sensing Materials for Detection of Heavy Metal Ions in Aqueous Environments*. **Electroanalysis** (2021). (Cited: 1, IF: 3.223, Q2)

[PR-7] L. Eddaif and A. Shaban. *In situ QCM-I study on the applications of macrocyclic resorcinarene tetramers in chemically modified sensors platforms used to detect heavy metals ions in aqueous media*. *Under preparation*

[PR-8] L. Eddaif and A. Shaban. *Simultaneous detection of Cd^{2+} , Cu^{2+} , Hg^{2+} , and Pb^{2+} in water based on resorcinarene electrochemical sensors*. *Under preparation*

[PR-9] L. Eddaif and A. Shaban. *Nanostructured, Biological and Macrocyclic Sensing Platforms Applied to Monitoring Heavy Metals Ions in Water Sources: A Review*. *Under preparation*.

Extended Abstracts in Conference proceedings

[CR-1] **L. Eddaif** and A. Shaban. *Calix[4]resorcinarene Ionophores: A Heavy Metals Ions Detection Application. Proceedings of the 7th International Joint Conference on Environmental and Light Industry Technologies* (2019), 315-321;

[CR-2] **L. Eddaif**, A. Shaban, and J. Telegdi. *Application of Calixresorcinarenes as Chemical Sensors. Proceedings of the 1st Coatings and Interfaces Web Conference (CIWC 2019)* 1 (2019), 1-10.

[CR-3] **L. Eddaif**, A. Shaban, and J. Telegdi. *Calix[4]resorcinarene and Calix[4]arene Macrocycles: An Application for Heavy Metal Ions Detection in Aqueous Solutions, Matrafured International Meeting on Chemical Sensors* (2019).

Oral presentations

[OP-1] **L. Eddaif** and A. Shaban. *Calix[4]resorcinarene Ionophores: A Heavy Metals Ions Detection Application. The 7th International Joint Conference on Environmental and Light Industry Technologies*, Budapest, Hungary 2019;

[OP-2] **L. Eddaif**, A. Shaban, and J. Telegdi. *Calix[4]resorcinarene and Calix[4]arene Ionophores: A Heavy Metals Ions Detection Application. TTK AKI Seminar, RCNS, Budapest, Hungary* 2019;

[OP-3] **L. Eddaif**, A. Shaban, and J. Telegdi. *Application of Calixresorcinarenes as Chemical Sensors. The 1st Coatings and Interfaces Web Conference (CIWC 2019)*, Florence, Italy 2019.

Book chapters

[CH-1] **L. Eddaif** and A. Shaban. (2021). Fundamentals of Sensor Technology, In *Advances in Sensing Technology- Fundamental Aspects*, Z. Altintas and A. Barhoum (edits), Elsevier, Electronic ISBN: 9780323884327. **Accepted.**

[CH-2] A. Shaban, **L. Eddaif**, and J. Telegdi. Sensors as useful tools for water and wastewater monitoring, In: *Advances in Sensing Technology- Environmental applications*. (2021). Z. Altintas and A. Barhoum (edits), Elsevier, Electronic ISBN: 978-0-323-90223-6. **Accepted.**

The scientific impact of the Ph.D. work

The publications and citations metrics related to the Ph.D. work are recapitulated in the following Table:

Ph.D. work-related publications	8
Ph.D. work-related cumulative impact factor	21.583
Ph.D. work-related citations	51, as of 2021-11-19

R

ferences

- [1] WHO, ed., Guidelines for drinking-water quality, 4. ed, World Health Organization, Geneva, 2011.
- [2] S.-R. Lim, J.M. Schoenung, Human health and ecological toxicity potentials due to heavy metal content in waste electronic devices with flat panel displays, *J. Hazard. Mater.* 177 (2010) 251–259. <https://doi.org/10.1016/j.jhazmat.2009.12.025>.
- [3] M. Stewart, N.R. Phillips, G. Olsen, C.W. Hickey, G. Tipa, Organochlorines and heavy metals in wild-caught food as a potential human health risk to the indigenous Māori population of South Canterbury, New Zealand, *Sci. Total Environ.* 409 (2011) 2029–2039. <https://doi.org/10.1016/j.scitotenv.2011.02.028>.
- [4] M.N. Hughes, R.K. Poole, Metal speciation and microbial growth--the hard (and soft) facts, *J. Gen. Microbiol.* 137 (1991) 725–734. <https://doi.org/10.1099/00221287-137-4-725>.
- [5] E. Merian, ed., Metals and their compounds in the environment: occurrence, analysis, and biological relevance, VCH, Weinheim, 1991.
- [6] C. White, J.A. Sayer, G.M. Gadd, Microbial solubilization and immobilization of toxic metals: key biogeochemical processes for treatment of contamination, *FEMS Microbiol. Rev.* 20 (1997) 503–516.
- [7] E. Hodgson, *Reviews in environmental toxicology.* 3 3, Elsevier, Amstersdam; New York; Oxford, 1987.
- [8] S. Caroli, G. Forte, A.L. Iamiceli, B. Galoppi, Determination of essential and potentially toxic trace elements in honey by inductively coupled plasma-based techniques, *Talanta.* 50 (1999) 327–336.
- [9] I.M.M. Kenawy, M.A.H. Hafez, M.A. Akl, R.R. Lashein, Determination by AAS of some trace heavy metal ions in some natural and biological samples after their preconcentration using newly chemically modified chloromethylated polystyrene-PAN ion-exchanger, *Anal. Sci.* 16 (2000) 493–500.
- [10] E.L. Silva, P. dos S. Roldan, M.F. Giné, Simultaneous preconcentration of copper, zinc, cadmium, and nickel in water samples by cloud point extraction using 4-(2-pyridylazo)-resorcinol and their determination by inductively coupled plasma optic emission spectrometry, *J. Hazard. Mater.* 171 (2009) 1133–1138. <https://doi.org/10.1016/j.jhazmat.2009.06.127>.
- [11] A.A. Elouzi, A.A. Akasha, A.M. Elgerbi, M. El-Baseir, B.A. El Gammudi, *Journal of Chemical and Pharmaceutical Research*, 2012, 4 (9): 4337-4341, *J. Chem. Pharm. Res.* 4 (2012) 4337–4341.
- [12] İ. Narin, M. Soylak, L. Elçi, M. Doğan, Determination of trace metal ions by AAS in natural water samples after preconcentration of pyrocatechol violet complexes on an activated carbon column, *Talanta.* 52 (2000) 1041–1046.
- [13] D. Prabhakaran, M. Yuehong, H. Nanjo, H. Matsunaga, Naked-eye cadmium sensor: using chromoionophore arrays of Langmuir- Blodgett molecular assemblies, *Anal. Chem.* 79 (2007) 4056–4065.
- [14] D. Melamed, *Monitoring arsenic in the environment: a review of science and technologies for field measurements and sensors*, US Environ. Prot. Agency Wash. US EPA. (2004).
- [15] D. Sanchez-Rodas, W.T. Corns, B. Chen, P.B. Stockwell, Atomic fluorescence spectrometry: a suitable detection technique in speciation studies for arsenic, selenium, antimony and mercury, *J. Anal. At. Spectrom.* 25 (2010) 933–946.
- [16] L.C. Clark, C. Lyons, Electrode systems for continuous monitoring in cardiovascular surgery, *Ann. N. Y. Acad. Sci.* 102 (1962) 29–45.
- [17] S.J. Updike, G.P. Hicks, The Enzyme Electrode, *Nature.* 214 (1967) 986.

- [18] G.G. Guilbault, J.G. Montalvo, Urea-specific enzyme electrode, *J. Am. Chem. Soc.* 91 (1969) 2164–2165. <https://doi.org/10.1021/ja01036a083>.
- [19] G.G. Guilbault, J.G. Montalvo, An Improved Urea Specific Enzyme Electrode, *Anal. Lett.* 2 (1969) 283–293. <https://doi.org/10.1080/00032716908051300>.
- [20] G. Asch, Les capteurs en instrumentation industrielle, 2017. <http://sbiproxy.uqac.ca/login?url=http://international.scholarvox.com/book/88852384> (accessed October 25, 2018).
- [21] H. Imen, Etudes physico-chimique de capteurs à base de nanomatériaux pour des applications biomédicales, (2009) 198.
- [22] P. Bühlmann, E. Pretsch, E. Bakker, Carrier-Based Ion-Selective Electrodes and Bulk Optodes. 2. Ionophores for Potentiometric and Optical Sensors, *Chem. Rev.* 98 (1998) 1593–1688. <https://doi.org/10.1021/cr970113+>.
- [23] E. Bakker, P. Bühlmann, E. Pretsch, Carrier-Based Ion-Selective Electrodes and Bulk Optodes. 1. General Characteristics, *Chem. Rev.* 97 (1997) 3083–3132. <https://doi.org/10.1021/cr940394a>.
- [24] A.J. Bard, L.R. Faulkner, *Electrochemical methods: fundamentals and applications*, 2. ed, Wiley, Hoboken, NJ, 2001.
- [25] S.J. Rupitsch, *Piezoelectric Sensors and Actuators: Fundamentals and Applications*, Springer Berlin Heidelberg, Berlin, Heidelberg, 2019. <https://doi.org/10.1007/978-3-662-57534-5>.
- [26] S.K. Vashist, P. Vashist, Recent Advances in Quartz Crystal Microbalance-Based Sensors, *J. Sens.* 2011 (2011) 1–13. <https://doi.org/10.1155/2011/571405>.
- [27] S. Mutlu, D. Çökeliler, A. Shard, H. Goktas, B. Ozansoy, M. Mutlu, Preparation and characterization of ethylenediamine and cysteamine plasma polymerized films on piezoelectric quartz crystal surfaces for a biosensor, *Thin Solid Films.* 516 (2008) 1249–1255. <https://doi.org/10.1016/j.tsf.2007.06.074>.
- [28] G. Sauerbrey, Verwendung von Schwingquarzen zur Wugung dünner Schichten und zur Mikrowugung, *Z. Phys.* 155 (1959) 206–222. <https://doi.org/10.1007/BF01337937>.
- [29] G. Mészáros, S. Akbarzadeh, B. De La Franier, Z. Keresztes, M. Thompson, Advances in Electromagnetic Piezoelectric Acoustic Sensor Technology for Biosensor-Based Detection, *Chemosensors.* 9 (2021) 58. <https://doi.org/10.3390/chemosensors9030058>.
- [30] L. Románszki, Z. Varga, J. Mihály, Z. Keresztes, M. Thompson, Electromagnetic Piezoelectric Acoustic Sensor Detection of Extracellular Vesicles through Interaction with Detached Vesicle Proteins, *Biosensors.* 10 (2020) 173. <https://doi.org/10.3390/bios10110173>.
- [31] R.W. Murray, A.G. Ewing, R.A. Durst, Chemically modified electrodes. Molecular design for electroanalysis, *Anal. Chem.* 59 (1987) 379A–390A. <https://doi.org/10.1021/ac00132a001>.
- [32] M.A.T. Gilmartin, J.P. Hart, Sensing with chemically and biologically modified carbon electrodes. A review, *Analyst.* 120 (1995) 1029–1045. <https://doi.org/10.1039/AN9952001029>.
- [33] J.A. Cox, M.E. Tess, T.E. Cummings, Electroanalytical methods based on modified electrodes: a review of recent advances, *Rev. Anal. Chem.* 15 (2011) 173–224. <https://doi.org/10.1515/REVAC.1996.15.3.173>.
- [34] R.W. Murray, Nanoelectrochemistry: Metal Nanoparticles, Nanoelectrodes, and Nanopores, *Chem. Rev.* 108 (2008) 2688–2720. <https://doi.org/10.1021/cr068077e>.
- [35] Y.-W. Lin, C.-C. Huang, H.-T. Chang, Gold nanoparticle probes for the detection of mercury, lead and copper ions, *Analyst.* 136 (2011) 863–871. <https://doi.org/10.1039/C0AN00652A>.
- [36] Y. Liu, G. Su, B. Zhang, G. Jiang, B. Yan, Nanoparticle-based strategies for detection and remediation of environmental pollutants, *Analyst.* 136 (2011) 872–877. <https://doi.org/10.1039/C0AN00905A>.
- [37] W.-W. Li, F.-Y. Kong, J.-Y. Wang, Z.-D. Chen, H.-L. Fang, W. Wang, Facile one-pot and rapid synthesis of surfactant-free Au-reduced graphene oxide nanocomposite for trace arsenic (III) detection, *Electrochimica Acta.* 157 (2015) 183–190. <https://doi.org/10.1016/j.electacta.2014.12.150>.
- [38] S. Kumar, G. Bhanjana, N. Dilbaghi, R. Kumar, A. Umar, Fabrication and characterization of highly sensitive and selective arsenic sensor based on ultra-thin graphene oxide nanosheets, *Sens. Actuators B Chem.* 227 (2016) 29–34. <https://doi.org/10.1016/j.snb.2015.11.101>.

- [39] G. Zhao, Y. Si, H. Wang, G. Liu, A Portable Electrochemical Detection System based on Graphene/Ionic Liquid Modified Screen-printed Electrode for the Detection of Cadmium in Soil by Square Wave Anodic Stripping Voltammetry, *Int J Electrochem Sci.* 11 (2016) 11.
- [40] H. Xing, J. Xu, X. Zhu, X. Duan, L. Lu, W. Wang, Y. Zhang, T. Yang, Highly sensitive simultaneous determination of cadmium (II), lead (II), copper (II), and mercury (II) ions on N-doped graphene modified electrode, *J. Electroanal. Chem.* 760 (2016) 52–58. <https://doi.org/10.1016/j.jelechem.2015.11.043>.
- [41] Z. Zhang, X. Fu, K. Li, R. Liu, D. Peng, L. He, M. Wang, H. Zhang, L. Zhou, One-step fabrication of electrochemical biosensor based on DNA-modified three-dimensional reduced graphene oxide and chitosan nanocomposite for highly sensitive detection of Hg(II), *Sens. Actuators B Chem.* 225 (2016) 453–462. <https://doi.org/10.1016/j.snb.2015.11.091>.
- [42] N. Wang, M. Lin, H. Dai, H. Ma, Functionalized gold nanoparticles/reduced graphene oxide nanocomposites for ultrasensitive electrochemical sensing of mercury ions based on thymine–mercury–thymine structure, *Biosens. Bioelectron.* 79 (2016) 320–326. <https://doi.org/10.1016/j.bios.2015.12.056>.
- [43] Y. Cheng, H. Fa, W. Yin, C. Hou, D. Huo, F. Liu, Y. Zhang, C. Chen, A sensitive electrochemical sensor for lead based on gold nanoparticles/nitrogen-doped graphene composites functionalized with l-cysteine-modified electrode, *J. Solid State Electrochem.* 20 (2016) 327–335. <https://doi.org/10.1007/s10008-015-3043-0>.
- [44] K. Hamsawahini, P. Sathishkumar, R. Ahamad, A.R.M. Yusoff, PVDF–ErGO–GRC electrode: A single setup electrochemical system for separation, pre-concentration and detection of lead ions in complex aqueous samples, *Talanta.* 148 (2016) 101–107. <https://doi.org/10.1016/j.talanta.2015.10.044>.
- [45] E. Punrat, C. Maksuk, S. Chuanuwatanakul, W. Wonsawat, O. Chailapakul, Polyaniline/graphene quantum dot-modified screen-printed carbon electrode for the rapid determination of Cr(VI) using stopped-flow analysis coupled with voltammetric technique, *Talanta.* 150 (2016) 198–205. <https://doi.org/10.1016/j.talanta.2015.12.016>.
- [46] J. Chang, G. Zhou, E.R. Christensen, R. Heideman, J. Chen, Graphene-based sensors for detection of heavy metals in water: a review, *Anal. Bioanal. Chem.* 406 (2014) 3957–3975. <https://doi.org/10.1007/s00216-014-7804-x>.
- [47] J. Molina, F. Cases, L.M. Moretto, Graphene-based materials for the electrochemical determination of hazardous ions, *Anal. Chim. Acta.* 946 (2016) 9–39. <https://doi.org/10.1016/j.aca.2016.10.019>.
- [48] M.R. Saidur, A.R.A. Aziz, W.J. Basirun, Recent advances in DNA-based electrochemical biosensors for heavy metal ion detection: A review, *Biosens. Bioelectron.* 90 (2017) 125–139. <https://doi.org/10.1016/j.bios.2016.11.039>.
- [49] Y. Zhou, L. Tang, G. Zeng, C. Zhang, Y. Zhang, X. Xie, Current progress in biosensors for heavy metal ions based on DNAzymes/DNA molecules functionalized nanostructures: A review, *Sens. Actuators B Chem.* 223 (2016) 280–294. <https://doi.org/10.1016/j.snb.2015.09.090>.
- [50] S. Lee, K. Jang, C. Park, J. You, T. Kim, C. Im, J. Kang, H. Shin, C.-H. Choi, J. Park, S. Na, Ultra-sensitive in situ detection of silver ions using a quartz crystal microbalance, *New J. Chem.* 39 (2015) 8028–8034. <https://doi.org/10.1039/C5NJ00668F>.
- [51] M. Ebrahimi, J.B. Raoof, R. Ojani, Novel electrochemical DNA hybridization biosensors for selective determination of silver ions, *Talanta.* 144 (2015) 619–626. <https://doi.org/10.1016/j.talanta.2015.07.020>.
- [52] Y. Yang, M. Kang, S. Fang, M. Wang, L. He, X. Feng, J. Zhao, Z. Zhang, H. Zhang, A feasible C-rich DNA electrochemical biosensor based on Fe₃O₄@3D-GO for sensitive and selective detection of Ag⁺, *J. Alloys Compd.* 652 (2015) 225–233. <https://doi.org/10.1016/j.jallcom.2015.08.229>.
- [53] Q. Chen, X. Wu, D. Wang, W. Tang, N. Li, F. Liu, Oligonucleotide-functionalized gold nanoparticles-enhanced QCM-D sensor for mercury(II) ions with high sensitivity and tunable dynamic range, *Analyst.* 136 (2011) 2572–2577. <https://doi.org/10.1039/C1AN00010A>.
- [54] Z. Chen, L. Li, X. Mu, H. Zhao, L. Guo, Electrochemical aptasensor for detection of copper based on a reagentless signal-on architecture and amplification by gold nanoparticles, *Talanta.* 85 (2011) 730–735. <https://doi.org/10.1016/j.talanta.2011.04.056>.

- [55] Y. Zhang, S. Xiao, H. Li, H. Liu, P. Pang, H. Wang, Z. Wu, W. Yang, A Pb²⁺-ion electrochemical biosensor based on single-stranded DNAzyme catalytic beacon, *Sens. Actuators B Chem.* 222 (2016) 1083–1089. <https://doi.org/10.1016/j.snb.2015.08.046>.
- [56] S. Cerminati, F.C. Soncini, S.K. Checa, A sensitive whole-cell biosensor for the simultaneous detection of a broad-spectrum of toxic heavy metal ions, *Chem. Commun.* 51 (2015) 5917–5920. <https://doi.org/10.1039/C5CC00981B>.
- [57] H. Abu-Ali, A. Nabok, T.J. Smith, Electrochemical inhibition bacterial sensor array for detection of water pollutants: artificial neural network (ANN) approach, *Anal. Bioanal. Chem.* 411 (2019) 7659–7668. <https://doi.org/10.1007/s00216-019-01853-8>.
- [58] M.A. Deshmukh, M.D. Shirsat, A. Ramanaviciene, A. Ramanavicius, Composites Based on Conducting Polymers and Carbon Nanomaterials for Heavy Metal Ion Sensing, *Crit. Rev. Anal. Chem.* 48 (2018) 293–304.
- [59] G. Fadillah, O.A. Saputra, T.A. Saleh, Trends in Polymers Functionalized Nanostructures for Analysis of Environmental Pollutants, *Trends Environ. Anal. Chem.* (2020) e00084. <https://doi.org/10.1016/j.teac.2020.e00084>.
- [60] M.A. Deshmukh, M. Gicevicius, A. Ramanaviciene, M.D. Shirsat, R. Viter, A. Ramanavicius, Hybrid electrochemical/electrochromic Cu (II) ion sensor prototype based on PANI/ITO-electrode, *Sens. Actuators B Chem.* 248 (2017) 527–535.
- [61] M.A. Deshmukh, H.K. Patil, G.A. Bodkhe, M. Yasuzawa, P. Koinkar, A. Ramanaviciene, M.D. Shirsat, A. Ramanavicius, EDTA-modified PANI/SWNTs nanocomposite for differential pulse voltammetry based determination of Cu(II) ions, *Sens. Actuators B Chem.* 260 (2018) 331–338. <https://doi.org/10.1016/j.snb.2017.12.160>.
- [62] P. Wei, Z. Zhu, R. Song, Z. Li, C. Chen, An ion-imprinted sensor based on chitosan-graphene oxide composite polymer modified glassy carbon electrode for environmental sensing application, *Electrochimica Acta.* 317 (2019) 93–101. <https://doi.org/10.1016/j.electacta.2019.05.136>.
- [63] S. Di Masi, A. Garcia Cruz, F. Canfarotta, T. Cowen, P. Marote, C. Malitesta, S.A. Piletsky, Synthesis and Application of Ion-Imprinted Nanoparticles in Electrochemical Sensors for Copper (II) Determination, *ChemNanoMat.* 5 (2019) 754–760. <https://doi.org/10.1002/cnma.201900056>.
- [64] S. Di Masi, A. Pennetta, A. Guerreiro, F. Canfarotta, G.E. De Benedetto, C. Malitesta, Sensor based on electrosynthesised imprinted polymeric film for rapid and trace detection of copper(II) ions, *Sens. Actuators B Chem.* 307 (2020) 127648. <https://doi.org/10.1016/j.snb.2019.127648>.
- [65] Z. Yang, C. Zhang, Designing of MIP-based QCM sensor for the determination of Cu (II) ions in solution, *Sens. Actuators B Chem.* 142 (2009) 210–215.
- [66] R. Seenivasan, W.-J. Chang, S. Gunasekaran, Highly Sensitive Detection and Removal of Lead Ions in Water Using Cysteine-Functionalized Graphene Oxide/Polypyrrole Nanocomposite Film Electrode, *ACS Appl. Mater. Interfaces.* 7 (2015) 15935–15943. <https://doi.org/10.1021/acsami.5b03904>.
- [67] L. Sartore, M. Barbaglio, L. Borgese, E. Bontempi, Polymer-grafted QCM chemical sensor and application to heavy metal ions real time detection, *Sens. Actuators B Chem.* 155 (2011) 538–544. <https://doi.org/10.1016/j.snb.2011.01.003>.
- [68] C.J. Pedersen, Cyclic polyethers and their complexes with metal salts, *J. Am. Chem. Soc.* 89 (1967) 7017–7036. <https://doi.org/10.1021/ja01002a035>.
- [69] H. Luo, L.-X. Chen, Q.-M. Ge, M. Liu, Z. Tao, Y.-H. Zhou, H. Cong, Applications of macrocyclic compounds for electrochemical sensors to improve selectivity and sensitivity, *J. Incl. Phenom. Macrocycl. Chem.* 95 (2019) 171–198. <https://doi.org/10.1007/s10847-019-00934-6>.
- [70] Z.M. Kadam, Polymer Membranes based on Ionophore-impregnated for Nutrients Detection by Electrochemical Methods, (2017) 5.
- [71] S. Kumbhat, U. Singh, A potassium-selective electrochemical sensor based on crown-ether functionalized self assembled monolayer, *J. Electroanal. Chem.* 809 (2018) 31–35. <https://doi.org/10.1016/j.jelechem.2017.12.051>.
- [72] U. Singh, S. Kumbhat, Functionalized surface for electrochemical sensing of electrochemically inactive alkali metal ion, *INDIAN J CHEM.* (2017) 5.

- [73] F. Karimian, G.H. Rounaghi, M.H. Arbab-Zavar, Construction of a PVC based 15-crown-5 electrochemical sensor for Ag(I) cation, *Chin. Chem. Lett.* 25 (2014) 809–814. <https://doi.org/10.1016/j.ccllet.2014.03.014>.
- [74] M. Ghanei-Motlagh, Ch. Karami, M.A. Taher, S.J. Hosseini-Nasab, Stripping voltammetric detection of copper ions using carbon paste electrode modified with aza-crown ether capped gold nanoparticles and reduced graphene oxide, *RSC Adv.* 6 (2016) 89167–89175. <https://doi.org/10.1039/C6RA10267K>.
- [75] E. Flores, J. Pizarro, F. Godoy, R. Segura, A. Gómez, N. Agurto, P. Sepúlveda, An electrochemical sensor for the determination of Cu(II) using a modified electrode with ferrocenyl crown ether compound by square wave anodic stripping voltammetry, *Sens. Actuators B Chem.* 251 (2017) 433–439. <https://doi.org/10.1016/j.snb.2017.05.058>.
- [76] M. Dagdevren, I. Yilmaz, B. Yucel, M. Emirik, A Novel Ferrocenyl Naphthoquinone Fused Crown Ether as a Multisensor for Water Determination in Acetonitrile and Selective Cation Binding, *J. Phys. Chem. B.* 119 (2015) 12464–12479. <https://doi.org/10.1021/acs.jpcc.5b06590>.
- [77] S. Dehdashtian, M. Shamsipur, Modification of gold surface by electrosynthesized mono aza crown ether substituted catechol-terminated alkane dithiol and its application as a new electrochemical sensor for trace detection of cadmium ions, *Colloids Surf. B Biointerfaces.* 171 (2018) 494–500. <https://doi.org/10.1016/j.colsurfb.2018.07.063>.
- [78] A. Villiers, Sur la transformation de la fécule en dextrine par le ferment butyrique, (1891).
- [79] X. Niu, Z. Mo, X. Yang, M. Sun, P. Zhao, Z. Li, M. Ouyang, Z. Liu, H. Gao, R. Guo, N. Liu, Advances in the use of functional composites of β -cyclodextrin in electrochemical sensors, *Microchim. Acta.* 185 (2018) 328. <https://doi.org/10.1007/s00604-018-2859-6>.
- [80] G. Zhu, Y. Yi, J. Chen, Recent advances for cyclodextrin-based materials in electrochemical sensing, *TrAC Trends Anal. Chem.* 80 (2016) 232–241. <https://doi.org/10.1016/j.trac.2016.03.022>.
- [81] K.N. Rajput, K.C. Patel, U.B. Trivedi, β -Cyclodextrin Production by Cyclodextrin Glucanotransferase from an Alkaliphile Microbacterium terrae KNR 9 Using Different Starch Substrates, *Biotechnol. Res. Int.* 2016 (2016). <https://doi.org/10.1155/2016/2034359>.
- [82] S. Teka, A. Gaied, N. Jaballah, S. Xiaonan, M. Majdoub, Thin sensing layer based on semi-conducting β -cyclodextrin rotaxane for toxic metals detection, *Mater. Res. Bull.* 74 (2016) 248–257. <https://doi.org/10.1016/j.materresbull.2015.10.040>.
- [83] S. Çubuk, Ö. Yılmaz, E. Kök Yetimoğlu, M.V. Kahraman, Determination of Cd(II) Ions by using Cyclodextrin Based Polymeric Fluorescence Sensor, *J. Turk. Chem. Soc. Sect. Chem.* (2017) 61–61. <https://doi.org/10.18596/jotcsa.292001>.
- [84] A.U. Alam, M.M.R. Howlader, N.-X. Hu, M.J. Deen, Electrochemical sensing of lead in drinking water using β -cyclodextrin-modified MWCNTs, *Sens. Actuators B Chem.* 296 (2019) 126632. <https://doi.org/10.1016/j.snb.2019.126632>.
- [85] S. Huang, S. Lu, C. Huang, J. Sheng, W. Su, L. Zhang, Q. Xiao, Sensitive and selective stripping voltammetric determination of copper(II) using a glassy carbon electrode modified with amino-reduced graphene oxide and β -cyclodextrin, *Microchim. Acta.* 182 (2015) 2529–2539. <https://doi.org/10.1007/s00604-015-1627-0>.
- [86] M. Lv, X. Wang, J. Li, X. Yang, C. Zhang, J. Yang, H. Hu, Cyclodextrin-reduced graphene oxide hybrid nanosheets for the simultaneous determination of lead(II) and cadmium(II) using square wave anodic stripping voltammetry, *Electrochimica Acta.* 108 (2013) 412–420. <https://doi.org/10.1016/j.electacta.2013.06.099>.
- [87] A.U. Alam, Y. Qin, M.M.R. Howlader, N.-X. Hu, M.J. Deen, Electrochemical sensing of acetaminophen using multi-walled carbon nanotube and β -cyclodextrin, *Sens. Actuators B Chem.* 254 (2018) 896–909. <https://doi.org/10.1016/j.snb.2017.07.127>.
- [88] A.U. Alam, Y. Qin, M. Catalano, L. Wang, M.J. Kim, M.M.R. Howlader, N.-X. Hu, M.J. Deen, Tailoring MWCNTs and β -Cyclodextrin for Sensitive Detection of Acetaminophen and Estrogen, *ACS Appl. Mater. Interfaces.* 10 (2018) 21411–21427. <https://doi.org/10.1021/acsami.8b04639>.
- [89] A. Zinke, E. Ziegler, Zur Kenntnis des Härtungsprozesses von Phenol-Formaldehyd-Harzen, X. Mitteilung, *Berichte Dtsch. Chem. Ges. B Ser.* 77 (1944) 264–272. <https://doi.org/10.1002/cber.19440770322>.

- [90] B.T. Hayes, R.F. Hunter, Phenol-formaldehyde and allied resins VI: Rational synthesis of a 'cyclic' tetranuclear p-cresol novolak, *J. Appl. Chem.* 8 (1958) 743–748. <https://doi.org/10.1002/jctb.5010081107>.
- [91] N.L.R. Megson, historical review after a lecture given in Graz, Oct. 9, 1952, *Oesterreichische Chemie Zeitschrift.* 54 (1953) 317.
- [92] T. Kappe, The Early History of Calixarene Chemistry. In: Vicens J., Asfari Z., Harrowfield J.M. (eds) *Calixarenes 50th Anniversary: Commemorative Issue*. Springer, Dordrecht (1994). https://doi.org/10.1007/978-94-011-0267-4_1.
- [93] J.W. Cornforth, P.D. Hart, G.A. Nicholls, R.J.W. Rees, J.A. Stock, Antituberculous Effects of Certain Surface-Active Polyoxyethylene Ethers, *Br. J. Pharmacol. Chemother.* 10 (1955) 73–86. <https://doi.org/10.1111/j.1476-5381.1955.tb00063.x>.
- [94] C.D. Gutsche, *Calixarenes: An Introduction*, 2008. <https://doi.org/10.1039/9781847558190>.
- [95] C.D. Gutsche, R. Muthukrishnan, Calixarenes. 1. Analysis of the product mixtures produced by the base-catalyzed condensation of formaldehyde with para-substituted phenols, *J. Org. Chem.* 43 (1978) 4905–4906. <https://doi.org/10.1021/jo00419a052>.
- [96] A. Arduini, A. Pochini, S. Raverberi, R. Ungaro, p-t-Butyl-calix[4]arene tetracarboxylic acid. A water soluble calixarene in a cone structure, *J. Chem. Soc. Chem. Commun.* (1984) 981–982. <https://doi.org/10.1039/C39840000981>.
- [97] H. Kämmerer, G. Happel, F. Caesar, Die spektroskopische untersuchung einer cyclischen, tetrameren verbindung aus p-kresol und formaldehyd, *Makromol. Chem.* 162 (1972) 179–197. <https://doi.org/10.1002/macp.1972.021620116>.
- [98] E.U. Thoden van Velzen, J.F.J. Engbersen, P.J. de Lange, J.W.G. Mahy, D.N. Reinhoudt, Self-Assembled Monolayers of Resorcin[4]arene Tetrasulfides on Gold, *J. Am. Chem. Soc.* 117 (1995) 6853–6862. <https://doi.org/10.1021/ja00131a007>.
- [99] J. Vicens, V. Böhmer, eds., *Calixarenes: A Versatile Class of Macrocyclic Compounds*, Springer Netherlands, 1991. <https://doi.org/10.1007/978-94-009-2013-2>.
- [100] D.R. Stewart, C.D. Gutsche, Isolation, Characterization, and Conformational Characteristics of p-tert-Butylcalix[9–20]arenes1, *J. Am. Chem. Soc.* 121 (1999) 4136–4146. <https://doi.org/10.1021/ja983964n>.
- [101] J. Vicens, J. Harrowfield, eds., *Calixarenes in the Nanoworld*, Springer Netherlands, 2007. <https://doi.org/10.1007/978-1-4020-5022-4>.
- [102] G. Uysal Akku, E. Al, S.E. Korcan, Selective extraction of toxic heavy metals and biological activity studies using pyrimidylthioamide functionalised calix[4]arene, *Supramol. Chem.* 27 (2015) 522–526. <https://doi.org/10.1080/10610278.2015.1020944>.
- [103] X. Lu, D. Zhang, S. He, J. Feng, A. Tesfay Reda, C. Liu, Z. Yang, L. Shi, J. Li, Reactive extraction of europium(III) and neodymium(III) by carboxylic acid modified calixarene derivatives: Equilibrium, thermodynamics and kinetics, *Sep. Purif. Technol.* 188 (2017) 250–259. <https://doi.org/10.1016/j.seppur.2017.07.040>.
- [104] M. Moradi, L.G. Tulli, J. Nowakowski, M. Baljovic, T.A. Jung, P. Shahgaldian, Two-Dimensional Calix[4]arene-based Metal-Organic Coordination Networks of Tunable Crystallinity, *Angew. Chem. Int. Ed.* 56 (2017) 14395–14399. <https://doi.org/10.1002/anie.201703825>.
- [105] C. Sgarlata, G. Brancatelli, C.G. Fortuna, D. Sciotto, S. Geremia, C. Bonaccorso, Three-Dimensional Network Structures Based on Pyridyl-Calix[4]Arene Metal Complexes, *ChemPlusChem.* 82 (2017) 1341–1350. <https://doi.org/10.1002/cplu.201700400>.
- [106] I.V. Smirnov, E.S. Stepanova, N.M. Ivenskaya, M.D. Karavan, S.R. Zaripov, S.R. Kleshnina, S.E. Solovieva, I.S. Antipin, Cesium and americium extraction from carbonate-alkaline media with O-substituted p-alkylcalix[8]arenes, *J. Radioanal. Nucl. Chem.* 314 (2017) 1257–1265. <https://doi.org/10.1007/s10967-017-5505-6>.
- [107] A.N. Kumar, J. Ramkuma, S. Chandramouleeswaran, S.K. Nayak, One-step synthesis of a singly bridged biscalic[6]arene and evaluation of its alkali metal recognition properties, *Org. Commun.* 10 (2017) 304–313. <https://doi.org/10.25135/acg.oc.28.17.06.029>.

- [108] G. Horvat, L. Frkanec, N. Cindro, V. Tomišić, A comprehensive study of the complexation of alkali metal cations by lower rim calix[4]arene amide derivatives, *Phys. Chem. Chem. Phys.* 19 (2017) 24316–24329. <https://doi.org/10.1039/C7CP03920D>.
- [109] G. De Leener, D. Over, C. Smet, D. Cornut, A.G. Porras-Gutierrez, I. López, B. Douziech, N. Le Poul, F. Topić, K. Rissanen, Y. Le Mest, I. Jabin, O. Reinaud, “Two-Story” Calix[6]arene-Based Zinc and Copper Complexes: Structure, Properties, and O₂ Binding, *Inorg. Chem.* 56 (2017) 10971–10983. <https://doi.org/10.1021/acs.inorgchem.7b01225>.
- [110] S. Sayin, M.S. Engin, S. Eymur, S. Çay, Synthesis and Characterization of 1-(2-Furoyl) Piperazine Calix[4]arene for the Preconcentration of Metal Ions, *Anal. Lett.* 51 (2018) 111–118. <https://doi.org/10.1080/00032719.2016.1265533>.
- [111] D. Diamond, Neutral carrier based ion-selective electrodes, in: *Anal. Chem. Symp. Ser.*, 1986: p. 155.
- [112] D. Diamond, G. Svehla, E.M. Seward, M.A. McKervey, A sodium ion-selective electrode based on methyl p-t-butylcalix[4]aryl acetate as the ionophore, *Anal. Chim. Acta.* 204 (1988) 223–231. [https://doi.org/10.1016/S0003-2670\(00\)86361-8](https://doi.org/10.1016/S0003-2670(00)86361-8).
- [113] A.M. Cadogan, D. Diamond, M.R. Smyth, M. Deasy, M.A. McKervey, S.J. Harris, Sodium-selective polymeric membrane electrodes based on calix[4]arene ionophores, *Analyst.* 114 (1989) 1551–1554. <https://doi.org/10.1039/AN9891401551>.
- [114] K.M. O’Connor, G. Svehla, S.J. Harris, M.A. McKervey, Calixarene-based potentiometric ion-selective electrodes for silver, *Talanta.* 39 (1992) 1549–1554. [https://doi.org/10.1016/0039-9140\(92\)80140-9](https://doi.org/10.1016/0039-9140(92)80140-9).
- [115] K.M. O’Connor, M. Cherry, G. Svehla, S.J. Harris, M.A. McKervey, Symmetrical, unsymmetrical and bridged calix[4]arene derivatives as neutral carrier ionophores in poly (vinyl chloride) membrane sodium selective electrodes, *Talanta.* 41 (1994) 1207–1217. [https://doi.org/10.1016/0039-9140\(94\)80093-6](https://doi.org/10.1016/0039-9140(94)80093-6).
- [116] F. Cadogan, P. Kane, M.A. McKervey, D. Diamond, Lead-Selective Electrodes Based on Calixarene Phosphine Oxide Derivatives, *Anal. Chem.* 71 (1999) 5544–5550. <https://doi.org/10.1021/ac990303f>.
- [117] Y. Liu, B.-T. Zhao, H.-Y. Zhang, H.-F. Ju, L.-X. Chen, X.-W. He, Molecular Design of Calixarene, Part 4, Synthesis of Novel Double-Armed p-(tert-Butyl)calix[4]arene-Derived Amides and Their Lead(II)(Pb²⁺)-Selective-Electrode Properties, *Helv. Chim. Acta.* 84 (2001) 1969–1975. [https://doi.org/10.1002/1522-2675\(20010711\)84:7<1969::AID-HLCA1969>3.0.CO;2-Q](https://doi.org/10.1002/1522-2675(20010711)84:7<1969::AID-HLCA1969>3.0.CO;2-Q).
- [118] M. Hosseini, M. Rahimi, H.B. Sadeghi, S. Taghvaei-Ganjali, S.D. Abkenar, M.R. Ganjali, Determination of Hg(II) ions in water samples by a novel Hg(II) sensor, based on calix[4]arene derivative, *Int. J. Environ. Anal. Chem.* 89 (2009) 407–422. <https://doi.org/10.1080/03067310802713195>.
- [119] D.P. Nikolelis, G. Raftopoulou, N. Psaroudakis, G.-P. Nikoleli, Development of an electrochemical chemosensor for the rapid detection of zinc based on air stable lipid films with incorporated calix4arene phosphoryl receptor, *Int. J. Environ. Anal. Chem.* 89 (2009) 211–222. <https://doi.org/10.1080/03067310802578952>.
- [120] S. Ahmadzadeh, M. Rezayi, E. Faghieh-Mirzaei, M. Yoosefian, A. Kassim, Highly Selective Detection of Titanium (III) in Industrial Waste Water Samples Using Mesooctamethylcalix[4]pyrrole-Doped PVC Membrane Ion-Selective Electrode, *Electrochimica Acta.* 178 (2015) 580–589. <https://doi.org/10.1016/j.electacta.2015.07.014>.
- [121] V.K. Gupta, S. Kumar, R. Singh, L.P. Singh, S.K. Shoora, B. Sethi, Cadmium (II) ion sensing through p-tert-butyl calix[6]arene based potentiometric sensor, *J. Mol. Liq.* 195 (2014) 65–68. <https://doi.org/10.1016/j.molliq.2014.02.001>.
- [122] R. Chester, M. Sohail, M.I. Ogden, M. Mocerino, E. Pretsch, R. De Marco, A calixarene-based ion-selective electrode for thallium(I) detection, *Anal. Chim. Acta.* 851 (2014) 78–86. <https://doi.org/10.1016/j.aca.2014.08.046>.
- [123] C. Dernane, A. Zazoua, I. Kazane, N. Jaffrezic-Renault, Cadmium-sensitive electrode based on tetracetone derivatives of p-tert-butylcalix[8]arene, *Mater. Sci. Eng. C.* 33 (2013) 3638–3643. <https://doi.org/10.1016/j.msec.2013.04.049>.

- [124] C. Göde, M.L. Yola, A. Yılmaz, N. Atar, S. Wang, A novel electrochemical sensor based on calixarene functionalized reduced graphene oxide: Application to simultaneous determination of Fe(III), Cd(II) and Pb(II) ions, *J. Colloid Interface Sci.* 508 (2017) 525–531. <https://doi.org/10.1016/j.jcis.2017.08.086>.
- [125] P. Shivappa Adarakatti, C.W. Foster, C.E. Banks, A.K. N. S., P. Malingappa, Calixarene bulk modified screen-printed electrodes (SPCCEs) as a one-shot disposable sensor for the simultaneous detection of lead(II), copper(II) and mercury(II) ions: Application to environmental samples, *Sens. Actuators Phys.* 267 (2017) 517–525. <https://doi.org/10.1016/j.sna.2017.10.059>.
- [126] J. Pizarro, E. Flores, V. Jimenez, T. Maldonado, C. Saitz, A. Vega, F. Godoy, R. Segura, Synthesis and characterization of the first cyrhetrenyl-appended calix[4]arene macrocycle and its application as an electrochemical sensor for the determination of Cu(II) in bivalve mollusks using square wave anodic stripping voltammetry, *Sens. Actuators B Chem.* 281 (2019) 115–122. <https://doi.org/10.1016/j.snb.2018.09.099>.
- [127] S.F. Nur Abdul Aziz, R. Zawawi, S.A. Alang Ahmad, An Electrochemical Sensing Platform for the Detection of Lead Ions Based on Dicarboxyl-Calix[4]arene, *Electroanalysis*. 30 (2018) 533–542. <https://doi.org/10.1002/elan.201700736>.
- [128] P.-G. Su, L.-G. Lin, P.-H. Lin, Detection of Cu(II) ion by an electrochemical sensor made of 5,17-bis(4'-nitrophenylazo)-25,26,27,28-tetrahydroxycalix[4]arene-electromodified electrode, *Sens. Actuators B Chem.* 191 (2014) 364–370. <https://doi.org/10.1016/j.snb.2013.09.117>.
- [129] L. Liu, K. Zhang, Y. Wei, A simple strategy for the detection of Cu(II), Cd(II) and Pb(II) in water by a voltammetric sensor on a TC4A modified electrode, *New J. Chem.* 43 (2019) 1544–1550. <https://doi.org/10.1039/C8NJ05089A>.
- [130] B. Lotfi, A. Tarlani, P. Akbari-Moghaddam, M. Mirza-Aghayan, A.A. Peyghan, J. Muzart, R. Zadnarm, Multivalent calix[4]arene-based fluorescent sensor for detecting silver ions in aqueous media and physiological environment, *Biosens. Bioelectron.* 90 (2017) 290–297. <https://doi.org/10.1016/j.bios.2016.11.065>.
- [131] R.J. Maya, A. Krishna, P. Sirajunnisa, C.H. Suresh, R.L. Varma, Lower Rim-Modified Calix[4]arene–Bentonite Hybrid System as a Green, Reversible, and Selective Colorimetric Sensor for Hg²⁺ Recognition, *ACS Sustain. Chem. Eng.* 5 (2017) 6969–6977. <https://doi.org/10.1021/acssuschemeng.7b01158>.
- [132] A. Dhir, V. Bhalla, M. Kumar, Ratiometric sensing of Hg²⁺ based on the calix [4] arene of partial cone conformation possessing a dansyl moiety, *Org. Lett.* 10 (2008) 4891–4894.
- [133] D. Maity, A. Chakraborty, R. Gunupuru, P. Paul, Calix [4] arene based molecular sensors with pyrene as fluoregenic unit: effect of solvent in ion selectivity and colorimetric detection of fluoride, *Inorganica Chim. Acta.* 372 (2011) 126–135.
- [134] M. Kumar, R. Kumar, V. Bhalla, F-induced 'turn-on' fluorescent chemosensor based on 1, 3-alt thiocalix [4] arene, *Tetrahedron.* 65 (2009) 4340–4344.
- [135] S. Erdemir, B. Tabakci, M. Tabakci, A highly selective fluorescent sensor based on calix[4]arene appended benzothiazole units for Cu²⁺, S²⁻ and HSO₄⁻ ions in aqueous solution, *Sens. Actuators B Chem.* 228 (2016) 109–116. <https://doi.org/10.1016/j.snb.2016.01.017>.
- [136] J.-L. Yang, Y.-H. Yang, Y.-P. Xun, K.-K. Wei, J. Gu, M. Chen, L.-J. Yang, Novel Amino-pillar[5]arene as a Fluorescent Probe for Highly Selective Detection of Au³⁺ Ions, *ACS Omega.* 4 (2019) 17903–17909. <https://doi.org/10.1021/acsomega.9b02951>.
- [137] L. Eddaif, A. Shaban, J. Telegdi, I. Szendro, A Piezogravimetric Sensor Platform for Sensitive Detection of Lead (II) Ions in Water Based on Calix[4]resorcinarene Macrocycles: Synthesis, Characterization and Detection, *Arab. J. Chem.* (2019) S1878535219301042. <https://doi.org/10.1016/j.arabjc.2019.09.002>.
- [138] L. Eddaif, A. Shaban, I. Szendro, Calix[4]Resorcinarene Macrocycles Interactions with Cd²⁺, Hg²⁺, Pb²⁺, and Cu²⁺ Cations: a QCM- I and Langmuir Ultra- thin Monolayers Study, *Electroanalysis*. (2019) elan.201900651. <https://doi.org/10.1002/elan.201900651>.
- [139] A. Shaban, L. Eddaif, Comparative study of a sensing platform via functionalized Calix[4]resorcinarene ionophores on QCM resonator as sensing materials for detection of heavy metal ions in aqueous environments., *Electroanalysis*. (2020) elan.202060331. <https://doi.org/10.1002/elan.202060331>.

- [140] E. Pungor, E. Hollos-Rokosinyi, The use of membrane electrodes in the analysis of ionic concentrations, *Acta. Chim. Acad. Sci. Hung.* 27 (1961) 63–8. ISSN: 0001-5407.
- [141] E. Pungor, J. Havas, K. Toth, G. Madarasz, Hungarian patent 152.106 (1963).
- [142] J. Pick, K. Tóth, E. Pungor, M. Vasák, W. Simson, A potassium-selective silicone-rubber membrane electrode based on a neutral carrier, *Analytica Chimica Acta.* 64 (1973) 477–480. [https://doi.org/10.1016/S0003-2670\(01\)82481-8](https://doi.org/10.1016/S0003-2670(01)82481-8).
- [143] R.E. Gyurcsányi, A.-S. Nybäck, A. Ivaska, K. Tóth, G. Nagy, Novel polypyrrole based all-solid-state potassium-selective microelectrodes, *Analyst.* 123 (1998) 1339–1344. <https://doi.org/10.1039/a800389k>.
- [144] L. Höfler, I. Bedlechowicz, T. Vigassy, R.E. Gyurcsányi, E. Bakker, E. Pretsch, Limitations of Current Polarization for Lowering the Detection Limit of Potentiometric Polymeric Membrane Sensors, *Anal. Chem.* 81 (2009) 3592–3599. <https://doi.org/10.1021/ac802588j>.
- [145] L. Höfler, R.E. Gyurcsányi, Nanosensors lost in space. A random walk study of single molecule detection with single-nanopore sensors, *Analytica Chimica Acta.* 722 (2012) 119–126. <https://doi.org/10.1016/j.aca.2012.02.010>.
- [146] J. Szűcs, T. Lindfors, J. Bobacka, R.E. Gyurcsányi, Ion-selective Electrodes with 3D Nanostructured Conducting Polymer Solid Contact, *Electroanalysis.* 28 (2016) 778–786. <https://doi.org/10.1002/elan.201500465>.
- [147] D. Pocsai, L. Höfler, Application of Potentiometric Ion-Breakthrough to Assess Individual Diffusion Coefficients of Ions in Ion-Selective Membranes, *J. Electrochem. Soc.* 167 (2020) 147506. <https://doi.org/10.1149/1945-7111/abc35c>.
- [148] J. Kozma, S. Papp, R.E. Gyurcsányi, Solid-contact ion-selective electrodes based on ferrocene-functionalized multi-walled carbon nanotubes, *Electrochemistry Communications.* 123 (2021) 106903. <https://doi.org/10.1016/j.elecom.2020.106903>.
- [149] Y. Aoyama, Y. Tanaka, S. Sugahara, Molecular recognition. 5. Molecular recognition of sugars via hydrogen-bonding interaction with a synthetic polyhydroxy macrocycle, *J. Am. Chem. Soc.* 111 (1989) 5397–5404. <https://doi.org/10.1021/ja00196a052>.
- [150] Y. Aoyama, Y. Tanaka, H. Toi, H. Ogoshi, Polar host-guest interaction. Binding of nonionic polar compounds with a resorcinol-aldehyde cyclooligomer as a lipophilic polar host, *J. Am. Chem. Soc.* 110 (1988) 634–635. <https://doi.org/10.1021/ja00210a073>.
- [151] D. Diamond, K. Nolan, Peer Reviewed: Calixarenes: Designer Ligands for Chemical Sensors, *Anal. Chem.* 73 (2001) 22 A-29 A. <https://doi.org/10.1021/ac012376g>.
- [152] V. Arora, H.M. Chawla, S.P. Singh, Calixarenes as sensor materials for recognition and separation of metal ions, *Arkivoc.* 2 (2007) 172–200.
- [153] M. Deska, B. Dondela, W. Sliwa, Selected applications of calixarene derivatives, *Arkivoc.* 6 (2015) 393–416.
- [154] W.C. Moreira, P.J. Dutton, R. Aroca, Langmuir-Blodgett Monolayers, and Vibrational Spectra of Calix[4]Resorcinarene, *Langmuir.* 10 (1994) 4148–4152. <https://doi.org/10.1021/la00023a039>.
- [155] F. Davis, C.J.M. Stirling, Calix-4-resorcinarene Monolayers and Multilayers: Formation, Structure, and Differential Adsorption ¹, *Langmuir.* 12 (1996) 5365–5374. <https://doi.org/10.1021/la960543f>.
- [156] F. Davis, A.J. Lucke, K.A. Smith, C.J.M. Stirling, Order and Structure in Langmuir–Blodgett Mono- and Multilayers of Resorcarenes, *Langmuir.* 14 (1998) 4180–4185. <https://doi.org/10.1021/la980078h>.
- [157] A.A. Turshatov, N.B. Melnikovac, Y.D. Semchikova, I.S. Ryzhkinab, T.N. Pashirovab, D. Möbiusd, S.Y. Zaitseve, Interaction of monolayers of calix[4]resorcinarene derivatives with copper ions in the aqueous subphase, in 2004.
- [158] F.L. Supian, T.H. Richardson, M. Deasy, F. Kelleher, J.P. Ward, V. McKee, Interaction between Langmuir and Langmuir–Blodgett Films of Two Calix[4]arenes with Aqueous Copper and Lithium Ions, *Langmuir.* 26 (2010) 10906–10912. <https://doi.org/10.1021/la100808r>.
- [159] J. Torrent-Burgués, F. Vocanson, J.J. Pérez-González, A. Errachid, Synthesis, Langmuir and Langmuir–Blodgett films of a calix[7]arene ethyl ester, *Colloids Surf. Physicochem. Eng. Asp.* 401 (2012) 137–147. <https://doi.org/10.1016/j.colsurfa.2012.03.040>.

References

- [160] A. Saftics, G.A. Prósz, B. Türk, B. Peter, S. Kurunczi, R. Horvath, In situ viscoelastic properties and chain conformations of heavily hydrated carboxymethyl dextran layers: a comparative study using OWLS and QCM-I chips coated with waveguide material, *Sci. Rep.* 8 (2018). <https://doi.org/10.1038/s41598-018-30201-6>.
- [161] J.R. Reimers, M.J. Ford, S.M. Marcuccio, J. Ulstrup, N.S. Hush, Competition of van der Waals and chemical forces on gold–sulfur surfaces and nanoparticles, *Nat. Rev. Chem.* 1 (2017) 0017. <https://doi.org/10.1038/s41570-017-0017>.
- [162] T. Zaba, A. Noworolska, C.M. Bowers, B. Breiten, G.M. Whitesides, P. Cyganik, Formation of Highly Ordered Self-Assembled Monolayers of Alkynes on Au(111) Substrate, *J. Am. Chem. Soc.* 136 (2014) 11918–11921. <https://doi.org/10.1021/ja506647p>.
- [163] Q. Tang, D. Jiang, Insights into the PhC≡C/Au Interface, *J. Phys. Chem. C.* 119 (2015) 10804–10810. <https://doi.org/10.1021/jp508883v>.
- [164] A. Chaudhuri, M. Odelius, R.G. Jones, T.-L. Lee, B. Detlefs, D.P. Woodruff, The structure of the Au(111)/methylthiolate interface: New insights from near-edge x-ray absorption spectroscopy and x-ray standing waves, *J. Chem. Phys.* 130 (2009) 124708. <https://doi.org/10.1063/1.3102095>.
- [165] J.R. Reimers, M.J. Ford, A. Halder, J. Ulstrup, N.S. Hush, Gold surfaces, and nanoparticles are protected by Au(0)–thiyl species and are destroyed when Au(I)–thiolates form, *Proc. Natl. Acad. Sci.* 113 (2016) E1424–E1433. <https://doi.org/10.1073/pnas.1600472113>.

A ppendices

Appendix A. IR data

Table A.1: IR parameters for compound I₁.

Molecular parts	$\bar{\nu}$ (cm ⁻¹)	Bond	Vibration	Intensity
Resorcinolic part	3253	Associated O-H	Stretching	Strong & large
	1164	C-O	Stretching	Medium
	1292	O-H	In-plane deformation	Medium
Vinyllic fragment	3077	=C-H	Stretching	Medium
	3034	=C-H	Stretching	Medium
	1822	C-H	Deformation harmonics	Medium
	1619	C=C	Stretching	Medium
Aromatic moieties	3074	=C-H	Stretching	Medium
	1499	C=C	Stretching	Medium
	1443	C=C	Stretching	Medium
	1980	C-H	Deformation harmonics	Small
	835	C-H	Out-of-plane deformation	Medium to small
Alkane	2924	CH ₂	Asymmetric stretching	Strong
	2853	CH ₂	Symmetric stretching	Medium
	721	CH ₂	Rocking	Medium to small

Table A.2: IR parameters for ionophore I₂

Molecular parts	$\bar{\nu}$ (cm ⁻¹)	Bond	Vibration	Intensity
Resorcinolic part	3484	Associated O-H	Stretching	Strong & large
	1195	C-O	Stretching	Medium to strong
	1377	O-H	In-plane deformation	Medium
Aromatic moieties	3038	=C-H	Stretching	Very small
	1616	C=C	Stretching	Medium
	1504	C=C	Stretching	Medium
	1464	C=C	Stretching	Medium
	1979	C-H	Deformation harmonics	Small
	900	=C-H	Out-of-plane deformation	Small
Alkane	2852	CH ₃	Symmetric stretching	Strong
	1428	CH ₃	Asymmetric plane deformation	Medium
	2921	CH ₂	Asymmetric stretching	Strong
	1465	CH ₂	Scissoring	Medium
	721	CH ₂	Rocking	Medium
	1342	C-H	In-plane deformation	Very small
	1167	Linear chain C-C	Stretching	Small

Table A.3: IR parameters for enantiomers I₃ and I₄

Molecular parts	$\bar{\nu}$ (cm ⁻¹)	Bond	Vibration	Intensity
Resorcinolic part	3340	Associated O-H	Stretching	Strong & large
	1226	C-O	Stretching	Medium
	1348	O-H	In-plane deformation	Medium
Vinyllic moieties	3070	=C-H	Stretching	Small to medium
	3027	=C-H	Stretching	Small to medium
	1822	C-H	Deformation harmonics	Small
	1640	C=C	Stretching	Small to medium
	907	=C-H	Out-of-plane deformation	Strong
	880	=C-H	deformation	Strong
	3030	=C-H	Stretching	Small
Aromatic cycles	1602	C=C	Stretching	Small
	1560	C=C	Stretching	Small
	1540	C=C	Stretching	Small
	1468	C=C	Stretching	Medium
	1980	C-H	Deformation harmonics	Small
	778	=C-H	Out-of-plane deformation	Medium
	750	=C-H	deformation	Medium
	880	=C-H		Medium
Tertiary amine	1145	C-N	Stretching	Small
Cyclic ether	1181	C-O	Stretching	Medium to strong
	2853	CH ₃	Symmetric stretching	Strong
	1468	CH ₃	Symmetric plane deformation	Medium
Alkane	2925	CH ₂	Asymmetric stretching	Strong
	700	CH ₂	Rocking	Medium
	2970	C-H	Stretching	Small
	1346	C-H	Out-of-plane deformation	Small

Appendix B. NMR data and spectra

Table B.1: ¹H NMR and ¹³C NMR shifts for ionophores I₁-I₄

Compound	¹ H NMR shifts	¹³ C NMR shifts
I ₁	(DMSO-d ₆ , 600 MHz, 25°C) δ(ppm): 8.85 (8H, s); 7.12 (4H, s); 6.13 (4H, s); 5.75 (4H, m); 4.98 (4H, m); 4.92 (4H, m); 4.22 (4H, t, J = 8.3Hz); 2.07 – 1.97 (16H, m); 1.43 – 1.05 (48H, m)	(DMSO-d ₆ , 150 MHz, 25°C) δ (ppm): 151.7; 138.7; 124.7; 122.9; 114.5; 102.3; 33.2; 33.0; 29.2; 29.1; 28.9; 28.5; 28.3; 27.7
	(DMSO-d ₆ , 400 MHz, 40°C) δ (ppm): 8.75 (8H, s); 7.12 (4H, s); 6.13 (4H, s); 4.23 (4H, t, J = 8.0Hz); 2.02 (8H, m); 1.47 – 1.00 (56H, m); 0.82 (12H, t, J = 6.3Hz)	(DMSO-d ₆ , 100 MHz, 50°C) δ (ppm): 151.5; 124.4; 123.0; 102.3; 33.8; 32.8; 31.1; 28.9; 28.8; 28.5; 27.5; 21.8; 13.6
I ₃ and I ₄	(CDCl ₃ , 400 MHz, 25°C) δ(ppm): 7.67 (4H, s); 7.18 (8H, d, J = 7.5Hz); 7.10 (4H, s); 7.05 (8H, m); 6.96 (4H, t, J = 7.5Hz); 5.82 (4H, m); 5.15 (4H, d, J = 10.4Hz); 5.04 – 4.90 (12H, m); 4.20 (4H, t, J = 7.8Hz); 3.96 (4H, d, J = 17.5Hz); 3.81 (4H, q, J = 6.2Hz); 3.73 (4H, d, J = 17.5 Hz); 2.18 (8H, m); 2.04 (8H, q, J = 6.0Hz); 1.50 – 1.20 (60H, m)	(CDCl ₃ , 100 MHz, 25°C) δ(ppm) : 149.6; 148.7; 144.5; 139.2; 128.2; 127.0; 124.3; 123.4; 121.1; 114.2; 108.9; 80.9; 58.0; 44.5; 33.8; 33.7; 32.7; 29.7; 29.6; 29.2; 29.0; 28.1; 21.4

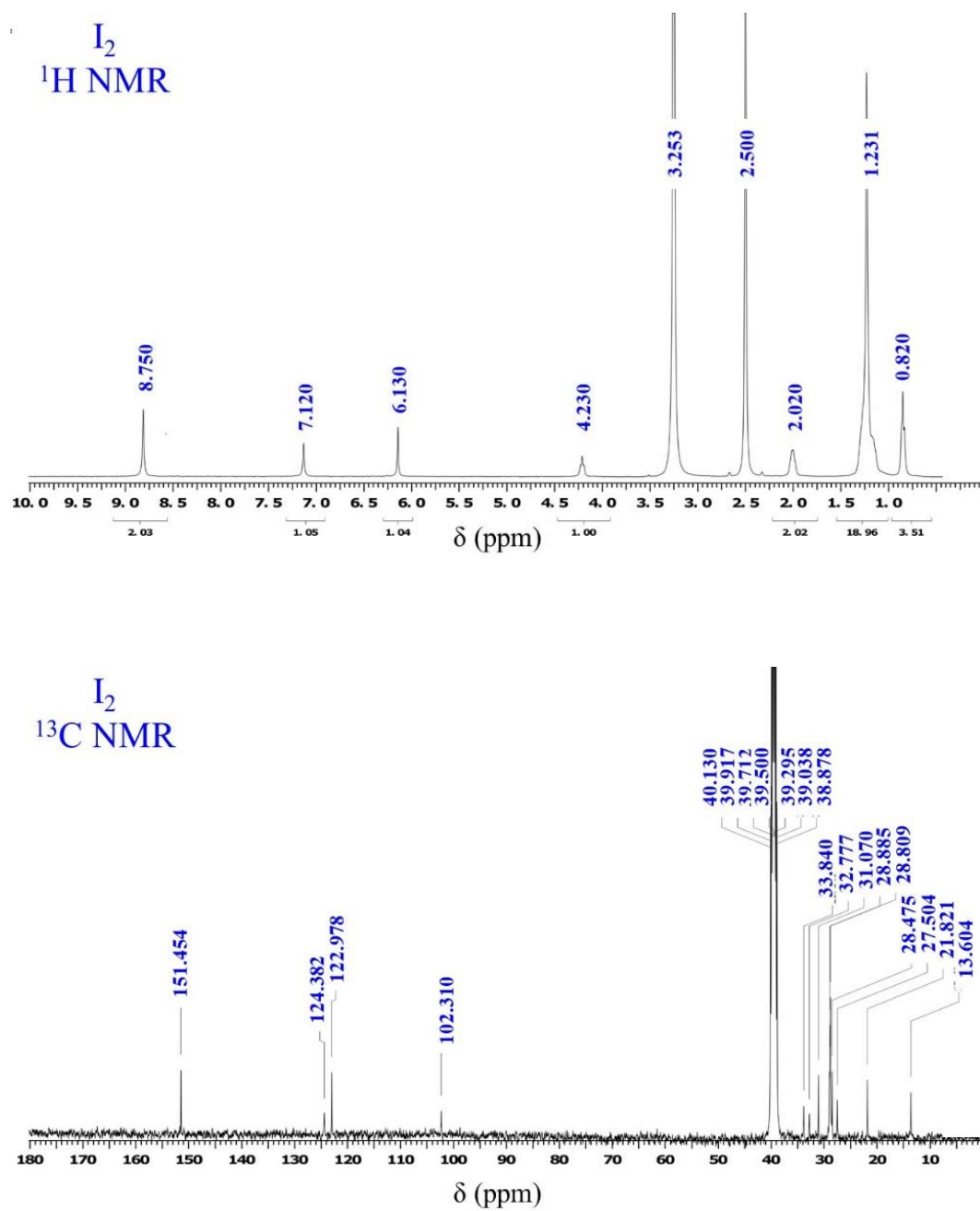


Fig. B.1: Proton (^1H) and Carbon (^{13}C) NMR spectra of ionophore (I_2)
C-dec-9-enylcalix[4]resorcinarene

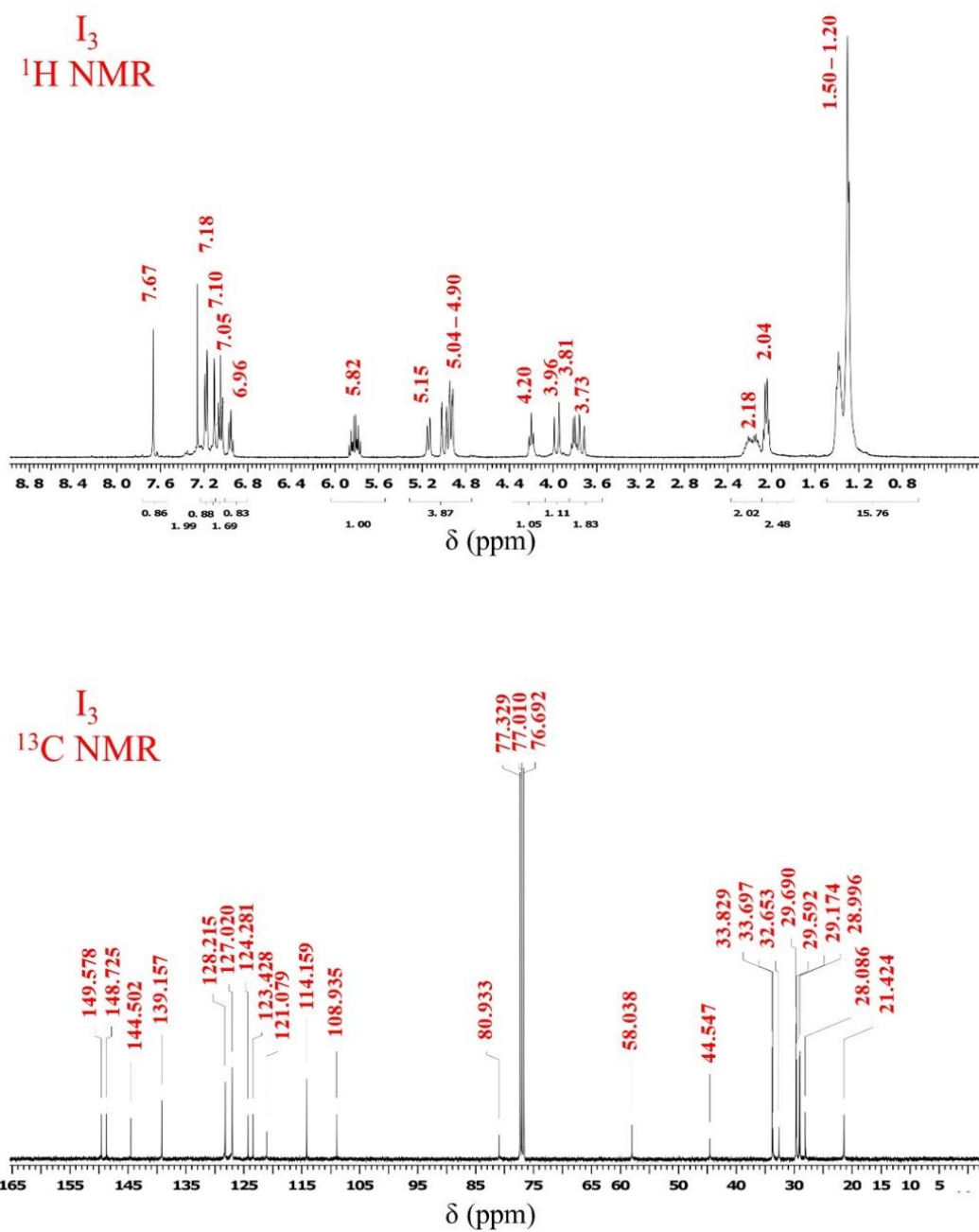


Fig. B.2: Proton (¹H) and Carbon (¹³C) NMR spectra of ionophore (I₃)
C-undecylcalix[4]resorcinarene,-O-(S)- α -methylbenzylamine

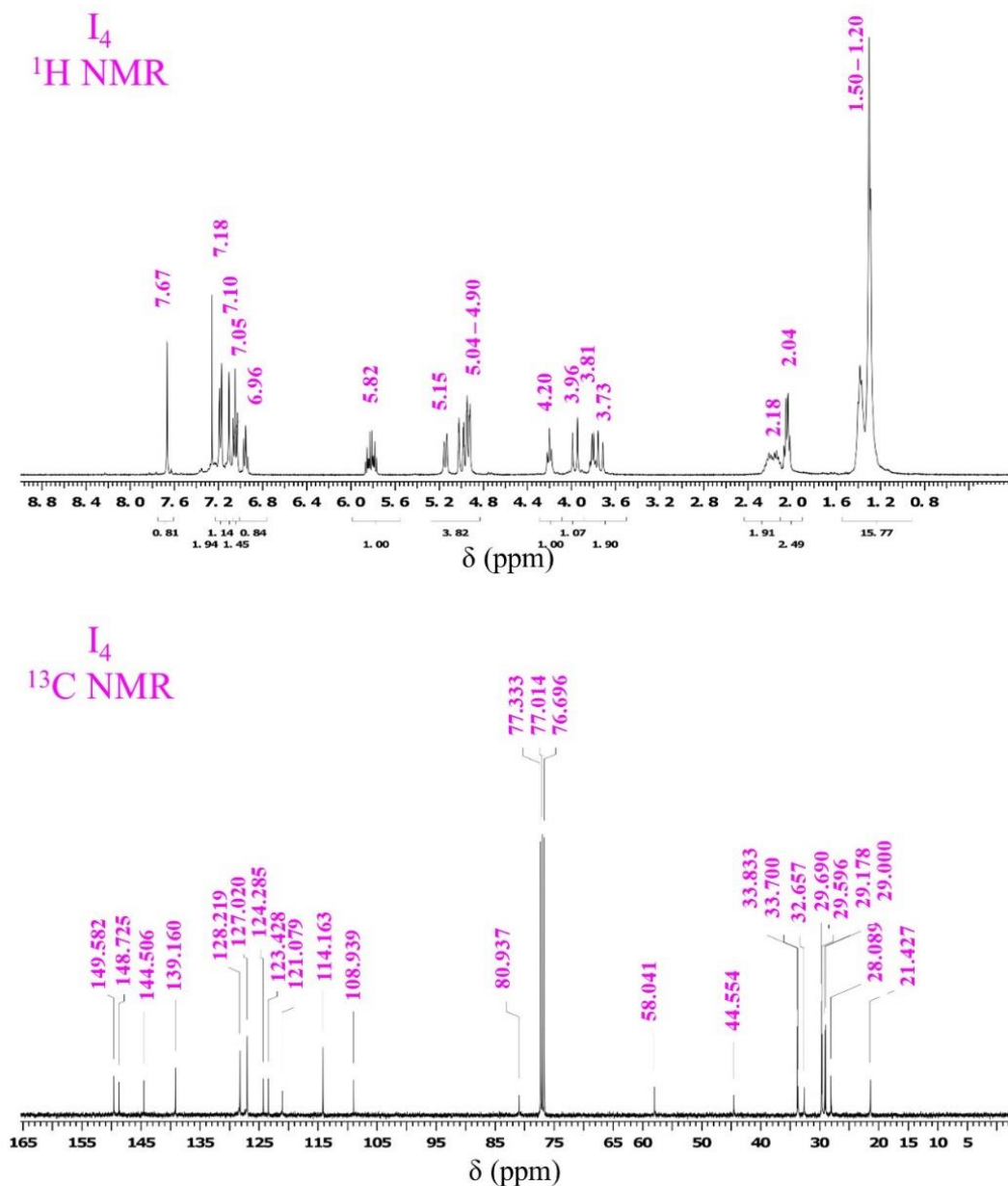


Fig. B.3: Proton (^1H) and Carbon (^{13}C) NMR spectra of ionophore (I_4)
C-undecylcalix[4]resorcinarene,-O-(R+)- α -methylbenzylamine

Appendix C. Π -A isotherms' data**Table C.1:** Π -A isotherms data for I_1 .

Different ions	Concentration (ppm)	Π_c (mN/m)	A_c ($\text{\AA}^2/\text{molecule}$)	A_{lim} ($\text{\AA}^2/\text{molecule}$)
Cd^{2+}	0 (Pure water)	32	65	110
	5	35	70	130
	25	38	70	160
	250	38	70	185
Cu^{2+}	0 (Pure water)	32	65	110
	5	40	70	150
	25	42	70	200
	250	38	130	320
Hg^{2+}	0 (Pure water)	32	65	110
	5	44	70	220
	25	45	85	240
	250	44	100	300
Pb^{2+}	0 (Pure water)	32	65	110
	5	38	70	150
	25	35	70	275
	250	35	95	320

Table C.2: Langmuir isothermal data for I_2 .

Different ions	Concentration (ppm)	Π_c (mN/m)	A_c ($\text{\AA}^2/\text{molecule}$)	A_{lim} ($\text{\AA}^2/\text{molecule}$)
Cd^{2+}	0 (Pure water)	17	65	105
	5	47	70	150
	25	48	80	220
	250	52	90	320
Cu^{2+}	0 (Pure water)	17	65	105
	5	44	80	140
	25	44	160	370
	250	44	160	450
Hg^{2+}	0 (Pure water)	17	65	105
	5	37	66	220
	25	43	67	290
	250	38	67	310
Pb^{2+}	0 (Pure water)	17	65	105
	5	27	65	160
	25	37	66	170
	250	37	111	300

Table C.3: Langmuir isotherms data for ionophores I₃ and I₄.

Different ions	Concentration (ppm)	Π_c (mN/m)	A_c ($\text{\AA}^2/\text{molecule}$)	A_{lim} ($\text{\AA}^2/\text{molecule}$)
Ionophore I ₃				
Cd ²⁺	0 (Pure water)	39	100	240
	5	52	150	550
	25	48	290	580
	250	47	130	630
Cu ²⁺	0 (Pure water)	39	100	240
	5	39	170	270
	25	41	220	440
	250	17	620	700
Hg ²⁺	0 (Pure water)	39	100	240
	5	35	210	320
	25	39	290	480
	250	30	410	600
Pb ²⁺	0 (Pure water)	39	100	240
	5	43	270	450
	25	46	235	490
	250	38	320	620

Appendix D. QCM-I data

Table D.1: Normalized frequency, dissipation, and FWHM data for I₁ based QCM sensor against various HM amounts

Different ions	Concentrations (ppm)	Normalized ΔF (Hz)	ΔD ($\times 10^{-6}$)	Normalized $\Delta FWHM$ (Hz)
Cd ²⁺	0 (Pure water)	-1.14 ± 0.01	0.07 ± 0.02	0.08 ± 0.02
	5	- 9.85 ± 0.04	1.54 ± 0.01	7.70 ± 0.01
	25	- 40.70 ± 0.30	2.51 ± 0.03	19.31 ± 0.04
	250	- 61.70 ± 0.90	3.83 ± 0.04	38.04 ± 0.30
	500	- 73.46 ± 0.78	3.84 ± 0.07	97.45 ± 1.20
	1000	- 76.55 ± 0.50	5.79 ± 0.90	202.70 ± 2.40
Cu ²⁺	0 (Pure water)	-4.94 ± 0.03	0.12 ± 0.01	0.67 ± 0.01
	5	- 14.42 ± 0.02	2.87 ± 0.04	14.59 ± 0.02
	25	- 32.76 ± 0.07	3.09 ± 0.02	16.62 ± 0.04
	250	- 37.91 ± 0.01	3.19 ± 0.03	28.51 ± 0.03
	500	- 50.91 ± 0.09	3.40 ± 0.09	42.14 ± 0.20
	1000	- 56.68 ± 0.10	6.24 ± 0.10	64.89 ± 0.09
Hg ²⁺	0 (Pure water)	-0.65 ± 0.08	0.05 ± 0.01	0.56 ± 0.06
	5	- 16.46 ± 0.03	0.36 ± 0.01	5.49 ± 0.02
	25	- 34.27 ± 0.06	1.17 ± 0.02	6.05 ± 0.01
	250	- 45.47 ± 0.07	3.43 ± 0.03	25.19 ± 0.07
	500	- 83.06 ± 0.13	3.98 ± 0.06	51.24 ± 0.03
	1000	- 90.32 ± 0.01	5.05 ± 0.04	59.59 ± 0.04
Pb ²⁺	0 (Pure water)	-2.13 ± 0.02	0.05 ± 0.03	0.21 ± 0.03
	5	- 6.55 ± 0.01	0.87 ± 0.02	4.20 ± 0.01
	25	- 10.48 ± 0.07	0.71 ± 0.01	6.65 ± 0.02
	250	- 20.36 ± 0.09	1.35 ± 0.04	21.49 ± 0.05
	500	- 29.90 ± 0.04	6.31 ± 0.22	31.67 ± 0.04
	1000	- 54.44 ± 0.03	6.51 ± 0.34	32.77 ± 0.07

Table D.2: Normalized frequency, dissipation, and FWHM data for I₂ based QCM sensor against various HM amounts

Different ions	Concentrations (ppm)	Normalized ΔF (Hz)	ΔD ($\times 10^{-6}$)	Normalized $\Delta FWHM$ (Hz)
Cd ²⁺	0 (Pure water)	-0.56 \pm 0.02	0.07 \pm 0.01	0.44 \pm 0.05
	5	- 1.99 \pm 0.01	0.75 \pm 0.01	4.47 \pm 0.03
	25	- 6.05 \pm 0.04	0.85 \pm 0.04	9.54 \pm 0.04
	250	- 12.16 \pm 0.39	1.78 \pm 0.02	11.31 \pm 0.01
	500	- 15.81 \pm 0.08	2.00 \pm 0.03	21.17 \pm 0.20
	1000	- 21.51 \pm 0.15	4.28 \pm 0.09	27.49 \pm 0.02
Cu ²⁺	0 (Pure water)	-0.25 \pm 0.01	0.38 \pm 0.02	0.18 \pm 0.03
	5	- 10.76 \pm 0.03	0.75 \pm 0.01	2.70 \pm 0.01
	25	- 18.03 \pm 0.02	0.76 \pm 0.03	3.72 \pm 0.04
	250	- 35.04 \pm 0.01	1.93 \pm 0.04	9.55 \pm 0.05
	500	- 38.19 \pm 0.04	9.14 \pm 0.07	45.93 \pm 0.08
	1000	- 45.61 \pm 0.07	10.48 \pm 0.05	52.26 \pm 0.07
Hg ²⁺	0 (Pure water)	0.00 \pm 0.00	0.00 \pm 0.00	0.00 \pm 0.00
	5	- 13.07 \pm 0.04	0.00 \pm 0.00	10.04 \pm 0.01
	25	- 14.80 \pm 0.02	2.03 \pm 0.03	11.81 \pm 0.02
	250	- 23.04 \pm 0.03	2.38 \pm 0.10	21.17 \pm 0.04
	500	- 25.07 \pm 0.01	4.21 \pm 0.04	23.96 \pm 0.03
	1000	- 28.73 \pm 0.05	4.75 \pm 0.05	82.09 \pm 0.12
Pb ²⁺	0 (Pure water)	0.00 \pm 0.00	0.00 \pm 0.00	0.00 \pm 0.00
	5	- 10.70 \pm 0.02	1.57 \pm 0.03	15.34 \pm 0.01
	25	- 14.08 \pm 0.01	3.11 \pm 0.02	18.13 \pm 0.03
	250	- 34.09 \pm 0.03	3.60 \pm 0.01	26.22 \pm 0.04
	500	- 50.72 \pm 0.07	5.21 \pm 0.12	44.92 \pm 0.08
	1000	- 105.78 \pm 0.01	8.96 \pm 0.04	59.33 \pm 0.12

Table D.3: Normalized frequency, dissipation, and FWHM data for I₃ based QCM sensor against various HM amounts

Different ions	Concentrations (ppm)	Normalized ΔF (Hz)	ΔD ($\times 10^{-6}$)	Normalized $\Delta FWHM$ (Hz)
Cd ²⁺	0 (Pure water)	-1.19 \pm 0.03	0.07 \pm 0.01	0.00 \pm 0.01
	5	- 4.42 \pm 0.02	0.08 \pm 0.02	0.09 \pm 0.02
	25	- 5.23 \pm 0.01	0.04 \pm 0.03	1.70 \pm 0.03
	250	- 12.27 \pm 0.09	0.07 \pm 0.04	1.98 \pm 0.04
	500	- 18.04 \pm 0.04	0.40 \pm 0.09	5.29 \pm 0.14
	1000	- 69.56 \pm 0.05	1.03 \pm 0.01	14.08 \pm 0.40
Cu ²⁺	0 (Pure water)	-0.14 \pm 0.01	0.00 \pm 0.00	0.00 \pm 0.00
	5	- 7.08 \pm 0.03	0.12 \pm 0.01	1.95 \pm 0.03
	25	- 7.88 \pm 0.02	0.30 \pm 0.01	2.00 \pm 0.02
	250	- 10.42 \pm 0.09	0.24 \pm 0.02	8.75 \pm 0.01
	500	- 17.14 \pm 0.07	2.40 \pm 0.04	18.40 \pm 0.17
	1000	- 22.33 \pm 0.12	3.67 \pm 0.13	38.24 \pm 0.20
Hg ²⁺	0 (Pure water)	-0.74 \pm 0.02	0.01 \pm 0.00	0.09 \pm 0.01
	5	- 16.45 \pm 0.01	0.25 \pm 0.02	7.90 \pm 0.07
	25	- 32.20 \pm 0.03	0.45 \pm 0.03	8.41 \pm 0.03
	250	- 50.05 \pm 0.04	0.55 \pm 0.01	10.91 \pm 0.04
	500	- 60.72 \pm 0.10	1.23 \pm 0.04	19.92 \pm 0.02
	1000	- 84.17 \pm 0.17	10.48 \pm 0.40	53.93 \pm 0.80
Pb ²⁺	0 (Pure water)	- 0.30 \pm 0.04	0.47 \pm 0.23	5.60 \pm 0.01
	5	- 2.40 \pm 0.30	0.54 \pm 0.11	7.70 \pm 0.03
	25	- 4.80 \pm 0.10	1.10 \pm 0.34	12.08 \pm 0.05
	250	- 6.80 \pm 0.40	2.50 \pm 0.48	15.90 \pm 0.02
	500	- 8.50 \pm 0.10	4.10 \pm 0.23	20.62 \pm 0.07
	1000	- 10.00 \pm 0.10	8.50 \pm 0.07	80.00 \pm 0.04